

PROCEEDING OF SCIENCE, ENGINEERING & NANOTECHNOLOGY

PReSENT

Regional Research Seminar on Science, Engineering and Nanotechnology

“Frontier in Multidisciplinary Research”

PROCEEDING OF SCIENCE, ENGINEERING & NANOTECHNOLOGY

PReSENT

Regional Research Seminar on Science, Engineering and Nanotechnology

“Frontier in Multidisciplinary Research”

7 December 2017



EDITORIAL BOARD

Advisory Editor-in-Chief

Nafarizal Nayan

Editor-in-Chief

Muhammad Suhaimi Sulong

Editorial Committee

Marlia Morsin

Nan Mad Sahar

Rahmat Sanudin

Feri Adriyanto

MICROELECTRONICS AND NANOTECHNOLOGY –
SHAMSUDDIN RESEARCH CENTRE
UNIVERSITI TUN HUSSEIN ONN MALAYSIA
86400 PARIT RAJA, JOHOR.



2018

© Penerbit UTHM

First Edition 2018

Copyright reserved. Reproduction of any articles, illustrations and content of this book in any form be it electronic, mechanical photocopy, recording or any other form without any prior written permission from The Publisher's Office of Universiti Tun Hussein Onn Malaysia, Parit Raja, Batu Pahat, Johor is prohibited. Any negotiations are subjected to calculations of royalty and honorarium.

Perpustakaan Negara Malaysia Cataloguing-in-Publication Data

PROCEEDING OF SCIENCE, ENGINEERING & NANOTECHNOLOGY

PReSENT / Editor-in-Chief Dr Muhammad Suhaimi Hj Sulong

Published by:

Penerbit UTHM

Universiti Tun Hussein Onn Malaysia

86400 Parit Raja,

Batu Pahat, Johor,

Malaysia.

FOREWORD

Congratulation and thank you for submitting and presenting your research finding at Regional Research Seminar on Science, Engineering & Nanotechnology (ReSENT2017) which was held on 7 December 2017 at MiNT-SRC Centre of Excellence, Universiti Tun Hussein Onn Malaysia, Johor. This is the second research seminar conducted at MiNT-SRC, after the first MiNT-SRC Research Seminar 2013 (MRS2013). The ReSENT2017 was intended between Universiti Tun Hussein Onn Malaysia and Universitas Sebelas Maret, Indonesia as part of the research collaboration activities in order to provide a session for discussing all related subjects on engineering and nanotechnologies especially in electronic device applications between academicians, researchers, and postgraduate students.

More than thirty one papers were presented, and we had forty participants including foreign researchers and fruitful discussions in the seminar. This special issue of "Proceeding ReSENT 2017" containing eighteen papers is a collection of the part of the research papers presented in the seminar. Those papers were referred on the publication standard of the International Journal of Integrated Engineering (IJIE). The aim of this special issue is to inform the latest researches in the fields of "Nanotechnology".

We sincerely wish that the readers will find excited and stimulated papers by this special issue in PReSENT.

THE ADVISOR

PREFACE

Proceeding of Science, Engineering and Nanotechnology (PReSENT) contains the research papers presented during the 2017 Regional Research Seminar on Science, Engineering and Nanotechnology (ReSENT2017) which was held at SoC and TCAD Laboratory, Microelectronic and Nanotechnology – Shamsuddin Research Centre (MiNT-SRC) in Universiti Tun Hussein Onn Malaysia on 7th December, 2017.

ReSENT2017 was initiated regionally collaboration between Malaysia and Indonesia higher education with the assistance of Institute of Integrated Engineering (I2E), UTHM. The idea was initially brought up to provide an opportunity for postgraduate students from UTHM, who are presently pursuing their Master's or Doctoral degree, to congregate and share their experiences and research work. The event engenders an interactive forum that creates a knowledge sharing culture and offer assistance in communicating their research to research students and other academics in a field of Microelectronics and Nanotechnology.

A total of thirteen original research papers were reviewed and accepted. These papers had highlighted a significant contribution and demonstrated a new up to date research, according to the seminar theme "Frontier in Multidisciplinary Research" for ReSENT2017 which practically create for this purpose and to allow the paper contributors the opportunity to do so. Each of these full manuscripts had been assessed and evaluated on the degree of novelty, creativity and technical depth under a double blind peer-review process, where referees and the authors are kept anonymous. This formal process is to ensure that all papers published in ReSENT2017 are of good quality and international standards. In order to uphold the rights of publication, every author(s) had agreed the terms and conditions and signed their copyright transfer form.

Finally, we would like to thank all the authors for their active participation during ReSENT2017 and their contribution to its success. Our acknowledgement goes also to the organizing committee members, session chairs and reviewers for the papers.

THE EDITOR-IN-CHIEF

CONTENT

Editorial Board	iii
Foreward	vi
Preface	vii
1. Hybrid Feeding Technique for the Design and Analysis of a Square Ring Patch Antenna	1
<i>Abdul rashid O. Mumin, Jiwa Abdullah, Rozlan Alias, Samsul Haimi Dahlan, Jawad Ali</i>	
2. Mini Review of n-type and p-type Doped GaN Thin Films	6
<i>Muliana Tahan, Nafarizal Nayan, Mohd Zainizan Sahdan, Anis Suhaili Bakri, Elfa Rizan Rizon, Siti Ashraf Abdullah, Yunus Sari, Ahmad Shuhaimi Abu Bakar, Ali Aldalbahi</i>	
3. Surface Morphology of NTO Thin Films Deposited via Magnetron Sputtering at Various Oxygen Concentrations	12
<i>Siti Ashraf Abdullah, Mohd Zainizan Sahdan, Nafarizal Nayan, Hashim Saim, Anis Suhaili Bakri, Sawsan Abdullah Abduljabbar, Cik Rohaida Cik Hak, Feri Adriyanto</i>	
4. Effect on Structural and Morphological Properties of Aluminum Thin Film at Different Substrates Deposited by Vacuum Thermal Evaporation	16
<i>Kusnanto Mukti Wibowo, Mohd. Zainizan Sahdan, Nafarizal Nayan, Yunus Sari, Zailani Mansor</i>	
5. Optimization of CuO films at different pH value for oxygen gas detection	20
<i>Nur Amaliyana Raship, Mohd Zainizan Sahdan, Anis Suhaili Bakri, Nor Damsyik Mohd Said</i>	
6. Investigation on the Aging Effect of Aluminum Thin Film Treated by Atmospheric Pressure Plasma Needle	25
<i>Rizon Rizan Elfa, Nayan Nafarizal, Mohd Khairul Ahmad, Kusnanto Mukti Wibowo, Chin Fong Soon, Mohd Zainizan Sahdan, Mohamad Hafiz Mamat, Ali Aldalbahi</i>	
7. Formation of Monolayer Polystyrene Array Template for Gold Nanomesh Structure	29
<i>Nur Liyana Razali, Marlia Morsin, Muhamad Mat Salleh, Nurfarina Zainal, Marriatyi Morsin</i>	
8. A Review of Hardware Implementation for Glucose-Insulin Regulation in Type 1 Diabetes Mellitus patient (T1DM)	33
<i>Nur Atikah Mohd Daud, Chin Fong Soon, Farhanahani Mahmud</i>	
9. A Review on the Current 3D Bioprinting Technology	39
<i>Sheril Amira Othman, Chin Fhong Soon, Farshid Sefat, Kian Sek Tee, Mohd Khairul Ahmad, Nafarizal Nayan</i>	
10. Fuzzy Logic System for Menstrual Cycle Interpretation Based on BBT Data	44
<i>Muhammad Syukri Mohd Yazed, Ariff Farhan Zainodin, Farhanahani Mahmud</i>	
11. Short Review on Techniques and Materials Used for Microfluidic Device Fabrication	49
<i>Sargunan Sundra, Chin Fhong Soon, Farhanahani Mahmud, Nurfarina Zainal, Kian Sek Tee</i>	

12.	Effects of withdrawal speed on the structural and electrical properties of TiO₂ thin films	54
	<i>Anis Suhaili Bakri, Mohd Zainizan Sahdan, Siti Ashraf Abdullah, Nur Amaliyana Raship, Sawsan Abdullah Abduljabbar, Yunus Sari</i>	
13.	A Review on Semiconductor Materials for Photoelectrochemical Water Splitting: Recent Advances and Future Challenges	58
	<i>Sawsan Abdullah Abduljabbar Anaam, Hashim Saim, Mohd Zainizan Sahdan, Anis Suhaili Bakri, Siti Ashraf Abdullah</i>	

HYBRID FEEDING TECHNIQUE FOR THE DESIGN AND ANALYSIS OF A SQUARE RING PATCH ANTENNA

Abdulrashid O. Mumin¹, Jiwa Abdullah¹, Rozlan Alias¹, Samsul Haimi Dahlan¹, Jawad Ali¹

¹Department of Communication Engineering, Faculty of Electrical and Electronic Engineering, Universiti Tun Hussein Onn Malaysia (UTHM), Johor, Malaysia.

Abstract: A hybrid feeding technique development for the assessment of antenna radiation performance by merging the inset fed and quarter wave transformer at the same time to use it in a cellular application is investigated in this paper. Scattering parameter, input impedance and radiation pattern of the proposed design at 1.8 GHz frequency have been examined by using CST studio for simulation and other measuring techniques for the fabricated design. Therefore, this feeding technique provides a comprehensive study of antenna and its impacts with respect to the reflection coefficient, and input impedance. Finally, the proposed antenna is tested using vector network analyzer to compare the simulation and measured results.

Keywords: Square Ring, Hybrid Method, Inset Fed Method, Quarter Wave Transformer-Fed Method.

1. Introduction

Microstrip patch antennas are lightweight, compact size, and low cost, due to which these antennas are considerable for their wide usage. The input impedance for these antennas relies on their numerical state, the feed type and location with the structural properties of the materials engaged. However, a subset of scattering parameters can be balance to accomplish the “best” position on matching of a specific frequency. Accordingly, this inset-fed microstrip antenna gives a type of impedance control with a planar feed outline [1],[2].

Meanwhile, quarter-wave transformer matching framework utilizing a division of transmission line roughly one quarter-wavelength in the length for matching a transmission line to load was also the part of study. It is also recognized as quarter-wave matching area with when physical length, $l=\lambda/4$ occurs at one frequency only. This wave transformer is a basic function for matching true load impedance for transmission line. Extra characteristic of a quarter-wave transformer may be developed to a multi segment plans for more extensive transfer speed. Therefore, assuming that a limited band impedance match is required, a single area transformer might be sufficient. Furthermore, multi-session quarter wave transformer outlines summarized on yield ideal matching features in a resonant frequency band. Therefore, the drawback of a quarter-wave transformer is that it matches best impedances. In the same vein, intricate load impedance transformed to the actual impedance by utilizing a suitable length of a transmission line middle of the load and the transformer on a fitting arrangement of a shunt sensitive stub. The techniques will

dependably propose the recurrence reliance of the equal load, which constantly need the impact from lessening the bandwidth of the match [3]. The four practically known feeding methods are the microstrip line, coaxial probe, aperture and proximity couplings [4, 5]. The square ring shape becomes a famous reconfiguration on antenna design [6-12].

The objective of this study is to investigate the radiation effect of cellular antenna using the hybrid-feeding configuration by emerging inset fed and quarter-wave transformer methods to develop a new design. According to the fundamental antenna configurations, the introductory reaching parametric investigations were carried by using CST Microwave studio simulation environment. This paper involves the methods and the material considered for the design in the next section. While the obtained results compared with the measured results in results and discussion section. Finally, all the work will be the part of discussion in conclusion section.

2. Materials and Method

In The proposed antenna is examined using electromagnetic simulator studio to investigate the performance and effect of the hybrid feeding techniques of the designed patch antenna where FR4 epoxy is used to analyze the geometry of antenna. Finally, a square ring patch antenna is designed using patch dimensions listed in Table I and Table II.

The proposed geometric properties and scattering parameters of the antenna based on the desired frequency at 1.8 GHz is calculated by using the following computational formulas in [13].

$$W_0 = \frac{c}{2f_r \sqrt{\frac{(\epsilon_r + 1)}{2}}}$$

$$L_0 = 0.412h \frac{(\epsilon_{\text{eff}} + 0.3) \left(\frac{w}{h} \right) + 0.264}{(\epsilon_{\text{eff}} - 0.258) \left(\frac{w}{h} \right) + 0.8}$$

$$L_0 = \frac{c}{2f_r \sqrt{\epsilon_{\text{eff}}}} - 2\Delta L_0$$

$$L_f = \frac{\lambda_g}{4}$$

$$\frac{W_1}{h} = \frac{8e^A}{e^{2A} - 2}$$

Where $\frac{W_1}{h} < 2$

$$A = \frac{Z_o}{60} \sqrt{\frac{\epsilon_r + 1}{2}} + \frac{\epsilon_r - 1}{\epsilon_r + 1} (0.23 + \frac{0.11}{\epsilon_r})$$

$$L_o = W_o = 0.46 \frac{\lambda}{\sqrt{\epsilon_r}}$$

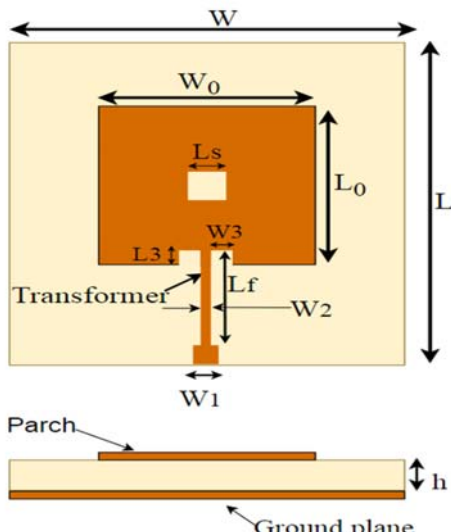


Fig. 1 :Configuration structure of the proposed patch antenna

Table I GEOMETRY PARAMETERS & SYMBOLS

Parameter	Symbols
width	W_0
length	L_0
effective dielectric	ϵ_{eff}
length extension	ΔL_0
feed of length	L_f
feed line width	W_1
guided wavelength	λ_g
Substrate high	h

(1) Table II. IMPORTANT DESIGN PARAMETERS OF THE ANTENNA

Parameter	Value
Design Frequency	1.8 GHz
Dimensions	$L_o = W_o = 19.42$ mm, $W_1 = 3$ mm, $W_2 = 0.5$ mm, $L_f = 11$ mm, $L_s = 2$ mm, $L_f = 11$ mm
Substrate	FR4: $\epsilon_r = 4.3$, $h = 1.6$ mm, $\tan \delta = 0.02$

3. Results and Discussion

The proposed configuration simulation was done by utilizing CST Microwave studio environment for advancing the configuration parameters and the simulated reflection coefficients; input impedance and gain were investigated. For fixed antenna height of, $h = 1.6$ mm, $L_o = W_o = 19.42$ mm, the simulated return loss results of the proposed geometric antenna using FR4 substrate is shown in Fig. 2. However, there is a shift in the central frequency; the geometric underway follows the reflection coefficients shape. The little shift in the full recurrence being attributed to not acknowledging the disjunction between the insets fed line and the patch. Thus, it is distinguished that the data input impedance collapses similarly as the embed point is moved approaching the patch middle from these edges as contrasted with the coaxially probe fed encourage patch antennas. However, those scattering parameter studies have been utilized to infer hybrid Inset fed-quarter wave transformer feeding. The outcomes indicate that the information impedance matched the 50Ω impedance of the coaxial probe. Therefore, it was designed a square ring patch antenna which has slot in the center on the patch. The simulated directivity and gain of proposed antenna is demonstrated in Fig. 3 and 4 respectively, which is giving us the informational that antenna also have directional properties. The proposed design was fabricated on FR4 substrate material at frequency of 1.8 GHz. The simulated and measured matching return loss values are -21.726 dB and gain 2.3 dB respectively. However, the measured result indicates a little shifting of one percent in the centre frequency; close agreement in the reflection coefficient, sketch can be observed as shown in Fig. 5. It might have been recognized the electrical current movements at edge of the square slot specially near to the feeding point of the patch. Therefore, the input impedance matching at intervals of the feeding point and transmission line is important and must agree as shown in Fig. 6 and 7. Therefore, there is a percentage slight distinction between simulation and measurement outcomes due to fabrication or alternately test tolerances. The Table II indicates the layouts of the designed antenna and measurements parameters.

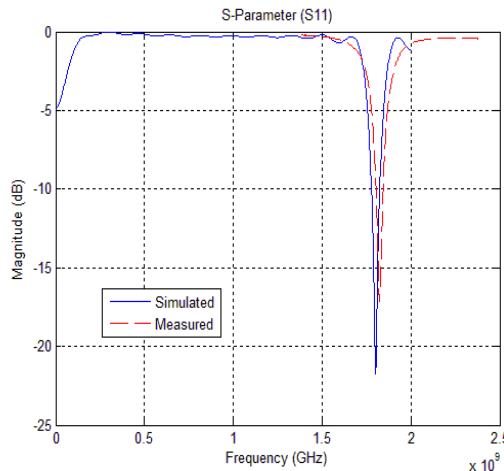


Fig. 2 : Simulated and measured reflection coefficients using FR4 substrate.

Table III PERFORMANCE OF THE DIELECTRIC SUBSTRATES

Substrate	S11	Directivity(dBi)	Gain(dB)
FR4	-24.85	6.58	2.304

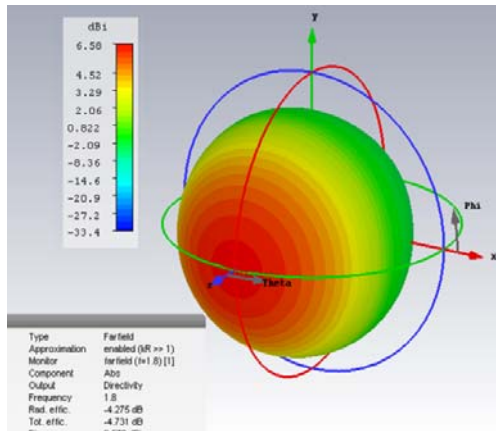


Fig. 3 : Directivity of Fairfield of Square Ring patch antenna at 1.8 GHz.

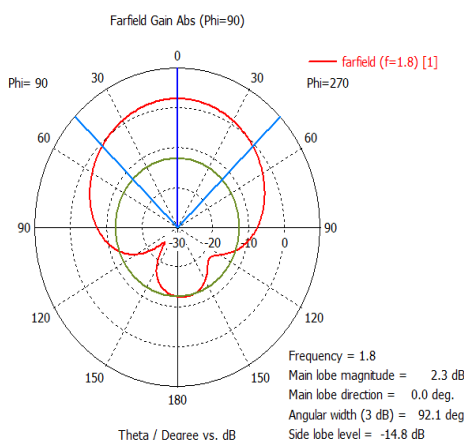


Fig. 4 : Gain of Square Ring patch antenna at 1.8 GHz

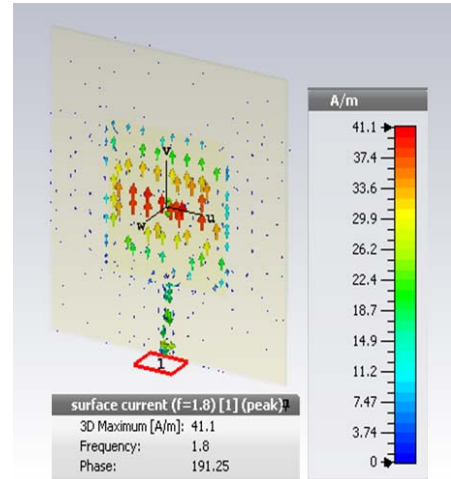


Fig. 5 : Square Ring Patch Surface Current Flow at 1.8GHz

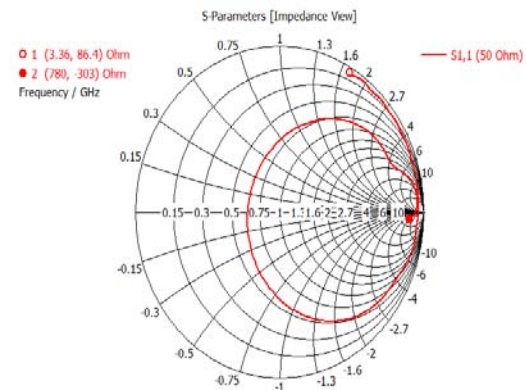


Fig. 6 : Simulated input impedance at 1.8 GHz

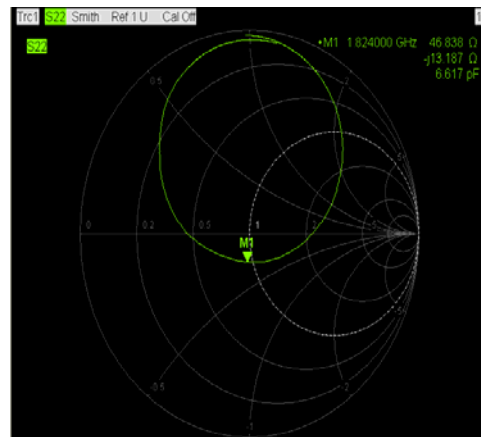


Fig. 7 : Measured input impedance at 1.8 GHz

Measured radiation pattern of square ring patch in E-plane and H-plane, the blue line is co-Polar, dotted red line is cross-polar component as shown in Fig. 8 and 9. The main purpose is to demonstrate the theory and to compare measurement with simulation results. Fig.10 displays the fabricated prototype of the proposed antenna

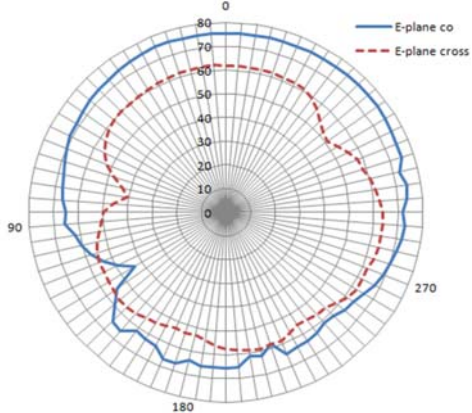


Fig. 8 Measured radiation pattern of square ring patch in E-plane, the blue line is co-Polar, dotted red line is cross-polar component

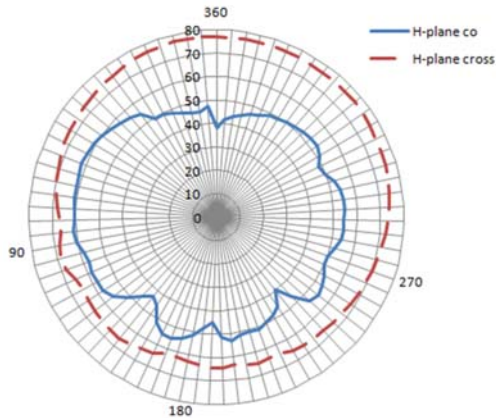


Fig. 9 : Measured radiation pattern of square ring patch in H-plane, the blue line is co-Polar, dotted red line is cross-polar component.

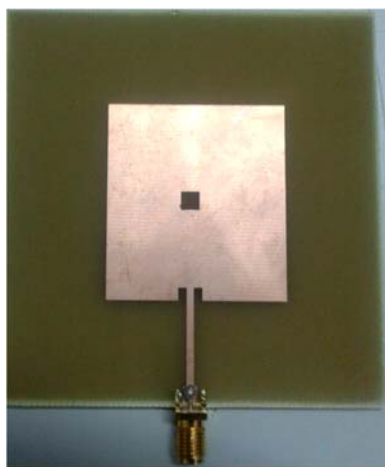


Fig. 10 : The fabricated prototype of the antenna.

4. Conclusion

This paper presented hybrid-feeding configuration by the addition of inset fed and quarter wave transformer-fed, which provided better impedance matching. The study of recent approaches of square ring slot design and their performance has been presented. In addition, the performance of FR4 substrate material has also been investigated thoroughly. The proposed configuration is the introduction of additional feeding method for antenna designers that provides better effect over the performance of the results, and will provide good agreement with simulations.

ACKNOWLEDGEMENTS

The authors would like to thank ORICC University Tun Hussein Onn Malaysia (UTHM) for supporting this work under Postgraduate Research Assistance Grant (GPPS) U585.

References

- [1] P. Tilanthe and P. Sharma, "Design of a single layer multiband microstrip square ring antenna," in *Applied Electromagnetics Conference (AEMC)*, 2009, 2009, pp. 1-4.
- [2] T. Samaras, A. Kouloglou, and J. Sahalos, "A note on the impedance variation with feed position of a rectangular microstrip-patch antenna," *IEEE Antennas and Propagation Magazine*, vol. 46, no. 2, pp. 90-92, 2004.
- [3] D. M. Pozar, "Microwave Engineering 3e," *Transmission Lines and Waveguides*, pp. 143-149, 2005.
- [4] W. Dou and W. Chia, "Small broadband stacked planar monopole," *Microwave and Optical Technology Letters*, vol. 27, no. 4, pp. 288-289, 2000.
- [5] C.-W. Ling, C.-Y. Lee, C.-L. Tang, and S.-J. Chung, "Analysis and application of an on-package planar inverted-F antenna," *IEEE transactions on antennas and propagation*, vol. 55, no. 6, pp. 1774-1780, 2007.
- [6] A. Kumar and M. Kumar, "Gain enhancement in a novel square microstrip patch antenna using metallic rings," in *Recent Advances and Innovations in Engineering (ICRAIE)*, 2014, 2014, pp. 1-4.
- [7] J. Puskely, A. Yarovoy, and A. Roederer, "Two-port dual-band microstrip square-ring antenna for radar applications," in *2016 10th European Conference on Antennas and Propagation (EuCAP)*, 2016, pp. 1-5.
- [8] W.-j. Lui, C.-h. Cheng, and H.-b. Zhu, "Improved frequency notched ultrawideband slot antenna using square ring resonator," *IEEE Transactions on Antennas and Propagation*, vol. 55, no. 9, pp. 2445-2450, 2007.
- [9] L. H. Weng, Y.-C. Guo, X.-W. Shi, and X.-Q. Chen, "An overview on defected ground structure,"

- Progress In Electromagnetics Research B*, vol. 7, pp. 173-189, 2008.
- [10] G.-L. Wu, W. Mu, D. Li, and Y.-C. Jiao, "Design of novel dual-band bandpass filter with microstrip meander-loop resonator and CSRR DGS," *Progress In Electromagnetics Research*, vol. 78, pp. 17-24, 2008.
- [11] B. Yuan, X. H. Zhang, Z. F. Hu, and G. Q. Luo, "An axial ratio beamwidth enhancement of patch antenna with digonal slot and square ring," *Microwave and Optical Technology Letters*, vol. 58, no. 3, pp. 672-675, 2016.
- [12] H. Majid, M. Rahim, R. Dewan, and M. Ismail, "Frequency reconfigurable square ring slot antenna," in *RF and Microwave Conference (RFM), 2015 IEEE International*, 2015, pp. 147-150.
- [13] A. Mumin, R. Alias, A. Awaleh, and R. A. Abdulhasan, "Assessment of microstrip patch antenna performance based on dielectric substrate," in *Computer, Communications, and Control Technology (I4CT), 2015 International Conference on*, 2015, pp. 468-471.

MINI REVIEW OF n-TYPE AND p-TYPE DOPED GaN THIN FILMS

Muliana Tahan¹, Nafarizal Nayan², Mohd Zainizan Sahdan², Anis Suhaili Bakri¹, Elfa Rizan Rizon¹, Siti Ashraf Abdullah¹, Yunus Sari³, Ahmad Shuhaimi Abu Bakar⁴, Ali Aldalbah⁵

¹Faculty of Electrical and Electronic Engineering, Universiti Tun Hussein Onn Malaysia (UTHM), 86400 Parit Raja, Batu Pahat, Johor Malaysia.

²Microelectronics and Nanotechnology- Shamsuddin Research Centre (MiNT-SRC), Institute of Integrated Engineering, Universiti Tun Hussein Onn Malaysia (UTHM), 86400 Parit Raja, Batu Pahat, Johor, Malaysia.

³Preston Shipyard Sdn. Bhd., KM9, Jalan Ranca-Ranca, P.O Box 82164, 87031, Wilayah Persekutuan Labuan.

⁴Low Dimensional Materials Research Centre, Department of Physics, Faculty of Science, University of Malaya, 50603 Kuala Lumpur, Malaysia.

⁵Chemistry Department, King Saud University, Riyadh 11451, Saudi Arabia.

Abstract: In this mini review, the n-type and p-type doping of gallium nitride (GaN) materials are discussed, based on the experimental works conducted by many researchers. Silane (SiH_4) and germane (GeH_4) are normally used as dopant materials source for used in Metal-Organic Vapor Phase Epitaxy (MOVPE) growth for n-type doping in group III nitrides. Silicon is standard dopant for n-type GaN as the activation energy is within 20 meV resulting donor state of the conduction band edge. P-type doping is more difficult to achieve due to hydrogen compensation, low hole mobility from the compound semiconductor itself and compensation native donor such as nitrogen vacancies that is easily formed during the growth when Fermi level is low. To have good p-type GaN, the high free hole concentration must excess 10^{20} cm^{-3} in doping combination. Based on the previous study of ionization energy, magnesium (200 meV) is the best p-type doping nowadays.

1. Introduction

Gallium nitride (GaN) is one of the III-nitride wide bandgap semiconductor commonly used in light emitting diodes (LED) and laser diode [1]. It has wurtzite crystal structure with wide bandgap of 3.45 eV, which corresponds to ultraviolet radiation (~360 nm). This make it as the best candidates for development of optoelectronic, high frequency and high power devices [2][3]. In order to create these devices, high quality of both n- and p-type doping of GaN are essential [4][5].

There are several well-known methods for growing and doping semiconductor materials such as Hydride Vapor Phase Epitaxy (HVPE) [6], Metal-Organic Phase Epitaxy (MOVPE) also known as Metal-Organic Chemical Vapor Deposition (MOCVD) [7][8][9], Molecular Beam Epitaxy (MBE) [10], Liquid Phase Epitaxy (LPE) [11], ion implantation [12], and sputtering [13].

The early method for growing and doping is HVPE which is made for development of silicon and germanium epitaxy [14][15]. The advantages of this method is high growth rate (~ 1 $\mu\text{m}/\text{min}$), near-equilibrium nature of the process which can be employed to generate low-defect material and lower cost than MOVPE because the precursor gas used such as ammonia (NH_3) and gallium trichloride (GaCl_3) are easily available in the market

[16]. However, it was difficult to achieve p-type doping by using this method. Meanwhile, MOVPE was undergo chemical vapor deposition process to deposit monocrystalline layer in single substrate. The disadvantage of HVPE (which is the difficulty to grow p-type doping) was overcome by MOVPE in thermal annealing function, often incorporated into the cooling sequence inside MOVPE reactors [17]. The disadvantages of MOVPE are it requires expensive and reactive precursor gas such as trimethylgallium (TMGa) and NH_3 and used high temperature at least 1100 °C in its process [18][19]. Moreover, A. Y. Cho and J. R. Arthur [20] mentioned that MBE growth is like “spray painting” the substrate crystal with layers of atom. In MBE process, the composition or impurity level in each layer is changing until desire structure is obtained. This technique has slow growth rate but much more easier to control the deposition rate [21][22]. Other method for doping is ion implantation technology followed by thermal annealing process [23][24]. This technique can also be used for doping but it can also damage the quality of crystallinity [25]. The recent and unconventional method for growth and doping is sputtering. Sputtering uses low temperature for deposition of thin films and doping, does not require thermal annealing process [26] and inexpensive method

[27]. In this review, the issue and current status of n-type and p-type doping in GaN nitrate are discussed.

2. Issues

Most crystal growth in III-nitrate such as GaN resulting n-type conductivity in natives population of vacancies and light element impurities in the nitrates [28]. In MOVPE process, doping is essential to obtain material with free electron concentrations and then reducing unwanted impurity incorporation to acceptable levels which is required for device such as LED. Silicon is almost ideal dopant for n-type GaN as the resulting donor state is within <20 meV of the conduction band edge [29]. A common silicon atom concentration in GaN based LED structure is about $5 \times 10^{18} \text{ cm}^{-3}$, equivalent to replacement about one every 9000 gallium atom [17].

Instead simplicity to achieve n-type conductivity in GaN, obtaining p-type conductivity in GaN is difficult to achieve [17]. One of the problem is low doping activation due to effect of chemical deactivation of acceptors hole by hydrogen atom bonding to the acceptors and high thermal activation energy of the acceptors itself [30]. However, Amano and Akasaki found a way to solve this problem using refinement of MOVPE to the point where compensation of free electrons become possible, using magnesium (Mg) as a dopant to GaN [31]. Then, Nakamura *et al.* demonstrate that p-type conductivity of GaN can be obtained from Mg using simple thermal annealing [32] resulting hole concentration of $3 \times 10^{17} \text{ cm}^{-3}$ and conductivity of $2 \Omega \text{ cm}^{-1}$ [32]. These values were still insufficient [32] since hole concentration should higher than 10^{19} cm^{-3} to fabricate good quality of blue LED [33].

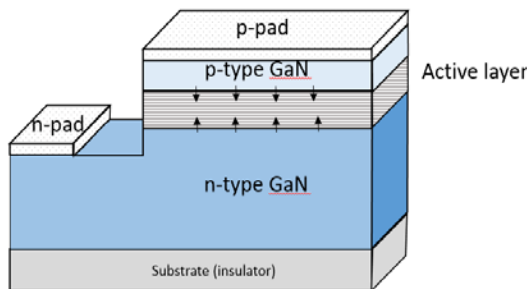


Figure 1: At forward-biased LED, n-type release negative electron and p-type release positive hole then combine at active layer thus release photons.

P-N junction which is known as diode is mainly used in LED, is created by placing n-type and p-type material in closed contact. Diffusion process occur in this p-n junction where mobile charges (holes) in p-type combine with mobile charges (electrons) in n-type. Holes concentration in p-type GaN doping region must be high to make sure electrons from donor can be caught successfully by the holes or acceptors and prevent the electrons from escape. Figure 1 shows basic structure of LED p-n junction. When current flow at forward biased, n-type GaN doping region release negative electron and

p-type GaN doping region release positive hole. In forward biased, the electron and hole combine at the active region. The hole energy is lower than electron energy, hence electron will lose energy to combine with the hole. The energy will lose in the form of photon or unit of light (photoluminescence). The amount of energy determine the frequency and colour of light depending on the type of material and process created by n-type and p-type materials.

GaN Material Doping

2.1 N-type Doping

Generally, GaN n-type doping can be obtained using group -IV atoms such as carbon (C), silicon (Si) and germanium (Ge) when they substitute for cation or group-VI atoms such as oxygen (O), sulphur (S) and selenium (Se) when they substitute nitrogen, (N). It was done by replacing the semiconductor atoms with any impurities from group IV and group VI that have same external electronic shell with one less electron which required for bonding. In particular, silane (SiH_4) and germane (GeH_4) are normally used as dopant source materials for used in MOVPE for group III nitrides. Both gases can be used either one as they are effectively used to induce the formation of free electrons in GaN materials [34]. Table 1 [34] shows the free concentration on GaN at room temperature. Silicon is chosen as doping in GaN due to its low cost and simple used (because Si doping atoms automatically activated during high temperature deposition of n-type GaN). On the other hand, Ge is chose for dopant in GaN because it does not cause to additional tensile stress induced for any Ge doping level [35][36].

Silicon is commonly used for n-dopant in GaN because amount of silicon to be doped during the growth can easily be adjusted. There are two ways for controlling the amount of silicon to be doped which was by varying the flow rate of silicon containing gases into the vapour phase reactor, or by direct control of evaporated silicon flux from the effusion cell in molecular beam epitaxy system. Based on previous research [32], free carrier concentration of Si in GaN is between the range of 10^{17} to $2 \times 10^{19} \text{ cm}^{-3}$ and the solubility of Si in GaN is 10^{19} cm^{-3} which is very high solubility. However, higher value of carrier concentration in dopant can affect the quality of materials as the materials start to deteriorate faster because of formation of tensile strain. The tensile strain that caused by Si doping can affect the thickness of deposited thin films [37].

For germanium doping, the free carrier concentration of Ge in GaN is $2 \times 10^{20} \text{ cm}^{-3}$ which show better surface morphology and lower effect tensile stress [34]. In more recent study by Fritze *et al.* [34] high n-type doping by Ge up to $2.9 \times 10^{20} \text{ cm}^{-3}$ of free carrier concentration shows no sign of mirror-like surface and material degradation. This Ge doping was proved to be successful in reaching high n-type doping on GaN because from this level of concentration, feasibility of GaN-based plasmonic detector is demonstrated and bulk carrier

plasma and surface plasma at infrared frequency can be seen [38].

Table 1: Source of dopant and its free carrier concentration after doping process using MOVPE.

Dopant	Free carrier concentration in doped GaN	Reference
SiH ₄	2x10 ¹⁹ cm ⁻³	[39]
GeH ₄	2.9x10 ²⁰ cm ⁻³	[34]

2.2 P-type Doping

Replacement of atom impurity from group II A and II B such as beryllium (Be), magnesium (Mg), zinc (Zn) and cadmium (Cd) on cation sites and group IV atom as nitrogen sites that has less one electron compared to the atom it replaces have ability to be shallow acceptor and induces p-type conductivity semiconductor. High free hole concentration is not easy to be achieved in GaN because hydrogen compensation [40], low hole mobility from the compound semiconductor itself [39] and compensation native donor such as nitrogen vacancies that is easily formed during the growth when Fermi level is low [41]. This issue can reduce the concentration of active acceptor in GaN doping. To have good p-type GaN, the high free hole concentration must excess 10²⁰ cm⁻³ in doping combination.

The earliest study to achieved p-type doping is using zinc (Zn) which is the standard dopant for gallium arsenide (GaAs) and gallium phosphate (GaP) for red and green LED at that time. However, it was not the best dopant for making p-type GaN for p-n junction for blue LED because of highly resistivity and self-compensation [42]. In fact, Zn doped GaN in GaAs LED at that time actually is not a p-n junction but metal insulator semiconductor (m-i-s) junction, which has an issue with high growth rate and strongly compensates the present donors in deposition of p-type GaN. It is difficult to control the thickness of insulating layer in mis type structure [39]. M-i-s junctions is majority carrier device produce electroluminescence using minority carrier tunneling from the metal [39]. Based on report by Pankove *et al.*, for Zn doped GaN using HVPE, the photoluminescent spectrum obtained by excitation using UV laser peaks is 2.4 eV and its width is about 350 meV at room temperature [43]. It is attributed to the injection of holes generated by breakdown at internal boundaries which indicates Zn attributed to forms a deep acceptors.

Nowadays, the best dopant for making p-type GaN for LED is Mg. It was start when Amano and Akasaki found that low-energy electron-beam irradiation (LEEBI) treatment radically lower the resistivity and enhance photoluminescence efficiency of Mg doped GaN growth using MOVPE [31][44][45]. Recent study for Mg doped GaN using MBE demonstrates MBE process can achieve high hole concentration and low resistivity of 4.5x10¹⁸ cm⁻³ and 1.3Ω cm at room temperature [46]. However, the major problem in both techniques is self-

compensation from Mg itself [47] which can reduce hole in p-type conductivity.

Other than Zn and Mg, beryllium, Be can also be dopant for GaN. It has been studied both theoretically [10][48] and experimentally [38] that beryllium can acquired shallow acceptor level for p doping in GaN. According to F. Bernardini *et al.* paper in 1997 [48], Be as potential to become a shallow acceptor in GaN but solubility of Be in GaN is low due to beryllium nitride (Be₃N₂) formation, so the hole concentrations is about 10¹⁷ cm⁻³ at room temperature. However, Be₃N₂ formation can be reduced by co-doping experiment with gallium oxide (Ga₂O₃), hence increase the activation energy (6.4 eV) and solve the issue. Therefore, Be and O can be incorporated simultaneously in large amounts into GaN. Recent experimentally studied in 2016 [49], high quality of Be doped GaN powder has been grown by reacting high purity Ga diluted alloys (Be-Ga) with ultra purity ammonia in a horizontal quartz tube reactor at 1200 °C. In that experiment, the photoluminescence emission spectra of the material GaN doped by Be is 3.39 eV at room temperature which is good candidates for enhancement of electroluminescence devices.

Table 2: Value of group II acceptors impurities in GaN.

Dopant	Ionization Energy (meV)	Emission Peak (meV)	Reference
Mg	200	220	[43][21]
Zn	550	350	[50]
Be	460	190	[51]

Table 2 shows the value of group II impurities in GaN. Based on the result of activation energy in the table, Mg (200 meV) is the best p type dopant because it can act as shallow acceptor. While ionization energy of both Be (550 meV) and Zn (460 meV) are too large to permit any p-type conductivity. Emission peak represent of photoluminescence from conduction band minimum of doped GaN to deep acceptor level. High value of emission is good in LED for lighting application because it can give bright visible light for users.

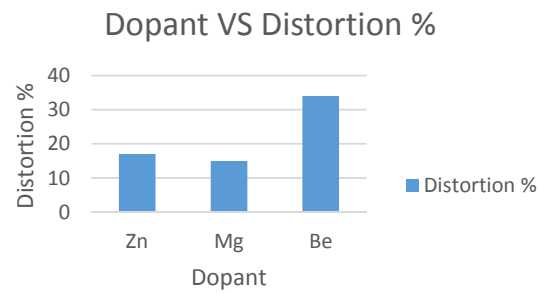


Figure 2: Distortion express in percentages represent of Ga-N bond length which is the change in bond length between the acceptors and closest neighbor nitrogen atom, in neutral charge of each acceptor.

Hole localization occurs in distortion (change in bond between acceptors and closest neighbor nitrogen atom) in neutral charge state. Based on the bar chart in Figure 2, Mg doped GaN have the lowest percentages of distortion which is 13%. This is due to encouragement of large local lattice distortion which cause the hole is localized on N atom neighboring the Mg impurity (Mg-N bond) [41]. Hence, reduced compensation native donor of nitrogen localization on Ga-N that is easily formed during the growth when Fermi level is low which can cause reducing the concentration of active acceptor in GaN doping. In other word, the bond length between Mg-N and Ga-N must be distorted and broke its symmetry so that hole vacancy (localization) can be created. Because of the large relaxation energy, the corresponding photoluminescence spectrum will also be broad. Without enabling symmetry breaking, the hole-localized lowest-energy configuration cannot be found. Distortion in Be doped GaN is 34%. It shows that Be doped Ga can lead to highly localized hole because of its smaller size than Mg. However, Be is not chosen as ideal dopant for GaN because the ionization energy is higher hence too large to permit any p-type conductivity. It is due to its smaller size that enable Be acts as deeper acceptor in doped GaN. The additional problem for Be doped GaN is because of self-compensation by Be interstitial [30][52] which cause Be acts as donor, not acceptor [53]. For Zn doped Ga, its distortion is 17%. But it cannot surpassed the effectiveness of Mg in p-type dopant because of the same reason for Be and due to high resistivity.

Summary

In this review, n-type and p-type doping GaN issues and materials were discussed. The current issues of doping in GaN were also reviewed. In general, n-type doping in GaN is easier to achieve because the crystal growth from III-nitrate itself can result in n-type conductivity. However, p-type has some difficulty to achieve due to hydrogen compensation, low hole mobility from the compound semiconductor itself, and compensation native donor such as nitrogen vacancies that is easily formed during the growth when Fermi level is low. In order to overcome this issue LEEBI treatment and thermal annealing using MOVPE are used. Today, new technology and way to improve efficiency of GaN doping is studied for high quality optoelectronic and high power device future.

Acknowledgement

This study is partially supported by Ministry of Higher Education Malaysia and Industrial Grant under the contract Vot A124: Preston Fund. Nafarizal acknowledges the financial support by CREST Malaysia through P28C1-17 and Ali Aldalbahi acknowledges the financial support by Deanship of Scientific Research, College of Science Research Centre, King Saud University.

References

- [1] D. Walker and M. Razeghi, "The development of nitride-based UV photodetectors," *Opto-Electronics Review*, vol. 8, no. 1, pp. 25–42, 2000.
- [2] Y. Arakawa, "Progress in GaN-based quantum dots for optoelectronics applications," *IEEE J. Sel. Top. Quantum Electron.*, vol. 8, no. 4, pp. 823–832, 2002.
- [3] H. Amano, "Development of GaN-based blue LEDs and metalorganic vapor phase epitaxy of GaN and related materials," *Prog. Cryst. Growth Charact. Mater.*, vol. 62, no. 2, pp. 126–135, 2016.
- [4] K. Yohannes and D. H. Kuo, "Growth of p-type Cu-doped GaN films with magnetron sputtering at and below 400 oC," *Mater. Sci. Semicond. Process.*, vol. 29, pp. 288–293, 2015.
- [5] M. R. Krames and R. D. Dupuis, "History, Development, and Applications of High-Brightness Visible Light-Emitting Diodes," *J. Light. Technol. Vol. 26, Issue 9, pp. 1154-1171*, vol. 26, no. 9, pp. 1154–1171, 2008.
- [6] H. Morkoç, "Comprehensive characterization of hydride VPE grown GaN layers and templates," *Mater. Sci. Eng. R Reports*, vol. 33, no. 5–6, pp. 135–207, 2001.
- [7] S. Surender, K. Prabakaran, R. Loganathan, S. Pradeep, S. Singh, and K. Baskar, "Effect of growth temperature on InGaN/GaN heterostructures grown by MOCVD," *J. Cryst. Growth*, vol. 468, no. xxxx, pp. 0–1, 2016.
- [8] H. M. Kim, T. W. Kang, and J. E. Oh, "Comparison of HVPE GaN films and substrates grown on sapphire and on MOCVD GaN epilayer," *Mater. Lett.*, vol. 46, no. 5, pp. 286–290, 2000.
- [9] R. Kirste, M. P. Hoffmann, E. Sachet, M. Bobea, Z. Bryan, I. Bryan, C. Nenstiel, A. Hoffmann, J. P. Maria, R. Collazo, and Z. Sitar, "Ge doped GaN with controllable high carrier concentration for plasmonic applications," *Appl. Phys. Lett.*, vol. 103, no. 24, pp. 14–18, 2013.
- [10] C. G. Van de Walle, S. Limpijumnong, and J. Neugebauer, "First-principles studies of beryllium doping of GaN," *Phys. Rev. B*, vol. 63, no. 24, p. 245205, 2001.
- [11] A. Denis, G. Goglio, and G. Demazeau, "Gallium nitride bulk crystal growth processes: A review," *Mater. Sci. Eng. R Reports*, vol. 50, no. 6, pp. 167–194, 2006.
- [12] J. I. Pankove and J. A. Hutchby, "Photoluminescence of ion-implanted GaN," *J. Appl. Phys.*, vol. 47, no. 12, pp. 5387–5390, 1976.
- [13] T. Kikuma, K. Tominaga, K. Furutani, K. Kusaka, T. Hanabusa, and T. Mukai, "Gan films deposited by planar magnetron sputtering," *Vacuum*, vol. 66, no. 3–4, pp. 233–237, 2002.

- [14] P. Hofmann, M. Krupinski, F. Habel, G. Leibiger, B. Weinert, S. Eichler, and T. Mikolajick, "Novel approach for n-type doping of HVPE gallium nitride with germanium," *J. Cryst. Growth*, vol. 450, pp. 61–65, 2016.
- [15] M. Iwinska, T. Sochacki, M. Amilusik, P. Kempisty, B. Lucznik, M. Fijalkowski, A. Khapuridze, G. Staszczak, I. Grzegory, M. Bockowski, and B. Gan, "Homoepitaxial growth of HVPE-GaN doped with Si," *J. Cryst. Growth*, 2016.
- [16] R. J. Molnar, W. Götz, L. T. Romano, and N. M. Johnson, "Growth of gallium nitride by hydride vapor-phase epitaxy," *J. Cryst. Growth*, vol. 178, no. 1–2, pp. 147–156, 1997.
- [17] I. M. Watson, "Metal organic vapour phase epitaxy of AlN, GaN, InN and their alloys: A key chemical technology for advanced device applications," *Coord. Chem. Rev.*, vol. 257, no. 13–14, pp. 2120–2141, 2013.
- [18] H. Wang, H. Sodabanlu, Y. Daigo, T. Seino, T. Nakagawa, and M. Sugiyama, "Initial growth control of GaN on Si with physical-vapor-deposition-AlN seed layer for high-quality GaN templates," *Appl. Phys. Express*, vol. 9, no. 5, 2016.
- [19] L. A. Template, H. Wang, Z. Lin, Y. Lin, W. Wang, and G. Li, "High-Performance GaN-Based LEDs on Si Substrates : The Utility of Ex Situ With Optimal Thickness," pp. 1–7, 2017.
- [20] A. Y. Cho and J. R. Arthur, "Molecular beam epitaxy," *Prog. solid state Chem.*, vol. 10, pp. 157–191, 1975.
- [21] U. Kaufmann, P. Schlotter, H. Obloh, K. Köhler, and M. Maier, "Hole conductivity and compensation in epitaxial GaN:Mg layers," *Phys. Rev. B - Condens. Matter Mater. Phys.*, vol. 62, no. 16, pp. 10867–10872, 2000.
- [22] J. K. Sheu and G. C. Chi, "The doping process and dopant characteristics of GaN," *J. Phys. Condens. Matter*, vol. 14, no. 22, pp. 657–701, 2002.
- [23] J. C. Zolper, R. J. Shul, A. G. Baca, R. G. Wilson, S. J. Pearton, and R. A. Stall, "Ion \square implanted GaN junction field effect transistor," *Appl. Phys. Lett.*, vol. 68, no. 16, pp. 2273–2275, 1996.
- [24] J. C. Zolper, H. H. Tan, J. S. Williams, J. Zou, D. J. H. Cockayne, S. J. Pearton, M. H. Crawford, and R. F. Karlicek, "Electrical and structural analysis of high-dose Si implantation in GaN," *Appl. Phys. Lett.*, vol. 70, no. 20, pp. 2729–2731, 1997.
- [25] H. Tsuge, K. Ikeda, S. Kato, T. Nishimura, T. Nakamura, and K. Kuriyama, "Impact of Mg-ion implantation with various fluence ranges on optical properties of n-type GaN," *Nucl. Instruments Methods Phys. Res.*, vol. 409, pp. 50–52, 2017.
- [26] T. Tran, A. Tuan, D. Kuo, A. Daniel, and G. Li, "Electrical properties of RF-sputtered Zn-doped GaN films and p -Zn-GaN / n -Si hetero junction diode with low leakage current of 10 Å 9 A and a high rectification ratio above 10 5," *Mater. Sci. Eng. B*, vol. 222, pp. 18–25, 2017.
- [27] W. Y. Pang, I. Lo, S. Wu, Z. X. Lin, C. H. Shih, Y. C. Lin, Y. C. Wang, C. H. Hu, and G. Z. L. Hsu, "Growth of wurtzite and zinc-blende phased GaN on silicon (100) substrate with sputtered AlN buffer layer," *J. Cryst. Growth*, vol. 382, pp. 1–6, 2013.
- [28] J. Wu, "When group-III nitrides go infrared: New properties and perspectives," *J. Appl. Phys.*, vol. 106, no. 1, pp. 1–27, 2009.
- [29] O. Ambacher, "Growth and applications of group III-nitrides," *Journal of Physics D: Applied Physics*, vol. 31, no. 20, pp. 2653–2710, 1998.
- [30] W. Götz, R. S. Kern, C. H. Chen, H. Liu, D. A. Steigerwald, and R. M. Fletcher, "Hall-effect characterization of III-V nitride semiconductors for high efficiency light emitting diodes," *Mater. Sci. Eng. B Solid-State Mater. Adv. Technol.*, vol. 59, no. 1–3, pp. 211–217, 1999.
- [31] H. Amano, M. Kito, K. Hiramatsu, and I. Akasaki, "P-Type Conduction in Mg-Doped GaN Treated with Low-Energy Electron Beam Irradiation (LEEBI)," *Jpn. J. Appl. Phys.*, vol. 28, no. Part 2, No. 12, pp. L2112–L2114, 1989.
- [32] N. Shuji, M. Takashi, and S. Masayuki, "Si- and Ge-Doped GaN Films Grown with GaN Buffer Layers," *Jpn. J. Appl. Phys.* Vol. 31, pp. 2883–2888, 1992.
- [33] H. Okumura, D. Martin, and N. Grandjean, "Low p -type contact resistance by field-emission tunneling in highly Mg-doped GaN," *Appl. Phys. Lett.*, vol. 109, no. 25, pp. 1–6, 2016.
- [34] S. Fritze, A. Dadgar, H. Witte, M. Bügler, A. Rohrbeck, J. Bläsing, A. Hoffmann, and A. Krost, "High Si and Ge n-type doping of GaN doping - Limits and impact on stress," *Appl. Phys. Lett.*, vol. 100, no. 12, pp. 1–4, 2012.
- [35] M. A. Moram, M. J. Kappers, F. Massabuau, R. A. Oliver, and C. J. Humphreys, "The effects of Si doping on dislocation movement and tensile stress in GaN films," in *Journal of Applied Physics*, 2011, vol. 109, no. 7.
- [36] J. Xie, S. Mita, A. Rice, J. Tweedie, L. Hussey, R. Collazo, and Z. Sitar, "Strain in Si doped GaN and the Fermi level effect," *Appl. Phys. Lett.*, vol. 98, no. 20, pp. 96–99, 2011.
- [37] L. T. Romano, C. G. Van de Walle, J. W. Ager, W. Götz, and R. S. Kern, "Effect of Si doping on strain, cracking, and microstructure in GaN thin films grown by metalorganic chemical vapor deposition," *J. Appl. Phys.*, vol. 87, no. 11, pp. 7745–7752, 2000.
- [38] C. C. Yu, C. F. Chu, J. Y. Tsai, and S. C. Wang, "Investigation of beryllium implanted P-type GaN," *Mater. Sci. Eng. B Solid-State Mater. Adv. Technol.*, vol. 82, no. 1–3, pp. 82–84, 2001.
- [39] P. Pampili and P. J. Parbrook, "Doping of III-

- [40] nitride materials," *Mater. Sci. Semicond. Process.*, vol. 62, no. October 2016, pp. 180–191, 2017.
- [41] W. Götz, N. M. Johnson, J. Walker, D. P. Bour, and R. A. Street, "Activation of acceptors in Mg-doped GaN grown by metalorganic chemical vapor deposition," *Appl. Phys. Lett.*, vol. 68, no. 5, pp. 667–669, 1996.
- [42] S. Lany and A. Zunger, "Dual nature of acceptors in GaN and ZnO: The curious case of the shallow MgGa deep state," *Appl. Phys. Lett.*, vol. 96, no. 14, pp. 1–3, 2010.
- [43] S. Nakamura, N. Iwasa, M. Senoh, and T. Mukai, "Hole compensation mechanism of p-type GaN films," *Jpn. J. Appl. Phys.*, vol. 31, pp. 1258–1266, 1992.
- [44] J. I. Pankove, E. A. Miller, D. Richman, and J. E. Berkeyheiser, "Electroluminescence in GaN," *Journal of Luminescence*, vol. 4, no. 1, pp. 63–66, 1971.
- [45] S. Nakamura, "Background story of the invention of efficient blue InGaN light emitting diodes (Nobel Lecture)," *Ann. Phys.*, vol. 527, no. 5–6, pp. 335–349, 2015.
- [46] I. Akasaki, "Key inventions in the history of nitride-based blue LED and LD," *J. Cryst. Growth*, vol. 300, no. 1, pp. 2–10, 2007.
- [47] S. D. Burnham, G. Namkoong, D. C. Look, B. Clafin, and W. A. Doolittle, "Reproducible increased Mg incorporation and large hole concentration in GaN using metal modulated epitaxy," *J. Appl. Phys.*, vol. 104, no. 2, 2008.
- [48] A. Uedono, M. Malinverni, D. Martin, H. Okumura, S. Ishibashi, and N. Grandjean, "Vacancy-type defects in Mg-doped GaN grown by ammonia-based molecular beam epitaxy probed using a monoenergetic positron beam," *J. Appl. Phys.*, vol. 119, no. 24, 2016.
- [49] F. Bernardini, V. Fiorentini, and A. Bosin, "Theoretical evidence for efficient p-type doping of GaN using beryllium," *Appl. Phys. Lett.*, vol. 70, no. 22, pp. 2990–2992, 1997.
- [50] R. García-Gutiérrez, A. Ramos-Carrasco, D. Berman-Mendoza, G. A. Hirata, O. E. Contreras, and M. Barboza-Flores, "Photoluminescence enhancement from GaN by beryllium doping," *Opt. Mater. (Amst.)*, vol. 60, pp. 398–403, 2016.
- [51] J. L. Lyons, A. Janotti, and C. G. Van De Walle, "Impact of group-II acceptors on the electrical and optical properties of GaN," *Jpn. J. Appl. Phys.*, vol. 52, no. 8 PART 2, pp. 1–5, 2013.
- [52] F. B. Naranjo, E. Calleja, Z. Bougrioua, A. Trampert, X. Kong, and K. H. Ploog, "Efficiency optimization of p-type doping in GaN:Mg layers grown by molecular-beam epitaxy," *J. Cryst. Growth*, vol. 270, no. 3–4, pp. 542–546, 2004.
- [53] S. Limpijumnong and C. Van de Walle, "Diffusivity of native defects in GaN," *Phys. Rev. B*, vol. 69, no. 3, p. 35207, 2004.
- [54] H. T. Wang, L. S. Tan, and E. F. Chor, "Study of activation of beryllium implantation in gallium nitride," *J. Cryst. Growth*, vol. 268, no. 3–4 SPEC. ISS., pp. 489–493, 2004.

SURFACE MORPHOLOGY AND TOPOGRAPHY OF NTO THIN FILMS DEPOSITED VIA MAGNETRON SPUTTERING AT VARIOUS OXYGEN CONCENTRATIONS

Siti Ashraf Abdullah¹, Mohd Zainizan Sahdan^{1,2}, Nafarizal Nayan¹, Hashim Saim¹, Anis Suhaili Bakri¹, Sawsan Abdullah Abduljabbar¹, Cik Rohaida Cik Hak³, Feri Adriyanto⁴

¹ Microelectronic and Nanotechnology-Shamsuddin Research Centre (MiNT-SRC), Universiti Tun Hussein Onn Malaysia, 86400 Parit Raja, Batu Pahat Johor, Malaysia.

² Geochem Sdn Bhd, Taman Universiti, 86400 Parit Raja, Batu Pahat Johor, Malaysia

³ Malaysian Nuclear Agency, Bangi, Kajang 43000, Selangor, Malaysia

⁴ Department of Physics, Sebelas Maret University, 57126 Surakarta, Indonesia

Abstract: Nb doped TiO₂ (NTO) thin films were sputtered on cleaned glass substrate by DC and RF magnetron sputtering system. The oxygen concentration condition is varied at 2, 5, 8, and 10 sccm. The effect of oxygen doping on morphology and topography has been investigated with various characterization method, namely FE-SEM, AFM, and EDX. The oxygen doping increase the cluster particles on film surface, also resulting in increasing the grain size in AFM result. Besides, sample deposited at 5 sccm shows significant effect to photocatalytic activity which is it has lowest grain size and highest roughness, indicating that this sample has large surface area and high light absorption.

Keywords: TiO₂, photocatalyst, Nanomaterials, Inorganic semiconductor

1. Introduction

Niobium-doped TiO₂ (NTO) is acknowledged as transparent conducting oxide (TCO) and receives a special attention among researchers due to its good electrical performance [1]. Niobium become a favor transition metal as doping material into TiO₂ due to its ionic radius of Nb⁵⁺ slightly higher than ionic radius for Ti⁴⁺ which is 0.064 nm and 0.0605 nm respectively [2]. Therefore, additional carrier of electron could be generated from this reaction and allowed it to do reduction reaction on photocatalytic process.

The spatial extension of NTO surface is very important factors to increase the efficiency of the photocatalytic process. The performance of NTO thin films as photocatalyst is limit due to photo-generation of exciton and recombination. This effect is influenced by morphology and composition of the material [3]. Therefore, large surface areas need to be prepared to efficiently absorb the incident light from UV light sources. Increasing surface area could be achieve by increasing the surface roughness, height and frequency of the surface topographies [4]. Jia *et al.* reported that the morphologies of smaller grain size shows high photoactivity, it is also due to higher surface area that could adsorbed more reactive species [5].

The most selective deposition method is physical deposition and one of it is the magnetron sputtering system. Magnetron sputtering system has high-purity films, and excellent uniformity on large-area deposition [6]. Besides, the parameter of deposition condition is easily to control such as RF and DC power, deposition time, substrate temperature, working pressure and oxygen partial pressure. This parameter also influence the composition and structure of NTO thin films, thus gives effect to photocatalytic properties of NTO thin films.

2. Experiment

NTO thin films were prepared by DC and RF Magnetron Sputtering machine using Nb and TiO₂ target. First of all, the Microscope glass substrate at 2.5cm x 2.5cm area was cut using diamond cutter. Then, cleaning process has been done using acetone, ethanol and deionize water in ultrasonic bath for 10 minutes. Lastly, the substrate was dry by nitrogen gas. The sputtering chamber is initially set at ultra-high vacuum condition up to 5×10^{-6} Torr by turbo molecular pump. The deposition process parameter is 200 W RF power, 20 W DC power, 5 mTorr working pressure at 100 sccm Ar gas, 90 minute deposition time and 6 rpm rotational substrate holder. Various amount of oxygen which is 2, 5, 8 and 10 sccm is introduced to study the effect of oxygen doping into TiO₂.

thin films [7]. Lastly, all NTO thin films were post annealed at 500 °C for 1 hour. The effect on surface morphology and topography was studied by Field Emission Scanning Electron Microscopy (FE-SEM), and Atomic Force Microscopy (AFM). The composition of NTO films was confirmed with Energy Dispersive X-ray (EDX).

3. Results and Discussion

Thin films surface is one of the important characteristic for photocatalytic activities which also influence the optical and electrical properties. The surface morphology of samples was studied by FE-SEM analysis. Fig. 1 shows FE-SEM images at different oxygen concentration at 2, 5, 8 and 10 sccm. The main image is for 30 nm scales, 200x magnification and inset images at 100 nm scale and 150x magnification. It can be seen that all samples shows a good particles distribution and could be consider as fairly uniform granular structure. At oxygen concentration 8 sccm, the film starts to shows some agglomeration in certain places at both magnification images.

On the other hand, at 10 sccm oxygen concentration the agglomeration clearly shown at 200x magnification, while in inset image only shows a well particles distribution film. We believe that the agglomeration of particles on films might be due to interaction between Nb and O, hence producing NbO cluster as reported in literature [1]. FE-SEM images also shows the increased in grain size with increasing the oxygen concentration.

All samples contain Ti, O and Nb element with different intensity, the EDX spectra can be seen in fig. 2 and the weigh percent of all elements has been listed in table 1. It can be seen that, oxygen is three times higher

than Ti and two times higher than Nb, indicating that the films is in non-stoichiometric ratio. This values also explained that, this film might be contain NbO which is become cluster on film surface as discuss at FE-SEM images.

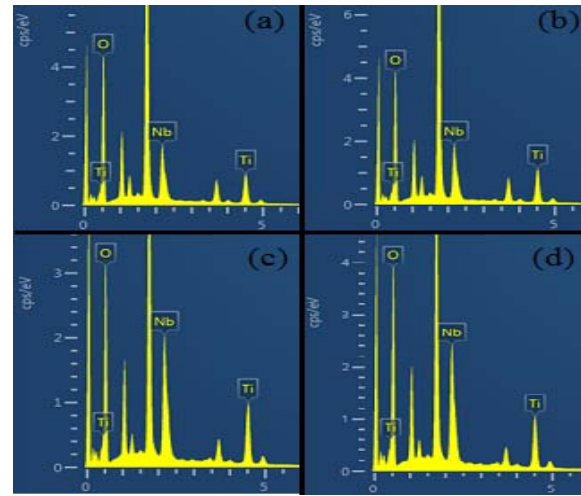


Fig 2. EDX spectra for O, Ti and Nb elements in NTO thin films for (a) 2, (b) 5, (c) 8 and (d) 10 sccm oxygen concentration

Table 1 EDX analysis of weight percent of O, Ti and Nb elements for samples 2, 5, 8 and 10 sccm.

Element	Weight percent (Wt%)			
	2sccm	5sccm	8sccm	10sccm
O	62.14	59.23	53.32	54.76
Ti	16.10	18.53	18.89	17.06
Nb	21.75	22.24	27.79	28.19

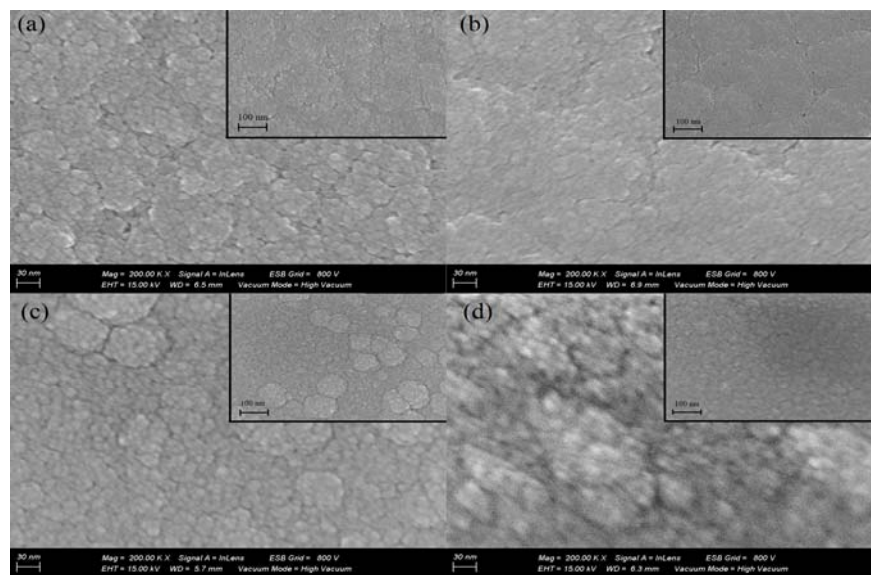


Fig. 1 FE-SEM images at 30 nm scale, 200x magnification and inset images at 100 nm scale 150x magnification of different O₂ concentration at (a) 2 sccm, (b) 5 sccm, (c) 8 sccm and (d) 10 sccm

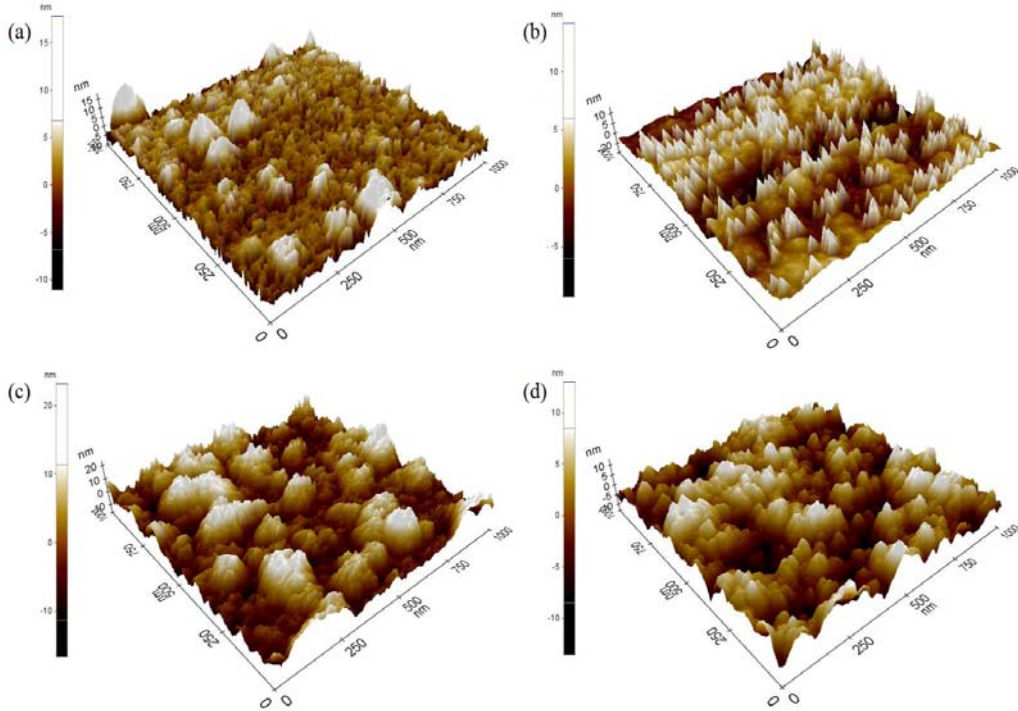


Fig. 3 AFM images for oxygen concentration at (a) 2 sccm, (b) 5 sccm, (c) 8 sccm and (d) 10 sccm

Table 2: AFM result of average grain size, RMS roughness and roughness average for NTO deposited at different oxygen concentration.

Oxygen concentration (sccm)	Average grain size (nm)	RMS roughness, R_q (nm)	Roughness average, R_a (nm)
2	34.52	3.46	2.69
5	34.55	7.83	5.54
8	39.93	5.82	4.75
10	43.39	4.32	3.49

Fig. 3 exhibits the 3D AFM topography images for $1\mu \times 1\mu$ of the surface morphology of NTO thin films for 2 to 10 sccm oxygen concentration. In the case of films, less uniform surface morphology was observed. However, as can be seen in rough eyes, increased the oxygen concentration gives slightly increase in grain size with agglomeration look. As can be seen, the sample deposited at 5 sccm is rough with equally grain distribution on film surface. On the other hand, sample deposited at 8 and 10 sccm shows broad hump grain with expectation, it has larger grain size as compared to other samples.

Evidently, oxygen doping during deposition affected the surface roughness as list out in table 2. The root mean square roughness values (R_q) and roughness average (R_a) is recorded, and the value of R_q is 3.46, 7.83, 5.82, and 4.32 for 2, 5, 8, and 10 respectively. It clearly showed that sample 5 sccm gives higher roughness as compares to other samples. This rough surface of NTO

nanostructures might increase the surface area, hence the photo-scattering efficiency would also increase [8].

However, roughness did not influence the grain size, as can be seen the grain size is increase by increasing the oxygen concentration. Indicating that, oxygen doping could produce more particles cluster that cause by Ti or Nb, hence increase the grains formation. This result is corresponding with FE-SEM images that show some particles cluster as increase the oxygen concentration during deposition process. Therefore, it can be noted that, 5 sccm oxygen concentration is the optimum oxygen doping into NTO thin film for this study.

4. Summary

Nb doped TiO_2 (NTO) has been successfully deposited by DC and RF magnetron sputtering system. The effect of oxygen doping during deposition process were investigated. By analyzed the FE-SEM images, we found that the agglomeration of particles occurred by increasing the oxygen concentration. This observation was supported by AFM result which proved that the occurrence of agglomeration by grain size calculation in AFM machine. It shows that the grain size is increase by increasing the oxygen concentration. Besides, sample deposited at 5 sccm shows higher roughness, lowest grain size. Indicating that, this sample has large surface area, and high light absorption. However, other observations need to be done for further study about surface characterization to study the performance of photocatalytic activity.

Acknowledgement

This work has been financially supported by Fundamental Research Grant Scheme (FRGS) Vot. 1536 from Universiti Tun Hussein Onn Malaysia (UTHM) and Ministry of Higher Education Malaysia. The experiment has been done at Mint-SRC UTHM laboratory.

References

- [1] J. Of, T. H. E. American, and C. Society, "Niobium-Doped Titania Photocatalyst Film Prepared via a Nonaqueous Sol-Gel Method," *Am. Ceram. Soc.*, no. July 2015, pp. 1–5, 2013.
- [2] J. Yang, X. Zhang, C. Wang, P. Sun, L. Wang, B. Xia, and Y. Liu, "Solar photocatalytic activities of porous Nb-doped TiO₂ microspheres prepared by ultrasonic spray pyrolysis," *Solid State Sci.*, vol. 14, no. 1, pp. 139–144, Jan. 2012.
- [3] D. a H. Hanaor, G. Triani, and C. C. Sorrell, "Morphology and photocatalytic activity of highly oriented mixed phase titanium dioxide thin films," *Surf. Coatings Technol.*, vol. 205, no. 12, pp. 3658–3664, 2011.
- [4] a P. Xagas, E. Androulaki, A. Hiskia, and P. Falaras, "Preparation , fractal surface morphology and photocatalytic properties of TiO₂ films," vol. 357, pp. 173–178, 1999.
- [5] Jia-Guo Yu, Huo-Gen Yu, Bei Cheng, Xiu-Jian Zhao, Jimmy C. Yu, and Wing-Kei Ho, "The Effect of Calcination Temperature on the Surface Microstructure and Photocatalytic Activity of TiO₂ Thin Films Prepared by Liquid Phase Deposition," *J. Phys. Chem. B*, vol. 107, no. 50, pp. 13871–13879, 2003.
- [6] B. Barrocas, O. C. Monteiro, M. E. Melo Jorge, and S. Serio, "Photocatalytic activity and reusability study of nanocrystalline TiO₂ films prepared by sputtering technique," *Appl. Surf. Sci.*, vol. 264, pp. 111–116, 2013.
- [7] S. a. Abdullah, M. Z. Sahdan, N. Nafarizal, F. Adriyanto, H. Saim, S. N. M. Tawil, and a. S. Bakri, "Optimization of oxygen on Nb-doped TiO₂ using DC and RF magnetron sputtering using composite and metal target," *AIP proceeding*, p. 030112, 2017.
- [8] A. M. Selman, Z. Hassan, and M. Husham, "Structural and photoluminescence studies of rutile TiO₂ nanorods prepared by chemical bath deposition method on Si substrates at different pH values," *Measurement*, vol. 56, pp. 155–162, 2014.

EFFECT ON STRUCTURAL AND MORPHOLOGICAL PROPERTIES OF ALUMINUM THIN FILM AT DIFFERENT SUBSTRATES DEPOSITED BY VACUUM THERMAL EVAPORATION

Kusnanto Mukti Wibowo¹, Mohd. Zainizan Sahdan^{1,*}, Nafarizal Nayan¹, Yunus Sari², Zailani Mansor²

¹Microelectronics and Nanotechnology Shamsuddin Research Center (MiNT-SRC)

Universiti Tun Hussein Onn Malaysia, Parit Raja, Batu Pahat 86400, Malaysia.

²Preston Shipyard Sdn Bhd, 87031, Labuan, Malaysia

Abstract: This paper studied influence on structural and morphological properties of aluminum (Al) thin films at different substrates such as amorphous substrate (glass), ITO coated glass, and silicon (100) substrate (p-type and n-type) by using vacuum thermal evaporation with base vacuum about 6.4×10^{-3} Pa. Thin film deposited by physical thermal evaporation allows vaporized particle to travel directly to the substrate with directional stage, hence provides poor coverage or lack of control the atoms. The films were analyzed with X-ray diffraction (XRD), field emission scanning electron microscope (FESEM), and atomic force microscopy (AFM). X-ray diffraction (XRD) spectra shows the absence of impurity peak, high crystallinity index (CI) up to 88%, and high quality of aluminum crystal due to the low of full width at half maximum (FWHM) value about 0.2362 on silicon n-type substrate. FESEM image reveals that all aluminum samples have a uniform size and hillock structure. The AFM images shows grainy morphology of aluminum films on different substrate. Furthermore, all films possess fairly smooth surface roughness in the range of 7 to 12 nm.

Keywords: Thin film, aluminum, thermal evaporation, nanomaterial

1. Introduction

Aluminum (Al) is the most abundant metal in the earth's crust and the third most abundant element. Aluminum is a metallic compound that has silvery white in color and low melting point of 600°C. Compare to other metals, aluminum has several advantages such as light weight, good adherence to glass, good reflectance and corrosion resistance. Aluminum thin film has many applications such as thin film transistors [1], flat panel displays [2], solar cells [3], optical mirrors [4], etc.

Many techniques have been used to deposit Al on a substrate, such as sputtering [5], electron beam evaporation [6], thermal evaporation [7], atomic layer deposition [8]. Compare to others physical vapor deposition (PVD) technique, thermal evaporation is good enough to deposit Al, since it has a low melting point. Moreover, thermal evaporation is the most cost-effective and the simplest method.

The structure of solid state material influences the properties of its material, such as conductivity, lifetime, refraction index, absorption coefficient, etc. As we know, atoms which are arranged in crystal posses long range order and symmetry. However, even in crystal there are many irregularities, the defects are always present in solids, like thin films. For example, the displacement of

one atom from the crystal lattice creates dangling bonds at several neighboring atoms by breaking their bonds. Thus, by knowing the structural properties of Al films in different substrates, it can enhance the quality of the microelectronic device that utilize Al.

2. Experimental method

Thermal vacuum evaporator (Model: Ulvac Kiko VPC-061) was used to deposit Al films on different substrates, glass, ITO, and Silicon (p-type and n-type). Before the deposition process, the glass and ITO substrates were cleaned ultrasonically with acetone and ethanol for 10 minutes each, after that rinsed with deionized water (DI water) to remove contamination from the surface. Then, nitrogen gas was blown over the surface for drying. While silicon substrates were cleaned using hydrofluoric acid (HF) and washed with DI water, then dried with nitrogen gas. Tungsten boat was used to evaporate the high purity of Al wire (99.99%). Al target was deposited in a vacuum chamber with base pressure of $\sim 6.4 \times 10^{-3}$ Pa. The current supply is turned on and increased gradually from 0 until 35 Ampere that result in sufficient heat to melt the target.

The SEM imaging of the evaporated Al thin films was performed with FE-SEM, Model: JEOL JSM-7600F.

The structural properties were carried out using X-ray diffraction system (XRD, Model: Panalytical X'Pert3 Powder) with Cu-K α 1 radiation source, $\lambda = 1.5406 \text{ \AA}$. The crystallographic analysis and peak phase conduct with HighScore plus software. The diffraction patterns recorded by varying the diffraction angle (2θ) from 20°–80°. Surface morphology of the samples was performed using AFM system, Model: XE-100 Park Series.

3. Results and Discussion

Figure 1 shows the XRD pattern for the Al films deposited on different substrates. Aluminum peak shows orientation in the (111), (200), (220), and (311) for all substrates. The parameters of crystal have equal value of $a = b = c = 4.048 \text{ \AA}$ for glass and silicon n-type, 4.046 \AA for ITO, and 4.049 \AA for silicon p-type, that is indexed to the cubic phase. The lattice constant of aluminum on all substrates is very close to the bulk of 0.4049 nm , thus the Al film is totally relaxed. The absence of impurity peaks in all substrates suggests the high purity of the aluminum.

The value of crystallinity index (CI_{XRD}) of all samples is high enough up to ~88 % that calculated by using formula:

$$CI = \frac{I_{111} - I_{311}}{I_{111}} \times 100\% \quad (1)$$

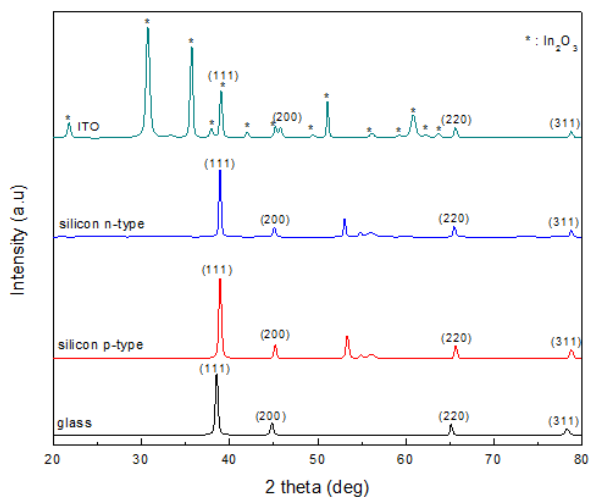


Figure 1. XRD pattern of Al on different substrate

The CI of aluminum on the glass substrate shows the highest value of 88.42%, in contrast to CI on ITO that has the lowest value of 84.08%. The high crystallinity also means striving to attain single crystallinity implying being defect free.

The amorphous substrate, glass hasn't shown any peak other than Al peaks, which is a peak mostly corresponds to the present of crystal. Therefore, there are only peaks of aluminum that occur on Al thin film on glass substrate. While on the ITO substrate occurs several peaks of In₂O₃ that is indicated the presence of In₂O₃ crystal. The same matter was also occurring on aluminum deposited on the silicon substrate, where the crystal peak background of the silicon substrate was appeared. Al film on a silicon substrate (n-type) shows the best quality of crystal compared to deposit on others substrate, since it has the lowest value of FWHM of 0.2362 \AA .

FE-SEM images of the aluminum films as shown in Figure 2, generally exhibits a uniform surface. It can be seen the films have a grainy surface structure with individual grains clearly defined and separated by voids for all substrates. The grains have almost uniform in size, and there are several hillocks protruding out from the film surface. There is almost no significant difference among them. Deposition by physical method have tendency result in uniform surface indeed.

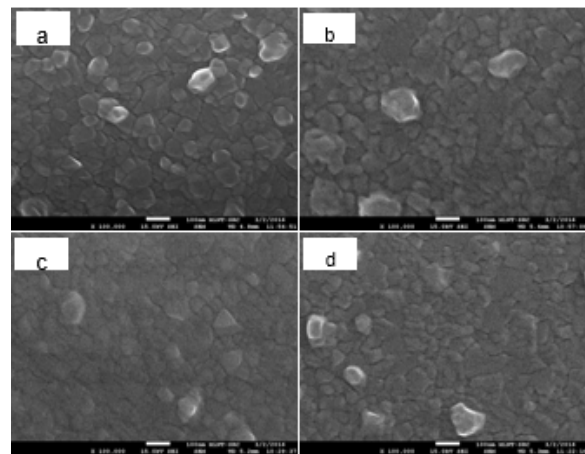


Figure 2. FESEM images of aluminum films deposited by thermal evaporation on (a) glass, (b) ITO, (c) silicon p-type, and (d) silicon n-type

Table 1. XRD data of Al thin films on different substrates

Substrate	Highest Peak (2theta)	FWHM (deg)	a (\AA)	b (\AA)	c (\AA)	Crystallite size, D (nm)	Crystallinity index (%)
Glass	38.5034	0.3247	4.048	4.048	4.048	29.785	88.42
ITO	38.5744	0.2952	4.046	4.046	4.046	32.908	84.08
Si (p-type)	38.4700	0.3247	4.049	4.049	4.049	29.782	86.50
Si (n-type)	38.4633	0.2362	4.048	4.048	4.048	41.694	87.53

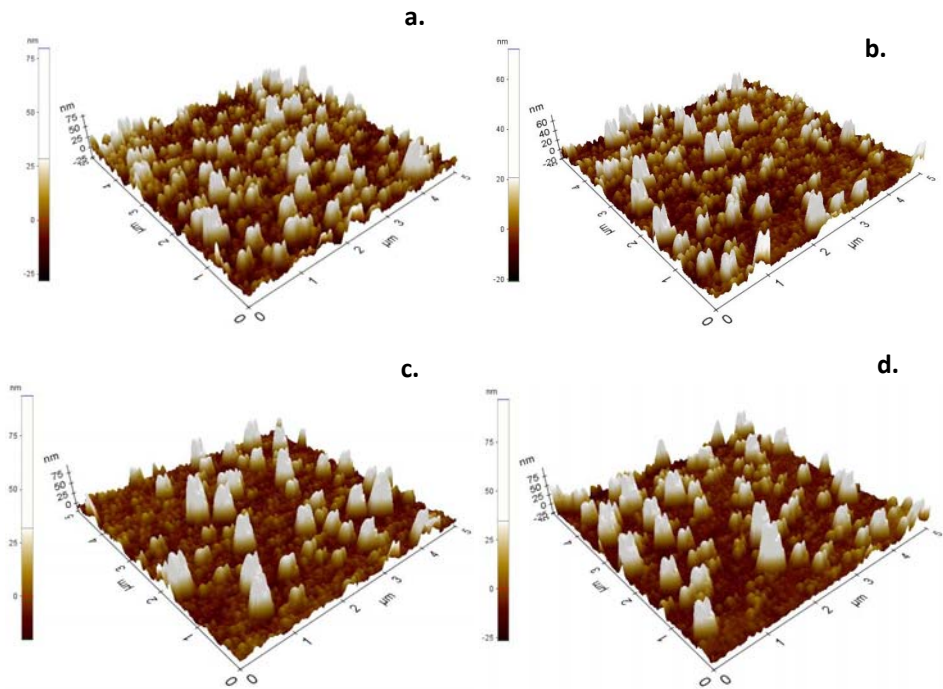


Figure 3. AFM images ($5 \times 5 \mu\text{m}^2$) of Al films deposited on (a) glass, (b) ITO, (c) silicon p-type, and (d) silicon n-type

Figure 3 reveals the AFM images of Al deposited on different substrate with a spot size of $5 \times 5 \mu\text{m}$. The surface morphology of thin films, exhibits a grainy morphology. From the Figure 3, it can be observed that all samples possess fairly smooth surface with roughness about 10 nm. This is believed because the directional line-of-sight deposition nature of thermal evaporation technique that normally results in smooth surfaces rather than rough surfaces. The roughness of the film which is deposited by physical vapour deposition correlates well with the roughness of the bare substrates.

Table 2. Surface roughness and grain size of thin Al films deposited on different substrates

Substrate	Grain size (nm)	Roughness (nm)
Glass	152.835	10.226
ITO glass	164.814	7.218
Silicon (p-type)	163.020	12.805
Silicon (n-type)	157.870	10.750

From the Table 2. It can be seen that the films deposited on silicon (p-type and n-type) are rougher than deposited on glass and ITO. Surface roughness of metal thin films is also known to influence their properties. In

related with the process of nucleation and coalescence of the deposited aluminum atoms, aluminum crystallites (grain) formed by aluminum atoms that are adsorbed onto the surface of the substrate by thermal evaporation and reach thermal equilibrium quickly, diffuse and then interact with.

4. Summary

Aluminum thin films deposited by thermal evaporation resulted in a high quality of crystal owing to the high purity of aluminum, and lead to defect free since it shows a high index of crystallinity. XRD spectra also confirmed no impurity occurred in all films with different substrates. Aluminum thin film on silicon n-type substrate exhibits the best quality of crystal due to the lowest FWHM of 0.2362. The surface of the aluminum films was also shows a smoother surface about less than 10 nm. Vacuum thermal deposition method has very stable deposition even though the substrate has different properties like physical, chemical or thermal.

References

- [1] K. Bordo and H. G. Rubahn, "Effect of deposition rate on structure and surface morphology of thin evaporated al films on Dielectrics and Semiconductors," *Medziagotyra*, vol. 18, no. 4, pp. 313–317, 2012.

- [2] M. G. Faraj, K. Ibrahim, M. H. Eisa, and M. A. Alrajhi, "Comparison of Aluminium Thin Film Deposited on Different Polymer Substrates With Thermal Evaporation for Solar Cell Applications," *J. Ovoic Res.*, vol. 10, no. 6, pp. 231–235, 2014.
- [3] Y.-Q. Xiong, X.-C. Li, Q. Chen, W.-W. Lei, Q. Zhao, L.-J. Sang, Z.-W. Liu, Z.-D. Wang, and L.-Z. Yang, "Characteristics and properties of metal aluminum thin films prepared by electron cyclotron resonance plasma-assisted atomic layer deposition technology," *Chinese Phys. B*, vol. 21, no. 7, p. 078105, 2012.
- [4] N. G. Semaltianos, "Thermally evaporated aluminium thin films," *Appl. Surf. Sci.*, vol. 183, pp. 223–229, 2001.
- [5] D. V Sidelev, A. V Yuryeva, V. P. Krivobokov, A. S. Shabunin, M. S. Syrtanov, and Z. Koishybayeva, "Aluminum films deposition by magnetron sputtering systems: Influence of target state and pulsing unit," *J. Phys. Conf. Ser.*, vol. 741, p. 012193, 2016.
- [6] S. Her and Y. Wang, "Temperature effect on microstructure and mechanical properties of aluminum film deposited on glass substrates," vol. 22, no. June, pp. 268–272, 2015.
- [7] K. M. Wibowo, M. Z. Sahdan, M. T. Asmah, H. Saim, F. Adriyanto, Suyitno, and S. Hadi, "Influence of Annealing Temperature on Surface Morphological and Electrical Properties of Aluminum Thin Film on Glass Substrate by Vacuum Thermal Evaporator," *IOP Conf. Ser. Mater. Sci. Eng.*, vol. 226, p. 012180, 2017.
- [8] H.-Y. Li, Y.-F. Liu, Y. Duan, Y.-Q. Yang, and Y.-N. Lu, "Method for Aluminum Oxide Thin Films Prepared through Low Temperature Atomic Layer Deposition for Encapsulating Organic Electroluminescent Devices," *Materials (Basel.)*, vol. 8, no. 2, pp. 600–610, 2015.

OPTIMIZATION OF CuO FILMS AT DIFFERENT pH VALUE FOR OXYGEN GAS DETECTION

Nur Amaliyana Raship¹, Mohd Zainizan Sahdan¹, Anis Suhaili Bakri¹, Nor Damsyik Mohd Said¹

¹Microelectronics and Nanotechnology – Shamsuddin Research Centre (Mint-SRC), Universiti Tun Hussein Onn Malaysia, 86400 Parit Raja, Batu Pahat, Johor.

Abstract: Copper oxide (CuO) film was used as a sensing layer for oxygen (O_2) sensing devices. CuO films were deposited by dip coating technique on a silicon wafer. The X-ray diffraction (XRD) result indicated that the film at pH 12.0 has good crystalline quality and match the characteristics peaks of CuO phase. The field emission scanning electron microscope (FESEM) image showed that the pH 12.0 film surface was uniform and has homogenous flower-like structure with porosity value of 19.2 %. The atomic force microscope (AFM) analysis reveals that the surface roughness of the film at pH 12.0 was 70.18 nm. The electrical measurement shows the resistivity of the film was 1.18 $\Omega \cdot cm$. Oxygen gas sensing characteristics such as sensitivity and response time were also reported.

Keywords: Copper oxide, dip coating, oxygen gas, gas sensor, room temperature

1. Introduction

O_2 is a natural component of air that contains non-toxic and non-flammable gas. O_2 also is a colourless and odourless gas. The O_2 concentration in the air of an average environment on the earth is about 20.9%. O_2 detection is required in fields such as industrial process, food processing plants, pollution control through automobile engine, medical facilities and room oxygen monitor [1][2]. Furthermore, O_2 gives potential risks to human health at low oxygen concentrations [3]. Thus, a highly sensitive and fast response of O_2 gas sensor is important and necessary to maintain human life. Currently, there are many types of sensors that can be used to detect varies type of gases [4]. One of the most usual types of sensor is chemiresistive sensor which related to the electrical resistance changes when the adsorption of O_2 on the surface of the film [5][6].

Various chemiresistive sensor has been developed using metal oxide semiconductor. One of them is a p-type semiconductor which is CuO. CuO exhibits a stable narrow band gap in the range between 1.2 eV to 1.9 eV [7][8]. CuO structures such as nanowires, nanorods, nanosheets and nanoparticles have been produced and investigated on their gas sensing properties [6]. Previously, spin coating [9], electrodeposition [10], RF sputtering [11], hydrothermal [12] and spray pyrolysis [13] have been used to prepare and control the morphology of the CuO structures for gas sensor application. However, there are no reports on p-type CuO for O_2 detection using dip coating technique. Thus, the suitability of CuO as a sensing material for O_2 sensor and their gas sensing properties is one of the ongoing research problems.

In this present work, the optimum CuO film was varied at different pH value for O_2 gas detection prepared by a low-cost fabrication method, dip coating technique. The characterization of CuO film were investigated using XRD, FESEM, AFM and four-point probe. The gas sensing characteristics such as sensitivity, response time and recovery time were also determined.

2. Materials and method

2.1 Preparation of CuO solution

In this present study, the solution was prepared by dissolving copper (II) sulfate pentahydrate ($CuSO_4 \cdot 5H_2O$) in distilled water. Then, 3M of lactic acid was added to the solution and keep stirring for 30 minutes until it was completely dissolved. Next, sodium hydroxide (NaOH) was added to the solution until the pH of the solution reaches pH 12.0, pH 12.3 and pH 12.5. The pH value of the solution was measured using pH meter. The solution was then dissolved and keep stirred on a hot plate magnetic stirrer until the temperature of the solution drops to 24 °C. The colour of CuO solution obtained from this process was a dark blue and clear without any precipitates. Finally, the solution undergo aging process for 24 hours at room temperature.

2.2 Fabrication of CuO film

CuO films were prepared on the silicon wafer by dip coating technique using dip coating machine (PTL-MM01 Desktop Dip Coater). Before starting the deposition process, the silicon substrate was cleaned with acetone and ethanol for 10 minutes each by using the ultrasonic cleaning machine to remove the impurities on

the substrate surface. To remove the native oxide, the silicon substrate was immersed in diluted hydrofluoric acid (HF) for 2 minutes with a ratio of 1 : 10. The silicon substrate was then rinsed with distilled water and dried with nitrogen gas (N_2). For the deposition process, the silicon substrate was dipped for 5 minutes and withdrawn from the solution at a withdrawal speed of 70 mm/min. The film was then pre-heated for 5 minutes at 150 °C on a hot plate to evaporate the solvent. The dipping and pre-heated process were repeated for four times onto the same substrate. Lastly, the film was annealed at 400 °C in an electrical furnace to improve the crystallinity of the film. The process for the fabrication of CuO film is shown in Fig. 1.

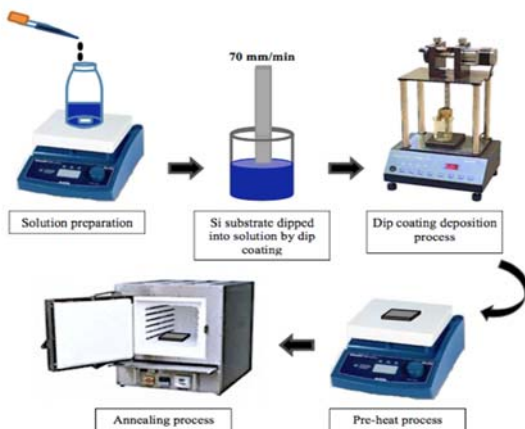


Fig. 1 Fabrication process of CuO film.

2.3 Characterization of CuO film

The structural properties of the CuO films were characterized by XRD using PANalytical X-Pert³ Powder with Cu K α radiation of wavelength $\lambda = 0.1540$ nm and operating at 40 mA of current and 40 kV of voltage. Measurements were set in the range of $2\theta = 20^\circ - 80^\circ$ with a step size of 0.02°. The surface morphology and the porosity CuO film was examined using FESEM (FESEM, model: JSM-7600F) with an accelerating voltage of 15 kV. The porosity value was measured using ImageJ software. Surface roughness of CuO film on silicon substrates was characterized by an AFM (Park Systems, XE-100) with a non-contact mode using PPP-NCHR cantilever. Measurement was done at the scan size of 40 $\mu\text{m} \times 40 \mu\text{m}$. The electrical resistivity of CuO film was determined by a four-point probe instrument using a Lucas-Signatton Pro4 connected with a Keithley 2400 series source meter.

2.4 Gas sensor fabrication

In order to fabricate the gas sensor, a thin layer of gold (Au) was coated on the top surface of CuO film by a thermal evaporator machine (Vacuum pump unit VPC-061 Ulvac Kiko). The Au electrodes layer was coated through an aluminium mask. The Au electrodes were

deposited in a vacuum chamber with pressure approximately $\sim 10^{-3}$. The current was applied up to 40 mA to start the evaporation process. The deposition time was set for 30 minutes.

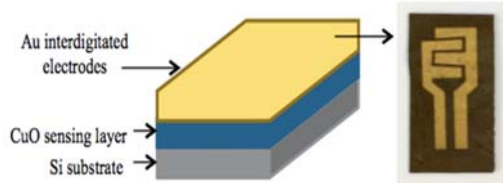


Fig. 2 CuO film as a sensing layer.

2.5 Gas sensor measurement

The gas sensing measurement was evaluated by measuring the change of the film resistance in the presence of oxygen gas. A schematic diagram of the experimental setup for gas sensing measurement was shown in Fig. 3. The fabricated CuO sensor was placed in a customized gas sensing chamber with the capacity volume of $2.01 \times 10^{-3} \text{ m}^3$. Digital multimeter was then connected to CuO sensor films. Then, the resistance in ambient air was taken as the reference response.

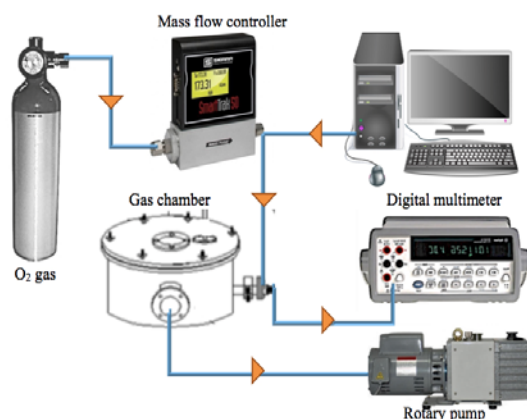


Fig. 3 Experimental setup for gas testing.

Initially, the argon gas was exposed into the chamber to remove any contaminations inside the chamber. Next, the O₂ gas was flow into the chamber with flow rate of 100 sccm. The flow rate of the gas was controlled using mass flow controller (Siera Instrument, Smart Track 50 Series). The exposure of oxygen gas was fixed for 5 minutes each cycle. The O₂ gas is then clear off from the chamber for each cycle by vacuum the chamber using a rotary pump, allowing the CuO sensor to recover. The measurement data were collected using a high precision digital multimeter (Fluke 8846 A) and analyzed using Matlab (R2012a).

3. Results and Discussion

Fig. 4 presents the X-ray diffraction pattern of CuO films at different pH value prepared using dip coating technique. It was observed that all the deposited film was

polycrystalline nature with a monoclinic structure. The dominant peaks were observed at 35.5° and 38.7° corresponding to the reflections from (002) and (111) planes of CuO phase. Another peak were observed at $2\theta = 33.8^\circ$, 48.7° and 57.8° which indexed to (110), (-202) and (202) planes of CuO, respectively. These indicate that all the peaks are matched with the characteristics peaks of CuO phase (ICSD 98-008-7124).

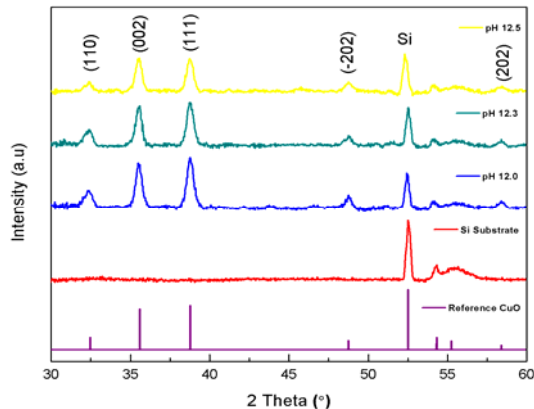


Fig. 4 XRD patterns of CuO films at different pH value.

Based on Table 1, the full width at half maximum value (FWHM) increases with increase in pH value. This result indicates that film at pH 12.0 have high crystal quality as it has lowest FWHM due to their sharp and narrow peak.

Table 1 Structural properties of CuO films at different pH value.

pH value	Pos. [$^{\circ}$ 2Th]	FWHM ($^{\circ}$)	Crystallite size (nm)
12.0	35.5809	0.1181	94.48
12.3	35.5322	0.1476	70.58
12.5	35.5411	0.2952	32.62

Fig. 5 shows the FESEM images of CuO films at different pH value. It shows that the surface morphology of CuO film was uniform with growth of flower-like structure. At pH 12.0, the petals are connected to each other through the narrow base, rooted in one centre and form the flower-like structure. As the pH value increases to 12.3 and 12.5, the flower-like structure starts detached and formed petal-like structures. Previous researchers reported that hierarchical flower-like structure could enhance the performance of the gas sensor due to their high surface to volume ratio which provides a large surface area [14][15].

All of the films also exhibits a porous structure with the porosity value of 19.2 %, 7.944 % and 3.775 % for pH 12.0, pH 12.3 and pH 12.5, respectively. Previous researchers stated that film with porous structure gives high sensitivity and fast response due to the gas can easily penetrate into the sensing film [16][17].

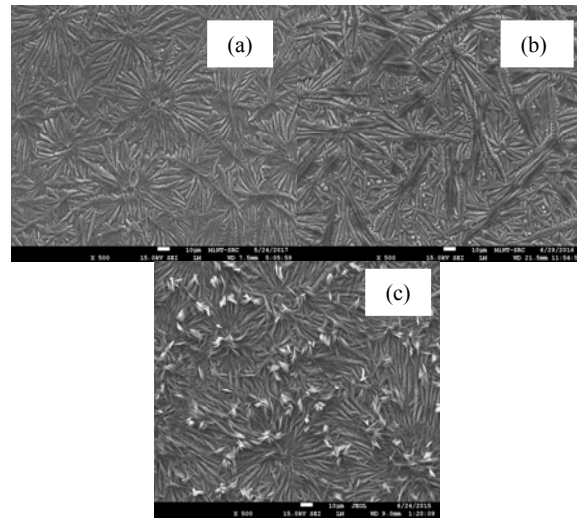


Fig. 5 FESEM images of CuO films at (a) pH 12.0 (b) pH 12.3 (c) pH 12.5.

The surface topography and surface roughness of CuO film were measured by AFM. Fig. 6 indicates the 3D AFM images of CuO films at different pH value. It was observed that the film surface at pH 12.0 exhibits hills and valley-like structure, which are uniformly distributed over the entire substrate surface. It also can be seen the film surface is well organized with mostly same size. The images also show a presence of pores in the film surface which is good for the performance of the gas sensor. This result agrees well with FESEM images in Fig. 5. Based on AFM measurement, the surface roughness of CuO films at pH 12.0, pH 12.3 and pH 12.5 was 70.18 nm, 284.0 nm and 387.0 nm, respectively.

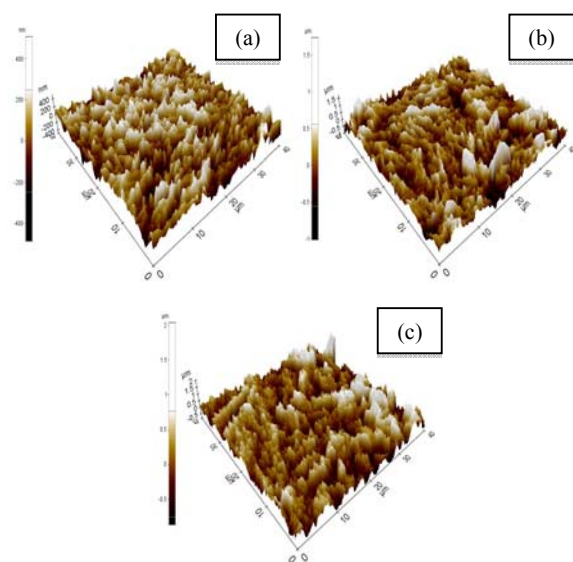


Fig. 6 3D AFM images of CuO films at (a) pH 12.0 (b) pH 12.3 (c) pH 12.5.

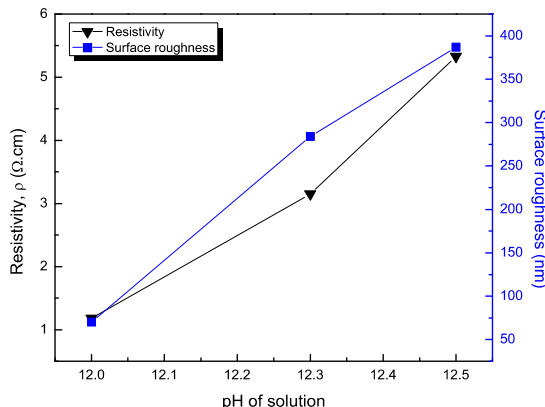


Fig. 7 Relationship of electrical resistivity and surface roughness of CuO films at different pH value.

For the electrical measurements, it was observed that the resistivity is directly proportional to the pH value as shown in Fig. 7. The increase in resistivity of the films may be due to increase in surface roughness. Previous researcher reported that the rough surface of the film is expected to cause diffusive of electrons contributes to increasing in resistivity [18]. Other than that, the resistivity in this present study is quite close to the experimental results by Li et al. [19].

Based on the effects of pH value, CuO film at pH 12.0 was chosen as the optimum film which is expected good for gas sensing performance. This is due to CuO film at pH 12.0 have good crystalline quality with the highest intensity peak compared to others. The surface morphology was uniform flower-like structure with higher porosity value. Other than that, the film has the lowest surface roughness and lowest resistivity which is benefit for gas sensing application.

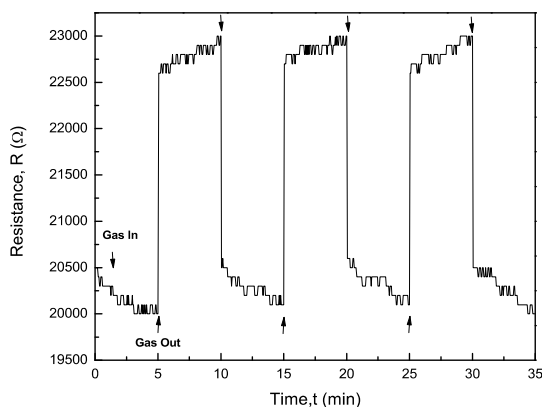


Fig. 8 The gas sensing performance of CuO film.

Fig. 8 shows the gas sensing performance of optimum CuO film which is pH 12.0 for O₂ gas detection. For a p-type gas sensor, oxidizing gases will induce an accumulation of holes near the surface, thus resulting in a decrease in resistance when it is exposed to the target gas [20][21]. In this study, the CuO gas sensor was tested at

room temperature, thus O₂⁻ is known to be a dominant charge oxygen species. When CuO film was exposed to the oxygen gas, molecules of oxidizing are adsorbed onto a CuO film surface and chemisorption proceeds by the electron transfer from the CuO film surface to the oxygen gas molecules. The transfer of an electron from CuO to the oxygen gas resulting in the lowering of the Fermi level. Thus, in turns leading to an increased accumulation of hole near to the surface and decrease the resistance of the CuO film. So, it can be concluded that the obtained result of interaction between the surface of the CuO based sensor and O₂ gas is same as the theory of p-type oxidizing gas sensor behaviour.

The sensor response is the change of resistance measured during gas exposure. In this study, the gas response of the sensor is defined as the ratio between the change of resistance when exposed to O₂ gas with the resistance in air. The reaction is given by

$$S = \frac{R_a - R_g}{R_g} \times 100\% \quad (1)$$

where R_a = The resistance in the ambient air

R_g = The resistance of the sensor when it exposed to target gas

Based on the calculation of the reaction from equation 1, the sensor response of CuO film when exposed to the O₂ gas was 26.7 %. For the response time, the time taken by the CuO sensor to reach 90 % of its final value was found to be 2.381 s. While the recovery time for the sensor to return to the 90% of the initial value was 7.128 s.

4. Summary

An optimum of CuO film at pH 12.0 was successfully tested for oxygen gas sensing. This film was deposited by dip coating technique on silicon substrate. The XRD results reveal that the dominant peaks were obtained at 35.5 and 38.7 with high crystalline quality of CuO phase. The FESEM images show that there is growth of hierarchical flower-like structure with the porosity value of 19.2 %. The surface roughness of the film was 70.18 nm while the electrical resistivity was 1.18 $\Omega \cdot \text{cm}$. The gas sensing performance of CuO film for O₂ gas at room temperature were 26.7 %, 2.381 s and 7.128 s for its sensitivity, response time and recovery time, respectively. Thus, this study on the effect of pH value might be significant in producing baseline data that can be used for further research on CuO film gas sensor.

5. Acknowledgement

The authors would like to thank the Microelectronic and Nanotechnology-Shamsuddin Research Centre (MiNT-SRC), UTHM for providing the experimental facilities for this research work. This study is financially supported by Ministry of Higher Education Malaysia

(MyBrain15), Universiti Tun Hussein Onn Malaysia for providing GIPS Vot. U325, Grant Contract Vot. A043 and Grant Contract Vot. A124.

References

- [1] Silver, A.T., and Juárez, A.S. SnO₂:Ga thin films as oxygen gas sensor. *Mater. Sci. Eng. B Solid-State Mater. Adv. Technol.*, Volume 110, (2004), pp. 268–271.
- [2] Sharma, R.K., Bhatnagar, M., and Sharma, G. Mechanism of highly sensitive and fast response Cr doped TiO₂ oxygen gas sensor. *Sensors Actuators B Chem.*, Volume 45, (1997), pp. 209–215.
- [3] NorthWest Occupational Health & Safety. *Oxygen Effects and Regulatory Limits*. Canada. 2009.
- [4] Jain, G.H. MOS gas sensors : What determines our choice ?. *IEEE*, (2011), pp. 66–72.
- [5] Barsan, N., Koziej, D., and Weimar, U. Metal oxide-based gas sensor research: How to?. *Sensors Actuators, B Chem.*, Volume 121, (2007), pp. 18–35.
- [6] Zhang, Q., Zhang, K., Xu, D., Yang, G., and Huang, H. CuO nanostructures : Synthesis, characterization, growth mechanisms, fundamental properties, and applications. *Prog. Mater. Sci.*, Volume 60, (2014), pp. 208–337.
- [7] Li, Y., Liang, J., Tao, Z., and Chen, J. CuO particles and plates: Synthesis and gas-sensor application. *Mater. Res. Bull.*, Volume 43, (2008), pp. 2380–2385.
- [8] Kumar, V., Panah, S.M., Tan, C.C., Wong, T.K.S., Chi, D.Z., and Dalapati, G.K. Copper oxide based low cost thin film solar cells. *IEEE*, (2013), pp. 443–445.
- [9] Nurfazliana, M.F., Kamaruddin, S.A., Nafarizal, N., Saim, H., and Sahdan, M.Z. Effects of annealing process on the structural, optical and electrical properties of copper oxide thin films grown by immersion technique, *Advanced Materials Research*, Volume 1133, (2016), pp. 439–443.
- [10] Rahman, A.S.M.S., Islam, M.A., and Shorowordi, K.M. Electrodeposition and characterization of ZnO thin films for solar cell applications. *Int. J. Adv. Eng. Nanotechnol.*, Volume 2, (2011), pp. 18–24.
- [11] Akgul, U., Yildiz, K., and Atici, Y. Effect of annealing temperature on morphological, structural and optical properties of nanostructured CuO thin film. *Eur. Phys. J. Plus*, Volume 131, (2016), pp. 1-6.
- [12] Shresta, K.M. Modifying nanoparticle shape by choice of synthetic method: Nanorods, spheres, mutipods and gels. Thesis Ph.D. Kansas State University; 2012.
- [13] Roy, S.S., Bhuiyan, A.H., and Podder, J. Optical and electrical properties of copper oxide thin films synthesized by spray pyrolysis technique. *Sensors & Tranducers*, Volume 191, (2015), pp. 21–27.
- [14] Yang, C., Xiao, F., Wang, J., and Su, X. 3D flower- and 2D sheet-like CuO nanostructures: Microwave-assisted synthesis and application in gas sensors. *Sensors Actuators B. Chem.*, Volume 207, (2015), pp. 177–185.
- [15] J. H. Lee, “Gas sensors using hierarchical and hollow oxide nanostructures: Overview,” *Sensors Actuators, B Chem.*, vol. 140, no. 1, pp. 319–336, 2009.
- [16] Ayesh, A.I. Metal/metal-oxide nanoclusters for gas sensor applications. *J. Nanomater.*, Volume 2016, (2016), pp. 1-17.
- [17] Tiemann, M. Porous metal oxides as gas sensors. *Chem. - A Eur. J.*, Volume 13, (2007), pp. 8376–8388.
- [18] Tang, W., Chao, Y., Weng, X., Deng, L., and Xu, K. Optical property and the relationship between resistivity and surface roughness of indium tin oxide thin films. *Phys. Procedia*, Volume 32, (2012), pp. 680–686.
- [19] Li, F.M., Waddingham, R., Milne, W.I., Flewitt, A.J., Speakman, S., Dutson, J., Wakeham, S., and Thawaiites, M. Low temperature (< 100 °C) deposited P-type cuprous oxide thin films: Importance of controlled oxygen and deposition energy. *Thin Solid Films*, Volume 520, (2011), pp. 1278–1284.
- [20] Shankar, P., Bosco, J., and Rayappan, B. Gas sensing mechanism of metal oxides : The role of ambient atmosphere, type of semiconductor and gases - A review. *Sci. Jet*, Volume 4, (2015), pp. 126.
- [21] Fine, G.F., Cavanagh, L.M., Afonja, A., and Binions, R. Metal oxide semiconductor gas sensors in environmental monitoring. *Sensors*, Volume 10, (2010), pp. 5469–5502.

INVESTIGATION ON THE AGING EFFECT OF ALUMINIUM THIN FILM TREATED BY ATMOSPHERIC PRESSURE PLASMA NEEDLE JET

Rizon Rizan Elfa¹, Nayan Nafarizal², Mohd Khairul Ahmad¹, Kusnanto Mukti Wibowo¹, Chin Fhong Soon¹, Mohd Zainizan Sahdan³, Mohamad Hafiz Mamat⁴, Ali Aldalbah⁵

¹Faculty of Electrical and Electronic Engineering, Universiti Tun Hussein Onn Malaysia (UTHM), 86400 Parit Raja, Batu Pahat, Johor Malaysia.

²Microelectronics and Nanotechnology- Shamsuddin Research Centre (MiNT-SRC), Institute of Integrated Engineering, Universiti Tun Hussein Onn Malaysia (UTHM), 86400 Parit Raja, Batu Pahat, Johor, Malaysia.

³Preston GeoCEM Sdn Bhd, No 33A, Jalan Universiti 4, Taman Universiti, 86400 Parit Raja, Johor, Malaysia.

⁴NANO-Electronic Centre, Faculty of Electrical Engineering, Universiti Teknologi MARA, Shah Alam, 40450 Selangor Malaysia.

⁵Chemistry Department, King Saud University, Riyadh 11451, Saudi Arabia.

Abstract: The atmospheric pressure plasma jet give a hunch to be expanding in pre-treatment application especially in upgrade conventional vacuum plasma cleaning in semiconductor industry. Plasma pre-treatment in semiconductor industry is a crucial issue as the process takes up 34 % of the total process of semiconductor device. The pre-treatment of plasma is needed to reduce or eliminate adventitious surface contamination on the thin film. In this paper shows that the atmospheric pressure plasma jet treatment is highly effective in activating the surface of Al thin film. Surface activation improves the adhesion of thin films and the effect of the treatment to have superhydrophilic thin film and last up to three hours. The thin films have been surface treated using the Ar atmospheric-pressure plasma, resulting in enhanced surface energy as proved by Water Contact Angle (WCA) measurements. The image of Al thin film surface topography shows that the treated surface roughness is reduced however the grain size of the particles is stable. The XRD pattern of treated Al thin film also remained stable as before of the atmospheric pressure plasma jet treatment. This gives evidence that the atmospheric pressure plasma jet introduce activation layer on the thin film surface without give impact to the thin film crystallity.

Keywords: Atmospheric pressure plasma jet, surface wettability, thin film cleaning, AFM, XRD

1. Introduction

During the few past decades, the development of artificial plasma has been focused in low-pressure plasma due to the long mean free path of the plasma in the vacuum environment [1]. This low-temperature plasma provides high performance in pre-treatment cleaning and deposition. The implementation of plasma technology has been fully utilized from small scale for example in a research lab to large scale such as in electronic and semiconductor fabrication industry. However, due to its requirement operating in low-pressure introduces several issues, for instance, high-cost machine, long period of process include time for provide vacuum environment and unable to provide continuous process due to sample need to be taken-in and taken-out. Besides, it becomes a trivial issue as in the semiconductor process, the plasma pre-treatment cleaning takes up about 34 % or 500 repeated pre-treatment process of the overall process for single chip.

In order to create the plasma in atmospheric pressure surrounding is a challenge due to the short mean free path of the plasma will eventually easy to increase the gas temperature into a high level (~10000 K) [2]. At a very high temperature plasma is applied to melt the metal such as in welding. Such a very high temperature turns to limit its application. In other hand, a few years back a low temperature in the ambient surrounding is created and called atmospheric pressure plasma jet (APPJ).

Currently, the application of APPJ is needed in engineering and biomedical fields such as treated polymers, stainless steel for painting and biomimetic materials [3][4][5][6][7]. However, there is still out numbers of a treated thin film for nanostructure fabrication and application. Due to superhydrophilic property in terms of low adhesion and high surface energy, it opens up a new possibility to provide a better growth rate of the substrate in the deposition process. The cleaning process is required due to substrates high decontamination and low adhesion to ensure the sample give out optimum result in paint and fabrication

application [8]. Hence, in this paper will reveal the intensive application of APPJ in treat aluminum (Al) thin film that will act as pre-treatment in the semiconductor industry.

2. Experimental Procedure

In the study, the 10 mm square Al thin film was exposed to 60 seconds and 5 seconds plasma treatment to verify the surface wettability of the treated surface after several hours. The aging effect of the plasma towards Al thin film is recorded by using VCA Optima, USA. The wettability testing was done by using sessile drop technique, whereby in this study 100 μL droplet of distilled water (DI water) was ejected and dropped onto treated sample. The adjacent angle between the treated surface and the water droplet was taken as the surface wettability test. The surface that exhibit above 90° was characterized as hydrophobic surface meanwhile; below 90° have hydrophilic surface characteristic. The samples were verified from exactly after plasma treatment until 4000 seconds (four days).

The thin film surface structure and roughness by using the AFM measurement (AFM 5010, Hitachi). The same thin film was used for surface topography characterization before plasma treatment and after plasma treatment. The topography of the thin film was only obtained for 60 seconds plasma treatment because there is no significant change in surface characterization until 60 seconds treatment time.

The x-ray diffraction (XRD) pattern of Al thin film was obtained for samples before plasma treatment and after 60 seconds of plasma treatment.

2.1 Aluminium Thin Film Deposition

The 8 inch Si wafer is cut in 1 cm^2 square as substrate for thin film deposition. Prior deposition, the substrates were cleaned. For cleaning purpose the buffer oxide etching solution was used to remove native oxide before deposition takes place. The Al thin film is deposited by utilized thermal evaporator (Ulvac Kiko, Inc). In this paper, the Al thin film is deposited by using 30 mg industrial grade Al (99.97%). The thickness of deposit Al thin films were about 40 μm .

2.2 Atmospheric Pressure Plasma Treatment Procedure

As mentioned earlier, the plasma discharge in the atmospheric environment was powered by alternating current 240 V and connected to the neon transformer to boosts up the voltage to 8 kV as shown in Fig. 1(a). The working frequency was also increased from 50 Hz to 35 kHz. One of the high voltage supply was connected to outer electrode wrapped Cu (copper) tape at quartz tube and the other one electrode Cu wire was inserted into the quartz tube. The high and width of the Cu tape is 15 mm and 10 mm respectively. The quartz tube was 150 mm long and 5 mm diameter. The plasma discharge

penetrates about 15 mm from the quartz tube by feeding 40 L/min Ar as working gas. The plasma jet was placed horizontally to the earth and perpendicular to the sample during treatment process as shown in Fig. 1(b).

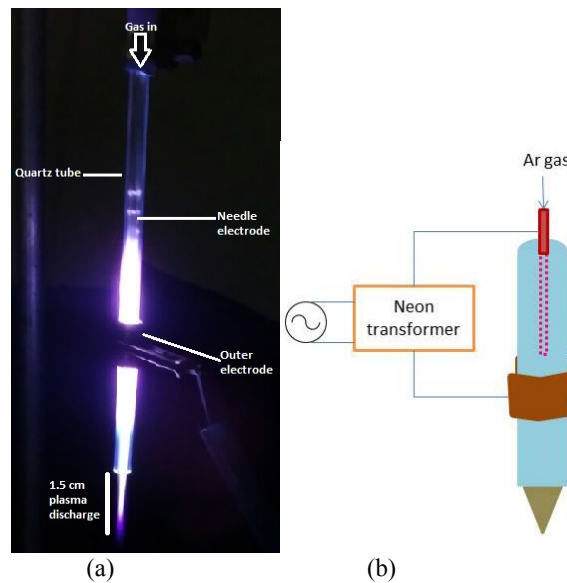


Fig. 1 (a) The image of atmospheric pressure plasma needle jet. (b) The configuration of atmospheric pressure plasma needle jet connected to the high neon transformer and 40 L/min feed Ar working gas.

3. Results and Discussion

The wettability testing is done only for 5 seconds and 60 seconds sample of Al thin film. This is due to have the intensive understanding of APPNJ's effect on the sample upon storage in the dry cabinet after treatment. The initial reading of the Al thin film without treat with APPNJ is 72°. The wettability testing is done by several recorded times such as right after APPNJ treatment that is less than 5 minutes, 30 minutes, 1 hours, 1 hours and a half minutes, 3 hours, 6 hours, 12 hours, 24 hours, 48 hours, 72 hours and 96 hours as shown in Fig. 2

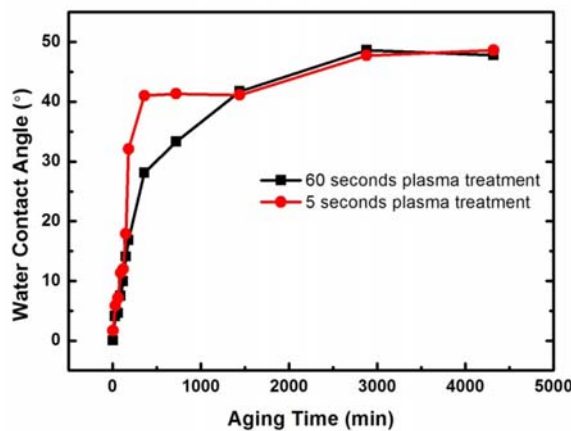
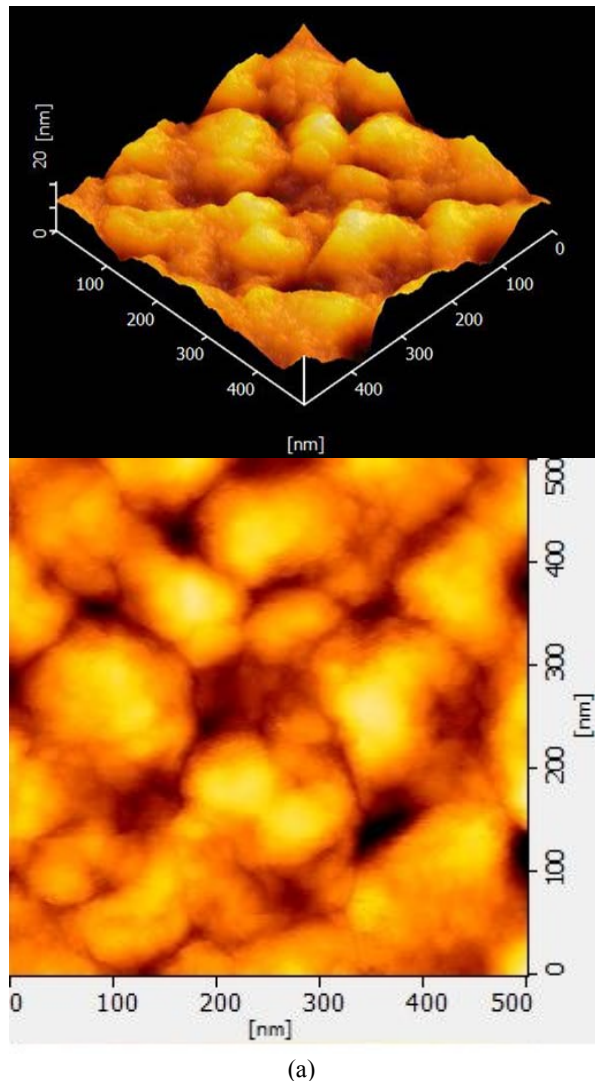
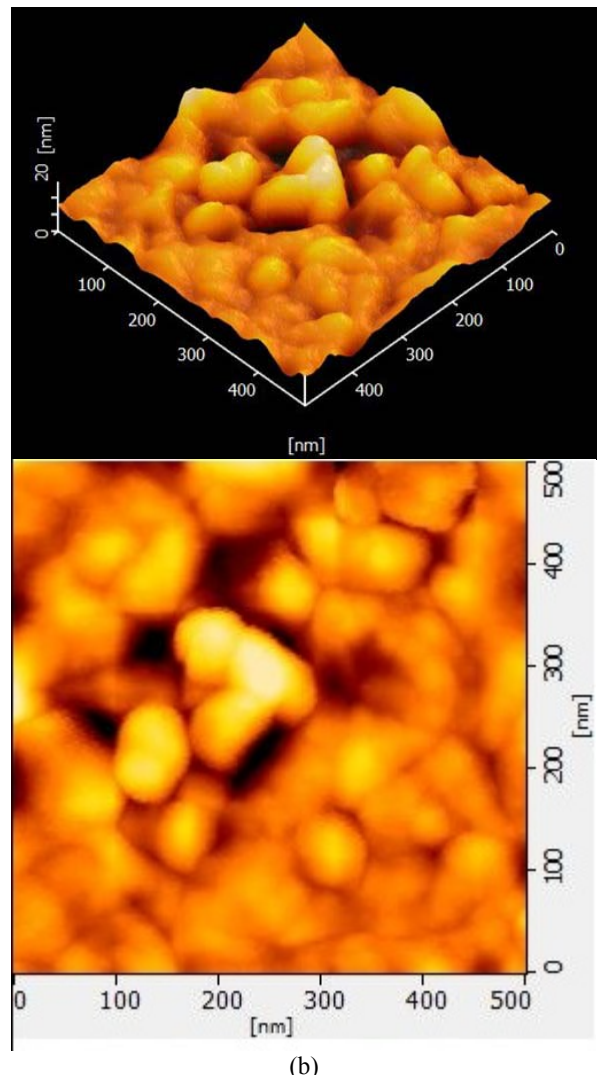


Fig. 2 The aging effect of the Al thin film after APPNJ treatment for 5 and 60 seconds recorded from immediately after the treatment until four days.

Figure 3(a) shows the initial image of thin film surface roughness is $R_a 5.37 \times 10^{-3}$ nm. Meanwhile, the surface roughness of the sample after plasma treatment as shown in Fig. 3(b) is reduced to $R_a 2.51 \times 10^{-3}$ nm for 60 seconds of plasma treatment. In the two-dimensional image of the Al thin film shows that the bump-like features after plasma treatment seem to get more flat than before the treatment. This could be the reason behind the surface roughness after the plasma is reduced in 2.86 nm. However, the grain size of particle shows no significant change as the grain size of particles before the plasma treatment is 3.81 nm^2 and after plasma treatment is 3.82 nm^2 .



(a)



(b)

Fig. 3 Three-dimentional and two-dimentional images of Al thin film surface roughness before APPNJ treatment (a) and after APPNJ treatment (b).

The x-ray diffraction (XRD) pattern of the Al thin film is obtained for samples before plasma treatment and after several seconds of plasma treatment. At first, the duration of plasma treatment is done in 60 seconds and for further investigation the duration of plasma treatment keeps on longer until 120 seconds in order to attain a probability of plasma effect at a much higher level of treatment time of plasma. The sample is analyzed by XRD before plasma treatment and after 60 seconds plasma treatment is shown in Fig. 4.

The data clearly shows that Al deposited is crystalline and intense (111) diffraction peak and followed others characteristic line at (200), (220) and (311) [9]. The silicon as the substrate is crystalline and exhibit the intense peak at 51.09° along with another broad peak at 56.26° . Then the same sample is utilized for 60 seconds plasma treatment. However, there is no significant changing of the thin film crystalline structure.

Hence, it can be claimed that the surface modification introduces by APPNJ is only affected at the surface interface only in the range less than a few nanometer as if the APPNJ plasma is kept for longer until 120 seconds there is also no observed changing of the thin film crystalline data as proved in Fig. 5.

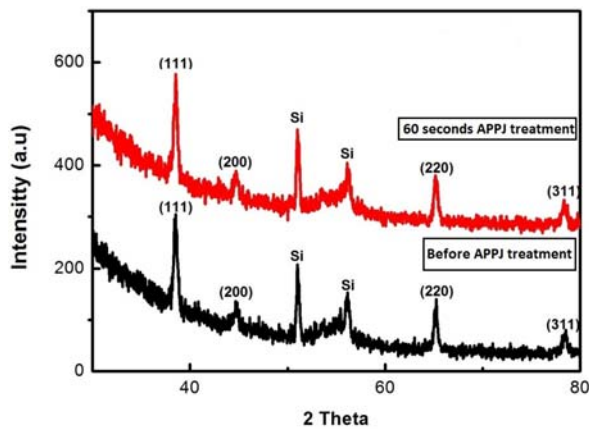


Fig. 4 The XRD pattern of the Al thin film before and after 60 seconds APPNJ treatment

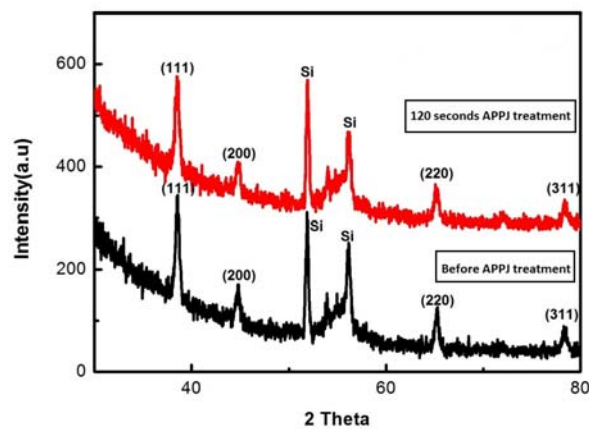


Fig. 5 The XRD pattern of AL thin film before and after 120 seconds APPNJ treatment

4. Summary

The wettability of the Al thin film shows a great enhance prior to atmospheric pressure plasma treatment. The high surface wettability also indicates the sample surface adhesion is decreasing. The treated sample properties retain its superhydrophilic characteristic up to three hours after plasma treatment. Besides, from the surface topography result, the roughness of the thin film is reduced to $R_a 2.51 \times 10^{-3}$ nm from $R_a 5.37 \times 10^{-3}$ nm for 60 seconds of plasma treatment. The XRD pattern of the Al thin film shows that the treatment of thin film is only affected on the surface only and not affected the bulk property of the Al thin film.

5. Acknowledgement

The facilities used in this study are supported by MiNT-SRC, Universiti Tun Hussein Onn Malaysia and this work is partially supported by Incentive Grant Scheme for Publication (IGSP U675) and Contract Grant Scheme (CGS U566) of Universiti Tun Hussein Onn Malaysia, Ministry of Higher Education Malaysia. Ali Aldalbahi acknowledges the financial support by Deanship of Scientific Research, College of Science Research Center, King Saud University.

References

- [1] P. C. Kong and E. Pfender, Plasma processes, (1997) pp. 14–15, 1997.
- [2] Z. Rahman, H. Rahman, and A. Rahman, Classification and Generation of Atmospheric Pressure Plasma and Its Principle Applications, *Int. J. Math. Phys. Sci. Res.*, Volume 2, no. 2, (2015) pp. 127–146.
- [3] G. C. C. Mendes, T. R. S. Brandão, and C. L. M. Silva, Ethylene oxide sterilization of medical devices: A review, *Am. J. Infect. Control*, Volume 35, no. 9, (2007) pp. 574–581.
- [4] P. Andrik and S. Velgos, Sterilization and disinfection in dentistry., *Lek. Obz.*, Volume 2, no. 4,(1953) pp. 262–264.
- [5] C. Service, “Glutaraldehyde and Formaldehyde : Allergic Contact Dermatitis (12 / 03),” 2003.
- [6] M. Moisan, J. Barbeau, S. Moreau, J. Pelletier, M. Tabrizian, and L. Yahia, Low-temperature sterilization using gas plasmas: a review of the experiment and an analysis of the inactivation mechanisms, *Int. J. Pharm.*, vol. 226, (2001)pp. 1–21.
- [7] P. Koulik, S. Begounov, and S. Goloviatinskii, Atmospheric Plasma Sterilization and Deodorization of Dielectric Surfaces, *Plasma Chem. Plasma Process.*, vol. 19, no. 2, (1999) pp. 311–326.
- [8] M. Noeske, J. Degenhardt, S. Strudthoff, and U. Lommatsch, Plasma jet treatment of five polymers at atmospheric pressure: Surface modifications and the relevance for adhesion, *Int. J. Adhes. Adhes.*, Volume 24, no. 2, (2004) pp. 171–177.
- [9] X.-F. Lei and J.-X. Ma, Synthesis and electrochemical performance of aluminum based composites, *J. Brazilian Chem. Soc.*, Volume 21, no. 2, (2010) pp. 209–213.

FORMATION OF MONOLAYER POLYSTYRENE ARRAY TEMPLATE FOR GOLD NANOMESH STRUCTURE

Nur Liyana Razali^{1,2}, Marlia Morsin^{1,2}, Muhamad Mat Salleh³, Nurfarina Zainal^{1,2}, Marriatyi Morsin³

¹Institute of Microelectronics & Nanotechnology - Shamsuddin Research Centre (MiNT-SRC), Universiti Tun Hussien Onn Malaysia, 86400, Parit Raja, Batu Pahat, Johor, Malaysia.

²Faculty of Electrical and Electronic Engineering, Universiti Tun Hussien Onn Malaysia, 86400, Parit Raja, Batu Pahat, Johor, Malaysia

³Institute of Microengineering and Nanoelectronics (IMEN), Universiti Kebangsaan Malaysia, 43600 UKM Bangi, Selangor, Malaysia

⁴Politeknik Sultan Salahuddin Abdul Aziz Shah, Persiaran Usahawan, Seksyen U1, 40150 Shah Alam, Selangor.

Abstract: In this study, the preparation of monolayer array template was performed using 0.2 μm polystyrene (PS) nanospheres monodisperse micro particle deposited onto Indium Tin Oxide (ITO) coated glass substrate. The template was used to arrange the gold (Au) in nanomesh structure thus, enhance its homogeneity for having better sensitivity and repeatability in the plasmonic sensor application. PS nanosphere template was prepared by diluting 0.2 μm PS liquid with ethanol in the ratio of 1:3 and stirred with 400 rpm for 1 hours at 40 °C. Next, the PS solution was spin coated on ITO substrate at different speed variation starting from 200 rpm to 800 rpm in 3 minutes at room temperature. The template structure was then inspected with Field Emission-Scanning Electron Microscopy (FESEM). It was found that, the PS nanosphere template with 600 rpm speed shows the most orderly arrangement of PS array. Subsequently, the PS array template was used as a mask to deposit gold (Au) and performed via direct current (DC) sputtering method. Finally, the Au nanomesh structure was obtained using the lift – off process of PS nanosphere template.

Keywords:

Localized Surface Plasmon Resonance, Array template, Polystyrene (PS) Nanosphere, Gold Nanoparticles,

1. Introduction

There are various type of metal nanoparticles (NPs), such as gold (Au), silver (Ag) and copper (Cu) which had demonstrated exceptional radiative, nonradiative and optical properties, reasonable for an extensive variety of utilization including disease detection , diagnosis and therapy, drug delivery, biomedical imaging, biosensing [1-2] and many more. These metal NPs are popular and widely used because of their chemical properties, surface plasmon behavior and nanometer (nm) in size. Apparently, gold nanoparticles is the most commonly used due to its simple and easy preparation and synthesizing method.

Localized surface plasmon resonance (LSPR) is a resonance phenomenon of free electron waves in a metal nanostructure [3]. Gold nanostructure is one of the metal nanostructures that have gained much attention in the field of electronics, non – linear optic applications. Thus far, many researches of gold nanostructures have been done in form of synthesis and its functionality [4-6]. However, assembly or alignment of gold nanostructures and inter – particle separation are still requires further

investigations. The need of gold particles arrangement is a crucial element in order to enhance its sensitivity and repeatability. In the case of optical sensor applications, aggregation of gold nanoparticles can affected particles alignment hence produce insensitive optical device with poor sense performance. To date, many methods were used to compose particle arrangement such as lithography (printed pattern) [7], implementing various surfactant [8] and also block of co – polymers [9]. Yet, several of these methods are complex and require a special intensive care and costly.

In this study, assembly or alignment of gold nanostructures and inter – particle separation was performed using a lift – off technique. This technique was chosen due to simpler method and inexpensive as compared to other methods mention above. Monolayer array template was produced using polystyrene (PS) nanospheres monodisperse micro particle which deposited onto ITO coated glass substrate. The template was used to arrange the gold (Au) in nanomesh structure with the purpose to enhance its homogeneity for LSPR sensor application or also known as plasmonic sensor.

2. Experimental work

The gold (Au) nanomesh structure was fabricated using three main procedures such as preparation of polystyrene (PS) template, sputtering of gold on the ITO coated glass substrate and removal of polystyrene template from the ITO coated glass substrate. These processes are called as lift – off technique and employed the usage of deionized (DI) water with resistivity 18.2 MΩcm.

First, the polystyrene (PS) template was prepared by diluting 0.2 µm PS particle liquid with ethanol in a ratio of 1:3. The PS mixture solution was then stirred for 1 hour at 40 °C with 400 rpm and spin coated onto the substrate. The 0.2 µm polystyrene monodisperse micro particle was purchased from Sigma Aldrich. The speed of stirring times were varied in the range of 200 until 800 rpm for 3 minutes.

Next, gold is transferred onto the template using direct current (DC) sputtering system at room temperature for 4 minutes. In this research, PolaronHigh Resolution sputter coater was used with gold (Au) solid source. The gold sputtering deposition process was performed in rotation a form with setting parameter of 2.5 kV voltage and 25 mA current. The gold solid source was purchased from Hi - Tech Instruments. Finally, the polystyrene (PS) nanosphere template was removed from the substrate using acetone. The template removal procedure was through in three different phases for example 15, 30 and 60 seconds under sonication processes. Following of nanosphere PS template removal, surface morphology of the gold nanomesh structures were inspected and observed using FESEM Zeiss Supra 55VP. Figure 1 show the schematic diagram of lift-off processes that used to fabricate the gold nanomesh structure using polystyrene nanosphere template.

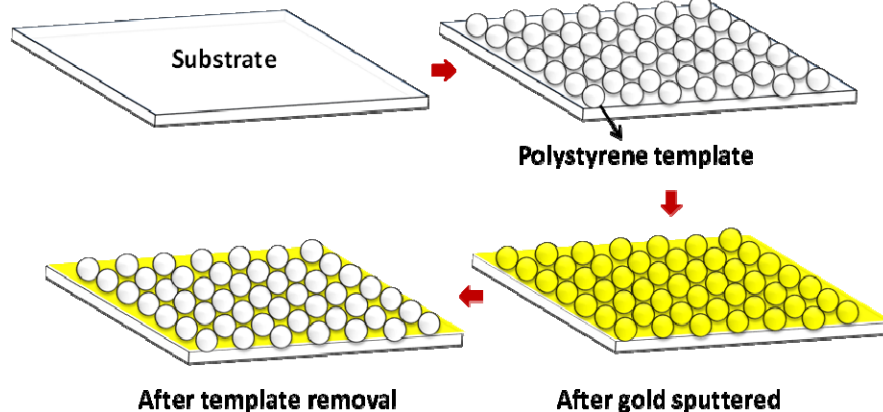


Figure 1: Schematic diagram of gold (Au) nanomesh structure using polystyrene (PS) nanosphere template in a lift - off technique.

3. Results and Discussions

As discussed above, there were three steps involving in the lift – off processes. Begin with the preparation of polystyrene (PS) template by construct a PS monolayer template on the substrate surface so that gold nanomesh structure can be arranged accordingly. Stirred mixture of PS and ethanol solutions were aimed to break the aggregation after the dilution procedure. It has reported [10-12] different stirring times can affected the PS arrangement. Thus, in this research 4 different stirring phases were applied for instance 200, 400, 600 and 800 rpm. Each of samples were then examine using FESEM as shown in Fig. 2.

For 200 rpm speed, it can be observed that the PS layer seems inhomogeneity with stackable nanosphere. Once the stirrer speed was increased, the homogeneity of the PS nanosphere has been improved as in Fig. 2 (B) and(C). However, when the speed was extended to 800 rpm, the PS nanosphere looks more scattered as in Fig. 2 (D).

In comparison, the most orderly PS nanosphere template arrangement with 600 rpm speed. Thus, sample with 600 rpm stirring speed was chosen to be coated with gold layer.

For second step, sputtered gold layer was deposited onto the PS nanosphere template with 600 rpm stirring phases. In this case, two different gold sputtering deposition approaches were carried out with samples in the rotated and fixed platform. The sputtering rate was around 15 nm/mins which resulting thickness of gold ca. 60 nm. In reality the yellow color of gold was observed on the substrate after sputtering process completed. Then, the samples were checked again using FESEM as depicted in Fig. 3.

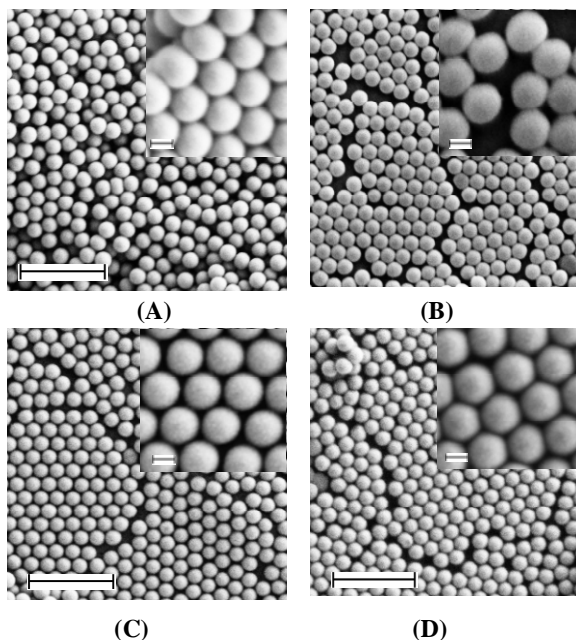


Fig. 2. FESEM images of Polystyrene (PS) nanosphere template with different coating speed (A) 200 rpm, (B) 400 rpm, (C) 600 rpm, and (D) 800 rpm. Scale for image: 1 μm and inset: 100 nm.

The images show samples after gold coated on the PS nanosphere template using DC sputtering method. Fig. 3(A) shows the gold was uniformly coated on the PS nanosphere surface with darker image by using rotated platform. On the other hand, fixed sputtering platform produced inhomogeneous gold distribution as shown in Fig. 3 (B). It can be clearly seen in the Fig. 3 (B) inset that surface morphology of fixed sputtered samples was non-uniform or uneven. It is believed that the inhomogeneous distribution of gold layer can be caused by many factors such as low current and voltage applied, the fixed platform is not suitable and size of template are not well suited. Bear in mind, the size of template must be well selected to ensure all the surface samples are covered up with gold layer until the substrate surface. In this research, the surface density of the polystyrene particle is ca. $575/\mu\text{m}^2$.

The measured size of polystyrene particles is ca. 0.2 μm ; which is same with the size given by manufacturer. Based on the density and size measurement results, it can be concluded that the distribution of gold on PS nanosphere template is not really in homogeneous condition which covered up to the substrate layer. Besides, the gold layer was not all covered in all spaces between PS nanosphere but rather coated just around the PS surface. Even this so, the experiments were conducted until the removal procedure.

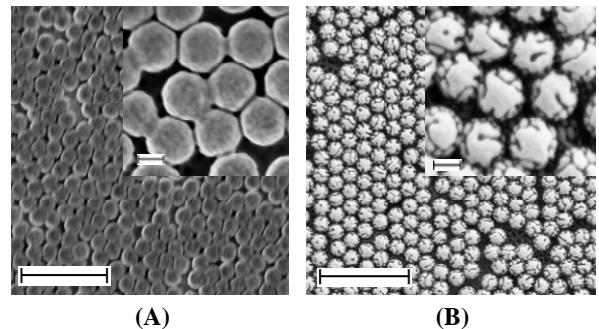


Fig. 3. After gold sputtering onto the PS template using (A) Rotation platform (B) Fixed platform. Scale for image: 1 μm and inset: 100 nm.

Lastly, the removal of polystyrene template from the substrate was proceeded or also known as lift-off process. The PS nanosphere template was removed using acetone for 3 different removal times for example 15 seconds, 30 seconds and 60 seconds. The results are shown in Fig. 4.

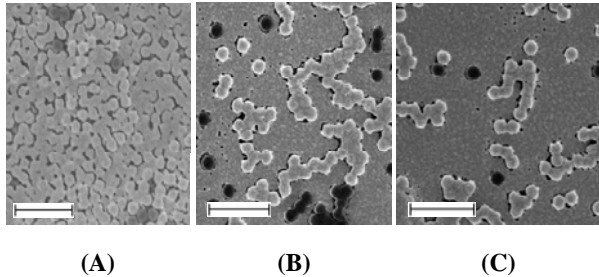


Fig. 4. After PS template removal using acetone for three different times (A) 15 seconds (B) 30 seconds and (C) 60 seconds. Scale for image: 1 μm

The PS template was removed from the substrate surface. However, the formation of gold (Au) nanomesh structure using polystyrene (PS) template was not fully transferred on the surface due to strong attraction between PS nanosphere and gold. The attraction is related with the electrostatic charging between these two types or particles. As a result, the sputtered gold was not placed in the space provided between PS nanosphere intersection areas but coated only on its top surface as mentioned before.

4. Conclusion

The formation of gold (Au) nanomesh structure using polystyrene (PS) template was not very suitable to be used in formed the gold nanomesh structure. This is because of strong attraction between PS nanosphere and gold can cause the gold not deposited in the space provided between PS particles (intersection) but only coated on its surface. As a suggestion, the PS nanosphere can be used to make as template and gold sputtering method can be replaced with synthesizing gold using wet chemical method.

Acknowledgements

This work was supported by Universiti Tun Hussein Onn Malaysia under UTHM Contract Research Grant (U565-UTHM) and IMEN, Universiti Kebangsaan Malaysia for the laboratory facilities.

References

- [1] Y. Zhang, J. Xiao, Y. Sun, L. Wang, X. Dong, J. Ren, W. He, F. Xiao, "Flexible nanohybrid microelectrode based on carbon fiber wrapped by gold nanoparticles decorated nitrogen doped carbon nanotube arrays: In situ electrochemical detection in live cancer cells," *Biosens. Bioelectron.*, vol. 100, September 2017, pp. 453–461, 2018.
- [2] B. F. G. Vadim V. Sumbayev, Inna M. Yasinska, "Biomedical Applications of Gold Nanoparticles," *Recent Adv. Circuits, Commun. Signal Process. Biomed.*, vol. 1, no. 2, pp. 10–25, 2012.
- [3] E. Hutter and J. Fendler, "Exploitation of Localized Surface Plasmon Resonance", *Advanced Materials*, vol. 16, no. 19, pp. 1685-1706, 2004.
- [4] T. Premkumar, K. Lee and K. Geckeler, "Shape-tailoring and catalytic function of anisotropic gold nanostructures", *Nanoscale Research Letters*, vol. 6, no. 1, p. 547, 2011.
- [5] M. Stewart, C. Anderton, L. Thompson, J. Maria, S. Gray, J. Rogers and R. Nuzzo, "Nanostructured Plasmonic Sensors", *Chemical Reviews*, vol. 108, no. 2, pp. 494-521, 2008.
- [6] M. Vidotti, R. Carvalhal, R. Mendes, D. Ferreira and L. Kubota, "Biosensors based on gold nanostructures", *Journal of the Brazilian Chemical Society*, vol. 22, no. 1, pp. 3-20, 2011.
- [7] P. Maury, M. Escalante, D. Reinhoudt and J. Huskens, "Directed Assembly of Nanoparticles onto Polymer-Imprinted or Chemically Patterned Templates Fabricated by Nanoimprint Lithography", *Advanced Materials*, vol. 17, no. 22, pp. 2718-2723, 2005.
- [8] X. Zhou, J. Li, C. Liu and L. Jiang, "Preparation, stability and two-dimensional ordered arrangement of gold nanoparticles capped by surfactants with different chain lengths", *Science in China Series B: Chemistry*, vol. 45, no. 4, pp. 358-364, 2002.
- [9] H. Yabu, T. Jinno, K. Koike, T. Higuchi and M. Shimomura, "Nanoparticle arrangements in block copolymer particles with microphase-separated structures", *Journal of Polymer Science Part B: Polymer Physics*, vol. 49, no. 24, pp. 1717-1722, 2011.
- [10] A. Kotera, K. Furusawa and K. Kudō, "Colloid chemical studies of polystyrene latices polymerized without any surface-active agents", *Kolloid-Zeitschrift & Zeitschrift für Polymere*, vol. 240, no. 1-2, pp. 837-842, 1970.
- [11] T. Ghoshal, A. Chaudhari, C. Cummins, M. Shaw, J. Holmes and M. Morris, "Morphological evolution of lamellar forming polystyrene-block-poly(4-vinylpyridine) copolymers under solvent annealing", *Soft Matter*, vol. 12, no. 24, pp. 5429-5437, 2016.
- [12] A. Rose, "The fabrication of polystyrene mouldings for use as a reduced density hydrogenous moderator", *Nuclear Instruments and Methods*, vol. 77, no. 1, pp. 167-169, 1970.

A REVIEW OF HARDWARE IMPLEMENTATION FOR GLUCOSE-INSULIN REGULATION IN TYPE 1 DIABETES MELLITUS PATIENT (T1DM)

Nur Atikah Mohd Daud^{1,2}, Chin-Fong Soon^{1,2}, Farhanahani Mahmud^{1,2*}

¹Department of Electronic Engineering, Universiti Tun Hussein Onn Malaysia, 86400 Parit Raja, Batu Pahat, Johor.

²Microelectronics and Shamsuddin Research Centre (MiNT-SRC), Universiti Tun Hussein Onn Malaysia, 86400, Parit Raja, Batu Pahat, Johor, MALAYSIA.

Abstract: This paper reviews on blood glucose-insulin regulation for Type 1 Diabetes Mellitus (T1DM) and recent development based on a hardware approach for the glucose-insulin regulation. T1DM is a condition where the pancreas has lost its function in producing insulin, thus required insulin injection to stabilize the glucose level. Towards achieving an artificial pancreas, there are a lot of research works have been progressively conducted from various branches starting from a simulation analysis on glucose-insulin dynamics until the development of glucose sensor, control algorithms and insulin pump. Most of mathematical models that act as a virtual patient of diabetes in the glucose-insulin regulation comprised of complex nonlinear ordinary differential equations (ODEs) which require high computational power. Moreover, over the past few years, engineers strive to realize ever smaller, lower cost and faster system in the glucose-insulin regulation through embedded systems employment which also has stringent power requirements. Thus, an approach of using high performance embedded hardware has become one of the solutions to overcome the issues as it helps to achieve in faster computational time, low power consumption and more reliable.

Keywords: Type 1 Diabetes Mellitus, mathematical model, controller, hardware

1. Introduction

Diabetes has become a worldwide concerned because the number of diabetic patients continues increasing every year. According to the recent statistic made by International Diabetes Federation (IDF), there are 415 million of people suffering from diabetes worldwide where 1 out of 11 adults has diabetes [1]. In Malaysia itself, there are 17.5% of prevalence diabetes starting at the age 18, making a total of more than three million people having diabetes [2].

Diabetes has several categories [3] and in this study, we are focusing on Type 1 Diabetes Mellitus (T1DM). The defective of β -cell of the pancreas caused insufficient amount of insulin production, thus resulting in high blood glucose (BG) concentration. Patient with T1DM required an exogenous insulin administration as a substitute function to the pancreas as to achieve normal level of BG concentration (70–140 mg/dL) [4]. A tight control of BG level is necessary to avoid any long-term complications [5].

Towards achieving a better management in insulin therapy, researchers around the world have conducted various works to fulfill the goal. To avoid ethical issues by direct testing to human subject, they have chosen mathematical modeling to carry out any related testing on BG regulation. The mathematical model will become as

the virtual patient that mimic the mechanism of the human body.

Currently, researchers are working on developing artificial pancreas [6-8]. It is a closed-loop device comprises of glucose sensor, insulin pump and control algorithm that can minimize patient's burden from frequently adjusting the amount of insulin needed. This artificial pancreas is able to automatically measured BG level and amount of insulin needed as similar function carried out by the pancreas. However, there is still an improvement needed due to the delay occurred during glucose sensing and insulin action [7].

One of the solutions to that problem is by implementing the device into a hardware platform. Further explanation can be found on section 4.

2. Diabetes and Care

T1DM is a metabolic related disease where the pancreas is unable to produce insulin sufficiently. This causes that person to experience hyperglycemia. It is a situation where the BG level is very high. Hypoglycemia, a condition of low BG concentration. It is a common situation experienced by diabetic person, normally occurred due to too high insulin injected into the body.

A person with T1DM must always aware of the BG level since it has adverse effects if not properly managed such as kidney failure, blindness and amputation [9-10].

Knowledge related to managing diabetes are important to the patient because the patients must know how to manipulate the accurate amount of insulin injected by considering various factors that could lead to vary that amount. Such factors are food intake, physical exercise and stress [11-12].

Currently, insulin can be administered into patient body through insulin syringes, insulin infusion pumps and pens [13]. The development of insulin therapy towards artificial pancreas is quite promising in achieving non-invasive treatment for better quality of life. With the advancement in nanotechnology, insulin will later can be consume orally [13]. In the market, there are several types of insulin available which can affect the BG level for a day if chosen wrongly, This is because each of the type has it owns role toward stabilizing the BG level [14-15].

3. Mathematical modeling

Research in diabetes has been done in the last five decades [16-19] and it continues todays to give a better quality of insulin therapy to diabetes patient to acquire an appropriate rate of insulin infusion [20]. The human biological system is very complex. To have a better understanding on how the body functioning especially mechanism that related to glucose stabilization, a mathematical modeling is chosen to represent the system. The research covers a wide area; ranging from clinical science to health service either using the mathematical models, statistical methods or computer algorithms. There is still a room of improvement to represent the body mechanism into mathematical model to overcome the imbalance that still exist between the current understanding and the complexity process towards managing diabetes [21].

Many of the systems in the human body have successfully transformed into mathematical modeling for simulation study such as cardiovascular and respiratory control. In the case of glucose-insulin modeling, it is much difficult because of the complexity of the pancreatic islet. But it is proven that it is possible to design mathematical modeling for BG regulation [22]. Until now, there is a lot of mathematical modeling have been designed for analysis of glucose-insulin interaction towards a better diabetes therapy treatment such as Hovorka model [23], Bergman model [22], Sturis model [24], Ackerman model [25], Sorensen model [26] and Cobelli model [27].

The mathematical modeling is very beneficial as it can simulate the regulation of BG level that later can be used to interpret and analyze for experimental data. The minimal model introduced by Bergmann [28] has lead the advancement in managing diabetes and Hovorka [23] had improved the model by implementing compartmental model. Hovorka model is a compartmental model, consist of glucose subsystem, an insulin subsystem and an insulin action subsystem [29]. The input is the subcutaneous insulin infusion and meal whereas the BG concentration as the output of the model. There are eight nonlinear

ordinary differential equations that make up the overall Hovorka mathematical structure.

Mathematical modeling is very useful because it can help the researcher to obtain knowledge on the glucose-insulin dynamic system, and to give a clear picture on how the glucose-insulin interaction works through a computer simulation [21]. This had been done before by [30] that developed the analysis system using a MATLAB Graphical User Interface (GUI) to simulate the 1-day interaction of insulin on BG level based on meal and insulin taken in T1DM patient based on the Hovorka model and by [31] that developed a simulation software of Meal Glucose-Insulin model with a MATLAB GUI to simulate 24-hour daily life of a normal, type 2, or type 1 diabetic subject based on Cobelli model [27]. Moreover, the results obtained from the computer simulation can be used for clinical purposes by testing various scenarios where the available mathematical models are also integrated with controller algorithms and the simulation outcomes are analyzed. For example, by using a model predictive control (MPC) with the Hovorka model, the glucose concentration can be predicted by controlling the insulin pump based on the output of the Hovorka model [32]. The advantages of using MPC is that it can control nonlinear system [33] and has the ability in dealing with time delays [34], however faster and longer time interval of computations for the prediction are needed. From here, the computer simulation can become a prerequisite benchmark before proceeding to the next step of developing an advance technology in glucose-insulin regulation.

The concept of in-silico testing had been done as reported in [35]. The authors had designed a complete BG regulation device into in-silico environment for computer simulation; a model of the glucose-insulin system as the in-silico subject, in-silico sensor, in-silico insulin pump and two types of controllers which were PID and a model predictive control (MPC). According to [36], using MATLAB Simulink, the performance of PD and PID controller had been evaluated on the insulin control for the BG regulation in T1DM patient based on the Hovorka model. They found that the PID controller with a fast response had given an optimum control of the glucose regulation compared to the PD controller. Meanwhile, towards achieving high computations of prediction, the authors [37] had used Palumbo delayed model together with the fuzzy logic and genetic algorithm to acquire optimal parameters on different patients. The comparison between fuzzy control and fuzzy-genetic control successfully showed that the latter could easily reached the reference glucose level.

4. Hardware implementation

Various high performance hardware platforms can be found in the market such as field programmable gate array (FPGA), microprocessor and advanced microcontroller. Recently, researchers have moved on to embedded hardware-based project to overcome computational time [38] towards a compact system with advanced performance. In the glucose-insulin regulation

research area, the controller algorithms have been implemented on the hardware platform to get a better analysis of the glucose-insulin dynamics before an advance technology can be produced. Figure 1 is the block diagram of the overall system for the glucose-insulin regulation analysis which consists of important peripherals of a virtual diabetic patient represented generally by the mathematical models as mentioned in Sec.3, control algorithm, sensor and insulin pump. Each of the peripherals complement each other in achieving optimal BG level.

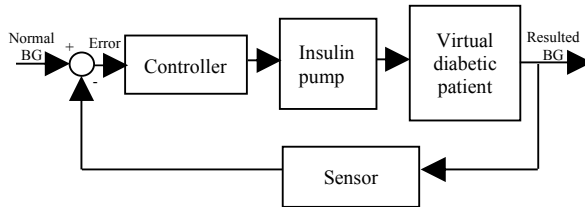


Figure 1: Overall system for the glucose-insulin regulation analysis [39]

The authors [38] had implemented their embedded model predictive controller (MPC) designed from their previous work [40] into testing application on BG regulation. The MPC had been implemented on single board computer phyCORE-MPC555. After setting up the design with the virtual patient, it showed that the BG level was managed to be kept within normal range, where it took less than one second for the controller to compute the optimal insulin dosage.

For accelerating computation of MPC operation, [41] had implemented logarithmic number system (LNS) on the proposed hardware architecture, consisting of general purpose microprocessor and auxiliary unit. The LNS can overcome disadvantage of the MPC to obtain a better performance of control [42]. The proposed hardware architecture had been tested with BG regulation problem. When the architecture was embedded into Virtex-IV FPGA board, it only took 0.688 ms to complete each time step.

Pagkalos et al. [43] was targeting towards CMOS ASIC application by applying control algorithm of

Biostator II to subcutaneous glucose sensing and insulin pump. The control algorithm was designed in fixed point number using VHDL and implemented into Altera DE2 FPGA board with embedded Nios II processor. Overall, the testing showed that the proposed design manage to control the BG level over 93% of a whole day spent within normal range.

The authors [44] had used fuzzy PD controller instead of PD controller in regulating the glucose level, focusing on power consumption within two hardware platforms; Cadence and Altera Cyclone II. Cadence gave 22.761uw compared to Altera 68uw, showing the former consumed less power.

Due to the complexity of the mathematical model that can cause low computational efficiency, the authors [45] had been used Pade approximant method to simplify the chosen mathematical model before implemented the model into Altera Cyclone II FPGA. The comparison between the original model and simplified model had shown that the simplified model is more robust by giving small root-mean-square error and accurately estimate glucose changes.

The authors in [46] used discrete-time inverse neural optimal control by implementing recurrent high order neural network on Altera DE2 FPGA board with Nios II processor. To obtain the insulin delivery rate, a control Lyapunov function was used to acquire an inverse optimal control law which helps in reducing cost functional. The controller had been trained by extended Kalman filter. Overall, the authors managed to regulate the glucose level, thus preventing from hyper and hypoglycemia episodes.

The authors in [47] had developed a model-based analysis tool using Keil simulator with selected 8051 architecture. A complete in-silico system had been developed, consisting of the chosen mathematical model, Hovorka acted as the virtual Type 1 Diabetes Mellitus (T1DM) and peripheral devices of sensor and actuator. A simple control algorithm was used to analyze the performance of each peripheral devices with the usage of error grid analysis. Table 1 shows the summary on the diabetic mathematical models used together with the embedded hardware platform.

Table 1: Summary of the glucose-insulin regulation analysis on the respective diabetic model and embedded hardware platform.

References	Year	Model	Purpose of study		Type of study	
			Analysis	Controller	Software	Hardware
Bleris et al. [38]	2005	Bergman	Computational time	Model Predictive Controller	Matlab and Simulink	phyCORE-MPC555 board and MPC555 processor
Vouzis et al. [41]	2009	Bergman	Computational time	Logarithmic Number System	C language	Xilinx Virtex IV
Pagkalos et al. [43]	2011	Cobelli and Dalla Man	Accuracy	Biostator II	VHDL	Nios II processor
Harikumar et al. [44]	2012	Ackerman	Power consumption	Fuzzy PD Controller	VHDL	Altera Cyclone II
Li et al. [45]	2016	Cobelli	Small root-mean square error	-	Matlab Simulink	Altera Cyclone II
Aragon et al. [46]	2014	Sorensen	Computational time	Discrete-time inverse neural optimal control	Matlab	Nios II processor
El-Gemayel et al. [47]	2013	Hovorka	Controller performance	Simple controller	C language	Intel 8051 Microcontroller

5. Conclusion

Overall, this review paper has given a brief picture on glucose-insulin regulation for hardware implementation approach. Those ideas can be further explored towards achieving artificial pancreas for better control of BG concentration throughout a day. The pancreas of diabetic patient with T1DM is unable to produce adequate amount of insulin, thus requires insulin injection to the role of the pancreas. To predict near-to-normal BG concentration, various controller has been developed, later implemented into hardware platform for a realistic testing. The major constraints of glucose regulation to implement into hardware that have been found in this review are on computation time and power consumption. There is still a room of improvement to tackle those constraints such as towards advancement of system-on-chip [48,49].

References

- [1] International Diabetes Federation. *IDF Diabetes Atlas, 7th edn.* Brussels, Belgium: International Diabetes Federation, 2015.
- [2] Institute for Public Health (IPH) 2015. National Health and Morbidity Survey 2015 (NHMS 2015). Volume II: Non-Communicable Diseases, Risk Factors and Other Health Problems; 2015.
- [3] American Diabetes Association. Classification and diagnosis of diabetes. *Diabetes Care*, Volume 38 (1), (2015), pp. S8-S16.
- [4] Soru, P., Nicolao, G. D., Man, C. D., Cobelli, C., and Magni, L. MPC based artificial pancreas: strategies for individualization and meal compensation. *Annual Reviews in Control*, Volume 36 (1), (2012), pp. 118-128.
- [5] Dennedy, M. C., and Dinneen, S. F. Management of type 1 diabetes mellitus. *Medicine*, Volume 38 (11), (2010), pp. 610-617.
- [6] Renard, E., Cobelli, C., and Kovatchev, B. P. Closed loop developments to improve glucose control at home. *Diabetes Research and Clinical Practice*, Volume 102 (2), (2013), pp. 79-85.
- [7] Cobelli, C., Renard, E., and Kovatchev, B. Artificial pancreas: past, present, future. *Diabetes*, Volume 60 (11), (2011), pp. 2672-2682.
- [8] Thabit, H., and Hovorka, R. Coming of age: the artificial pancreas for type 1 diabetes. *Diabetologia*, Volume 59 (9), (2016), pp. 1795-1805.
- [9] Wild, D., Maltzahn, R. V., Brohan, E., Christensen, T., Clauson, P., and Frederick, L. G. A critical review of the literature on fear of hypoglycemia in diabetes: Implications for diabetes management and patient education. *Patient Education Counseling*, Volume 68 (1), (2007), pp. 10-15.
- [10] Elleri, D., Dunger, D. B., and Hovorka, R. Closed-loop insulin delivery for treatment of type 1 diabetes. *BMC Medicine*, Volume 9 (1), (2011), pp. 120.
- [11] Jumel, F., Abouchi, N., Constantin, J., Tabet, A., and Zaouk, D. An in-silico study for glucose-insulin system based on microcontroller using system simulator. *25th International Conference on Microelectronics (ICM)*, (2013).
- [12] Wilcox, G. Review: Insulin and insulin resistance. *The Clinical Biochemist Reviews*, Volume 26 (2), (2005), pp. 19-39.
- [13] Yaturu, S. Insulin therapies: Current and future trends at dawn. *World Journal of Diabetes*, Volume 4 (1), (2013), pp. 1-7.
- [14] Mathieu, C., Gillard, P., and Benhalima, K. Review: Insulin analogues in type 1 diabetes mellitus: getting

- better all the time. *Nature Reviews Endocrinology*, Volume 13, (2017), pp 385-399.
- [15] Jayakrishnapillai, P. V., Shantikumar, V. N., and Kamalasan, K. Review: Current trend in drug delivery considerations for subcutaneous insulin depots to treat diabetes. *Colloids and Surfaces B: Biointerfaces*, Volume 153, (2017), pp. 123-131.
- [16] Berman, R. N., Philips, L. S., and Cobelli, C. Physiologic evaluation of factors controlling glucose tolerance in man from the response to intravenous glucose. *Journal of Clinical Investigation*, Volume 68 (6), (1981), pp. 1456-1467.
- [17] Chen, C. L., and Tsai, H. W. Modeling the physiological glucose-insulin system on normal and diabetic subjects. *Computer Methods and Programs in Biomedicine*, Volume 97 (2), (2010), pp. 130-140.
- [18] Cobelli, C., Man, C. D., Pedersen, M. G., Bertoldo, A., and Toffolo, G. Advancing our understanding of the glucose system via modeling: a perspective. *IEEE Transactions on Biomedical Engineering*, Volume 61 (5), (2014), pp. 1577-1592.
- [19] Wilinska, M. E., Chassin, L. J., Schaller, H. C., Schaupp, L., Pieber, T. R., and Hovorka, R. Insulin kinetics in type-1 diabetes: continuous and bolus delivery of rapid acting insulin. *IEEE Transactions on Biomedical Engineering*, Volume 52 (1), (2005), pp. 3-12.
- [20] Ahmed, J., Alvi, B. A., and Ali, Z. K. Blood glucose-insulin regulation and management system using MATLAB/SIMULINK. *4th International Conference on Emerging Technologies*. 2008.
- [21] Ajmera, I., Swat, M., Laibe, C., Novere, N. L., and Chelliah, V. Review: The impact of mathematical modeling on the understanding of diabetes and related complications. *CPT Pharmacometrics Systems Pharmacology*, Volume 2 (7), (2013), pp. 1-14.
- [22] Bergman, R. N. Minimal model: perspective from 2005. *Hormone Research in Paediatrics*, Volume 64 (3), (2005), pp. 8-15.
- [23] Hovorka, R., Moradie, F. S., Carroll, P. V., Chassin, L. J., Gowrie, I. J., Jackson, N. C., Tudor, R. S., Umpleby, A. M., and Jones, R. H. Partitioning glucose distribution/transport, disposal, and endogenous production during IVGTT. *American Journal of Physiology – Endocrinology and Metabolism*, Volume 282 (5), (2002), pp. E992-E1007.
- [24] Sturis, J., Polonsky, K. S., Mosekilde, E., and Cauter, E. V. Computer model for mechanisms underlying ultradian oscillations of insulin and glucose. *American Journal of Physiology – Endocrinology and Metabolism*, Volume 260 (5), (1991), pp. E801-E809.
- [25] Ackerman, E., Rosevear, J. W., and McGuckin, W. F. A mathematical model of the glucose-tolerance test. *Physics in Medicine and Biology*, Volume 9 (2), (1964), pp. 203-213.
- [26] Sorensen, J. T. A physiologic model of glucose metabolism in man and its used to design and assess improved insulin therapies for diabetes. Massachusetts Institute of Technology, (1985), PhD Thesis.
- [27] Man, C. D., Rizza, R. A. and Cobelli, C. Meal simulation model of the glucose-insulin system. *IEEE Transactions on Biomedical Engineering*, Volume 54 (10), (2007), pp. 1740-1749.
- [28] Bergman, R. N., Ider, Y. Z., Bowden, C. R., and Cobelli, C. Quantitative estimation of insulin sensitivity. *American Journal of Physiology – Endocrinology and Metabolism*, Volume 236 (6), (1979), pp. E667-E677.
- [29] Hovorka, R., Canonico, V., Chassin, L. J., et al. Nonlinear model predictive control of glucose concentration in subjects with type 1 diabetes. *Physiological Measurement*, Volume 25, (2004), pp. 905-920.
- [30] Daud, N. A. M., Sabri, A. F. M. and Mahmud, F. Simulation-based analysis system of glucose-insulin dynamics in type 1 diabetes mellitus. *Journal of Telecommunication, Electronic and Computer Engineering (JTEC)*, Volume 9 (3-8), (2017), pp. 133-137.
- [31] Man, C. D., Rizza, R. A., Raimondo, D. M. and Cobelli, C. GIM, Simulation software of meal glucose-insulin model. *Journal of Diabetes Science and Technology*, Volume 1 (3), (2007), pp. 323-330.
- [32] Pedersen, S. N., and Hansen, L. B. System identification for prediction of glucose levels in people with type 1 diabetes. Technical University of Denmark, (2010), Bachelor Degree Thesis.
- [33] Wang, Y., Dassau, E., and Doyle, F. J. Closed-loop control of artificial pancreatic β -cell in type 1 diabetes mellitus using model predictive iterative learning control. *IEEE Transactions on Biomedical Engineering*, Volume 57 (2), (2010), pp. 211-219.
- [34] Jiang, X., Wang, Y. Closed-loop glycemic control for critically ill subjects based on data-driven model predictive control. *Proceedings of the 31st Chinese Control Conference*, (2012), pp. 7061-7066.
- [35] Kovatchev, B. P., Breton, M., Man, C. D., and Cobelli, C. In silico preclinical trials: A proof of concept in closed-loop control of type 1 diabetes. *Journal of Diabetes Science and Technology*, Volume 3 (1), (2009), pp. 44-55.
- [36] Mahmud, F., Isse, N. H., Daud, N. A. M., and Morsin, M. Evaluation of PD/PID controller for insulin control on blood glucose regulation in a Type-I diabetes. *AIP Conference Proceedings* 1788, (2017), pp. 030072-1-030072-7.
- [37] Heydari, V., Karsaz, A., Heydari, R. A new hybrid approach on blood glucose level control based on Palumbo delayed model. *Proceedings on IEEE International Conference on Computational Science and Engineering, IEEE International Conference on Embedded and Ubiquitous Computing and International Symposium on Distributed Computing and Applications to Business, Engineering and Science*, (2017).

- [38] Bleris, L. G., and Kothare, M. V. Implementation of model predictive control for glucose regulation on a general purpose microprocessor. *Proceedings of the 44th IEEE Conference on Decision and Control and the European Control Conference*, (2005).
- [39] Srinivas, P., and Rao, P. D. P. Closed loop model for glucose insulin regulation system using labview. *International Journal of Instrumentation and Control Systems*, Volume 2 (4), (2012), pp. 93-102.
- [40] Bleris, L. G., Garcia, J., Kothare, M. V., and Arnold, M. G. Towards embedded model predictive control for System-on-Chip applications. *Journal of Process Control*, Volume 16 (3), (2006), pp. 255-264.
- [41] Vouzis, P. D., Bleris, L. G., Arnold, M. G., and Kothare, M. V. A system-on-chip implementation for embedded real-time model predictive control. *IEEE Transactions on Control Systems Technology*, Volume 17 (5), (2009), pp. 1006-1017.
- [42] Garcia, J., Arnold, M. G., Bleris, L., and Kothare, M. V. LNS architecture for embedded model predictive control processors. *Proceedings of the 2004 International Conference on Compilers, Architecture and Synthesis for Embedded System*, (2004), pp. 79-84.
- [43] Pagkalos, I., Herrero, P., El-Sharkawy, M., Pesl, P., Oliver, N., and Georgiou, P. A VHDL implementation of the biostator II glucose control algorithm for critical care. *IEEE Biomedical Circuits and Systems Conference*, (2011).
- [44] Harikumar, R., Sudhaman, V. K., and Babu, C. G. FPGA synthesis of fuzzy (PD and PID) controller for insulin pumps in diabetes using Cadence. *International Journal of Soft Computing and Engineering*, Volume 1 (6), (2012), pp. 324-331.
- [45] Li, P., Yu, L., Fang, Q., and Lee, S. Y. A simplification of Cobelli's glucose-insulin model for type 1 diabetes mellitus and its FPGA implementation. *Medical and Biological Engineering & Computing*, Volume 54 (10), (2016), pp. 1563-1577.
- [46] Aragon, J. C., Sanchez, E. N., and Alanis, A. Y. Glucose level regulation for diabetes mellitus type 1 patients using FPGA neural inverse optimal control. *IEEE Symposium on Computational Intelligence in Control and Automation*, (2014).
- [47] El-Gemayel, C., Jumel, F., Abouchi, N., Constantin, J., Tabet, A., and Zaouk, D. An in-silico study for glucose-insulin system based on microcontroller using system simulator. *25th International Conference on Microelectronics*, (2013).
- [48] Daud, N. A. M., Mahmud, F., and Jabbar, M. H. Meal simulation in glucose-insulin reaction analysis using hovorka model towards system-on-chip implementation. *ARPN J. of Eng. and Applied Sci.*, Volume 10 (19), pp. 8927-8935.
- [49] Daud, N. A. M., Mahmud, F., and Jabbar, M. H. A hardware acceleration based on high-level synthesis approach for glucose-insulin analysis. *AIP Conference Proceedings* 1788, (2017), pp. 030087-1-030087-6.

A REVIEW ON THE CURRENT 3D BIOPRINTING TECHNOLOGY

Sheril Amira Othman¹, Chin Phong Soon^{1,2*}, Farshid Sefat³, Kian Sek Tee¹, Mohd Khairul Ahmad^{1,2}, Nafarizal Nayan^{1,2}

¹Department of Electrical Engineering, Universiti Tun Hussein Onn Malaysia, Johor 86400, MALAYSIA.

²Microelectronic and Nanotechnology-Shamsuddin Research Center (MiNT-SRC), Universiti Tun Hussein Onn Malaysia, Johor 86400, MALAYSIA.

³Faculty of Engineering and Informatics, Medical Engineering Department, University of Bradford, Bradford, BD7 1DP, UK.

Abstract: Three-dimensional (3D) bioprinting is an uprising technology that will soon outweigh the traditional scaffold methods in cells and tissue engineering in terms of reconstructing the structures of tissue or organs. This rapid prototyping method capable to mimic the native tissue architecture of 3D microenvironment that possesses the characteristics of stimulating structural support, cells proliferation and cells differentiation. However, the bioprinting technology will continuously be improved and optimised for wide variety of functional organs that the patients are waiting for. This review paper describes the major types of bioprinting technology, the three main steps in printing process, and the previous development of the technology. The properties of 3D bioprinting ink or bioink used in previous studies are highlighted. The limitations and future development are also discussed in this paper.

Keywords: 3D bioprinting, organ transplantation, microenvironment, bioink

1. Introduction

Organ transplantation has saved numerous patients around the world since its first successful procedure of transplanting a living kidney between identical twins back in 1954 [1]. However, the number of organ donors are still fewer than the percentage of the recipients who are waiting for transplantation. Currently, there are approximately 23,091 organ transplants had been performed in 2017 in United States of America whereas the total of 116,500 patients are in need of organ transplants [2]. Meanwhile, in Malaysia, there were reported about 20,774 patients on waiting lists for organ transplants as of August 2016 [3]. The highest demand for organ transplant waiting list are from the patients with kidney failure and only 1% of the Malaysians had pledged to contribute as organ donors. In fact, the demanding of vital organ transplantation such as kidney, liver and heart are continuously multiplying surpasses the availability of the organs from potential donors.

Therefore, biomedical engineers are urged to recreate structures of the damaged, wounded tissues or organs as a new approach to overcome the shortage of organs in the field of tissue engineering. Three-dimensional (3D) bioprinting had been introduced as a new way in tissue engineering for recreating organ structures while preserving the viability and cell function through the usage of 3D technology. Bioprinting employed the layer-by-layer method in depositing and constructing the biological components for the use of medical purposes

[4]. The first 3D engineered organ implantation was performed by Atala et al. (1999) [5] of Wake Forest Institute for Regenerative Medicine for a patient who needed urinary bladder transplantation by using 3D synthetic polyglycolide and collagen scaffold of the patient's own cells.

This paper overviews the major types of bioprinting technology, the important steps in printing, and its previous development. In addition, this review paper summarized the source of bioink polymers, the physical and biochemistry properties, crosslinking features, advantages and disadvantages of the bioprinting ink.

2. The fundamental processes of 3D bioprinting

3D bioprinting can be defined as additive manufacturing or rapid prototyping that can produce solid objects layer-by-layer based on designs created using computer aided design (CAD) software [6]. This method are widely used to produce bio-engineered structures serving in regenerative medicine and other medical purposes such as prosthetics and dental applications. The process of bioprinting can be classified into three steps that are preprocessing, processing and post-processing [7]. Preprocessing is the preliminary stage of bioprinting or referred as the development of computer-aided design, normally called as the "blueprint" [8]. The blueprint in stereolithography file format is used as the instructions for bioprinter that includes 3D reconstruction and

mathematical modeling of objects. Bioprinting process continues with deposition of biomaterials components from the bioprinter as the bioprinting ink or bioink [9]. Usually, the bioink that contains cells will be dispensed onto a biocompatible hydrogel film or biopaper which functions as the scaffold and mimic the 3D microenvironment of the cells. Post-processing is important in ensuring the viability of the tissues and maintain the mechanical properties and functionality of the 3D printed tissues or organs. Recent development of bioreactor helps to accelerate the maturation of the printed tissues according to the environment prepared in the bioreactor system [10].

3. 3D Bioprinting Techniques

The major technology in bioprinting are categorized as stereolithography, inkjet-based, extrusion and laser-assisted bioprinting [11].

3.1 Stereolithography

The stereolithography based bioprinting system used an array of digital micromirror to control the light intensity of the pixels in the specified printing area where the light-sensitive hydrogels will be polymerized layer by layer [12]. In 1984, Chuck Hull had successfully patented the first stereolithography printer which works by focusing ultraviolet light to cure photosensitive biopolymers[13]. However, the ultraviolet (UV) light had been a major crisis to be applied in bioprinting as it is harmful to the biological components.

Based on the subsequent development of stereolithography bioprinter by Zongjie Wang et al.[14] in 2015, a water filter was used between the beam projector of the light source and petri dish to remove the byproduct of radiation produced from the infrared light that could harm the cells. The UV light medium was changed to visible light to maintain the cell-functionality [15]. Karina Arcaute et al. [16] from University of Texas proved that the cytotoxicity increased when the photo initiator concentration is increased.

3.2 Inkjet-based

The simplest bioprinting technology is basically from the modification of 2D desk printer especially the printer ink replaced into bioink with cells. Inkjet-based bioprinting technology used drop-on-demand deposition mechanisms in fabricating the biological structures [17]. In drop-on-demand mechanism, the printer cartridge is filled with the hydrogels and cells which is connected to the printer head before electronically controlled to drop one-by-one simultaneously. In inkjet bioprinting system, there are two methods that are used frequently to deposit the bioink known as thermal inkjet and piezoelectric inkjet head.

Thermal inkjet printer was introduced to overcome the limitation of inkjet-based printer which only allowed the usage of certain biomaterials [18]. Thermal inkjet applies heat to generate small bubbles followed by

pressure pulses to eject ink drops with various volume from 10-150 pL [19]. Meanwhile, in piezoelectric inkjet bioprinting, the actuators or piezocrystals are actuated because of the transient pressure produced when electrical signals are applied, thus, break the bioink into small droplets.

According to Xiaofeng Cui et al.[20], the viability of the cells in thermal inkjet process is 90% and higher than in piezoelectric inkjet process which means that the heat thermal inkjet is safe for the depositing cells. Nonetheless, Makoto Nakamura et al.[21] (2007) successfully fabricated 3D tubular and sheet structure by using piezoelectric inkjet head.

3.3 Extrusion

Extrusion bioprinting technology involves with mechanical or pneumatic syringe dispensing systems by applying continuous pressure to deposit bioink without any interruption or separated droplets [22]. The extrusion method has the ability to print porous constructions due to its characteristic in printing materials. The bioink is usually loaded into a syringe that coupled to an extruder. Pneumatic, piston-driven and screw-based motorized system are the backbone in extrusion technology. The pneumatic systems in extrusion bioprinting can cause some delays in dispensing biomaterials due to the gas compression but working well with highly viscous materials. The piston-driven system in extrusion technology offers a direct control over the hydrogel while the screw-based motorized system offers a spatial control over high viscosity hydrogel [23].

In 2014, Ibrahim T. Ozbalat et. al [24] had designed an extrusion bioprinter with multiple arm or ‘multi-arm bioprinter’ (MABP). It was built to concurrently printing a filament structure and depositing cell spheroids in between the filament in order to create hybrid structure for supporting function. Weitao Jia et al.[25] had developed a coaxial nozzle bioprinter in 2016 which contained two injection channels and different needles to fabricate the perfusable vascular structure.

3.4 Laser-assisted

Laser-assisted technology is a non-contact printing method that eliminates the mechanical stress in the cells by using laser as the energy source to deposit bioink [26]. It consists of three parts which are pulsed laser source, ribbon coated with liquid biomaterials that deposited on the metal film and a biopaper made up from receiving substrate such as collagen [27]. A laser pulse will be focused to a small area of the absorbing layer and vaporized the targeted layer. The targeted layer is also called as donor layer which have a ribbon-like structure usually of energy-absorbing material such as titanium and gold. This process will create a high-pressure bubble on the interface of the bioink layer and propelled the suspended bioink. Although the laser light is a high energy photons source that could cause photo-stress to the cells but it does not affect the cell viability which is 95%. Because this technology is a nozzle-free system and the

Bioink	Source	Properties	Crosslinking features	Disadvantages	Reference
Alginate	natural	biocompatibility, high mechanical strength, gelation at ideal temperature, enable various of crosslinking	rapid crosslinking	lack of cell recognition site	[39]
Collagen	natural	high mechanical strength, shear thinning, high stability, better cell adhesion	slow crosslinking, usually blended with faster-crosslink gel	longer gelation time	[40]
Fibrin	natural	strain-stiffening properties, non-linear elasticity, high compatibility	crosslink through thrombin	low mechanical properties	[41]
Polyethylene glycol (PEG)	synthetic	strong robust hydrogel, bioinert, variable molecular weight with tunable properties	required modification	viscosity too high, weak mechanical properties	[42]
Polylactic acid (PLA)	synthetic	semi crystalline polymer, excellent mechanical strength, biodegradable, less viscous	require mixture with other biopolymer	unable to encapsulate cells due to high temperature to print	[43]
Polylactic-co-glycolic acid (PLGA)	synthetic	thermoplastic polymer, controllable degradation rate, fast solvent evaporation	require mixture with other biopolymer	require high temperature to print	[44]

Table 1 Summary of bioink sources, the biophysical properties, crosslink features and the disadvantage of bioink

nozzle geometry does not cause any mechanical stress to the cells.

This is a less popular method due to the high expenditure of the bioprinter and safety issue. One of the previous development of laser-assisted bioprinting was reported by Bertrand et al. in 2010 [28] with some adjustments to the cell concentration on the ribbon and the laser parameters were made based on the viscosity of the bioink. These adjustments were made to ensure that the cells were printed droplet by droplet within a small volume of bioink.

In 2012, Stefanie Michael et al. [29], added a dorsal skin fold chamber in the laser-assisted bioprinter as a way to reduce the wound areas of the experimented mouse during the laser process.

4. Bioink

Bioink or bioprinting ink is a biomaterial made from living cells and biopolymers that mimics the extracellular matrix and functions as the printing ink in bioprinting technology [30]. Bioink can be divided into two main components that are the natural biopolymers and synthetic biopolymers. Table 1 shows the source of the most commonly used bioink reported in previous development, the properties possess by the bioink, the crosslink features and disadvantage of bioink. There are a lot of development related to the natural polymers because of its biocompatibility and ability to mimic the physical properties of the tissue environment. However,

there are also researchers who favors synthetic polymers as the bioink because the structures and stiffness of synthetic materials can easily be altered to enhance the cellular performance [31].

Alginate is a low cost natural polymer obtained from brown algae. It is the most common bioink used in most of the research because it is nontoxic and owns broad range of viscosity at room temperature [32]. Nonetheless, collagen and fibrin are also used as bioinks because they contain both natural proteins in human body [33]. In these natural proteins, the RGD sequence functions as cell-binding sites which helps to stimulate the cells adhesion. For synthetic biopolymers used as bioink, polyethylene glycol (PEG), polylactic acid (PLA) and polylactic-co-glycolic acid (PLGA) are among the popular bio-polymers often used in research activity [34]. These synthetic polymers are modified to enhance the mechanical properties of the bioink [35] and become more compatible with the cells. In regenerative medicine, these biodegradable polymers are used for bone regeneration because of its mechanical strength [36].

5. Limitations and future development

Limitations are still existed in 3D bioprinting technology such as the resolution, user-friendliness and the accuracy of the bioprinter [37]. Most of the technology used complex system and difficult to handle. The hygienic factor of the biomaterials in the process is also controversial. Furthermore, most of the natural

biomaterials applied as bioink lacks of mechanical properties [38]. In future, the resolution of the bioprinter need to be upgraded and accuracy of the printing area. A simple yet low cost bioprinter will catalyze the wide spread of bioprinting technology. The materials or polymers desired in bioink must be experimented first to identify the perfect bioink with improved mechanical properties in order to support the structure. The combination between natural and synthetic polymers can be studied to determine the cellular response of the cells. In future, various types of artificial and biodegradable tissue or organ structures can be printed to explore more in tissue engineering. In the near future, they are vast possibilities of producing artificial heart, nose, bones and fingers by bioprinting technology to serve mankind.

6. Summary

This paper overviews the three main steps in printing process, the major types of bioprinting technology and the previous development of the technology. The properties of 3D bioprinting ink or bioink used in previous studies were highlighted. Limitation and the future development are also discussed in this paper. Thus, the development of 3D bioprinting technology are ought to be continuously advanced while reducing complicity because it is a promising approach to reduce the organ shortage issues.

References

- [1] G. B. Klintmalm, ‘The history of organ transplantation in the Baylor Health Care System.’, *Proc. (Bayl. Univ. Med. Cent.)*, vol. 17, no. 1, pp. 23–34, 2004.
- [2] ‘National Data Transplantation’, *UNOS*, 2017. [Online]. Available: <https://unos.org/data/>. [Accessed: 02-Nov-2017].
- [3] O. Miwil, ‘Only 1.4 per cent of Malaysians are pledged organ donors’. [Online]. Available: <https://www.nst.com.my/news/2016/10/180424/only-14-cent-malaysians-are-pledged-organ-donors>. [Accessed: 02-Oct-2017].
- [4] Maika G. Mitchell, ‘Chapter 2 – Applications of 3D Printing in Cell Biology’, *AcademicPress*, pp. 121–162, 2016.
- [5] A. S. Munoz-Abraham, M. I. Rodriguez-Davalos, A. Bertacco, B. Wengerter, J. P. Geibel, and D. C. Mulligan, ‘3D Printing of Organs for Transplantation: Where Are We and Where Are We Heading?’, *Curr. Transplant. Reports*, vol. 3, no. 1, pp. 93–99, 2016.
- [6] B. K. Gu, D. J. Choi, S. J. Park, M. S. Kim, C. M. Kang, and C.-H. Kim, ‘3-Dimensional Bioprinting for Tissue Engineering Applications’, *Biomater. Res.*, vol. 20, no. 1, p. 12, 2016.
- [7] ‘3D Printing Process’. [Online]. Available: <http://3dprintingfromscratch.com/common/3d-printing-process/>. [Accessed: 01-Nov-2017].
- [8] S. El Bialy, ‘The 3 D Printing Age and Basic Sciences Education’, *Educ. Med. J.*, vol. 8, no. 4, pp. 79–82, 2016.
- [9] X. Wang *et al.*, ‘Gelatin-based hydrogels for organ 3D bioprinting’, *Polymers (Basel.)*, vol. 9, no. 9, 2017.
- [10] ‘Bioreactor’. [Online]. Available: <https://en.wikipedia.org/w/index.php?title=Bioreactor&oldid=85300000>. [Accessed: 31-Oct-2017].
- [11] Chinthu V Saji, ‘3D bioprinting system’. [Online]. Available: <https://www.slideshare.net/chinthuvsa1/bioprinting>. [Accessed: 29-Oct-2017].
- [12] ‘Stereolithography Technology’. [Online]. Available: <https://www.3dnatives.com/en/stereolithography-explained100420174/>. [Accessed: 03-Oct-2017].
- [13] ‘Stereolithography Explained’. [Online]. Available: <http://everything.explained.today/Stereolithography/>. [Accessed: 30-Oct-2017].
- [14] Z. Wang, ‘Development of A Visible Light Stereo Lithography-Based Bio Printing System for Tissue Engineering Zongjie Wang Master of Applied Science’, no. May, 2016.
- [15] Z. Wang, R. Abdulla, B. Parker, R. Samanipour, S. Ghosh, and K. Kim, ‘A simple and high-resolution stereolithography-based 3D bioprinting system using visible light crosslinkable bioinks’, *Biofabrication*, vol. 7, no. 4, p. 45009, 2015.
- [16] K. Arcuate, B. Mann, and R. Wicker, ‘Stereolithography of spatially controlled multi-material bioactive poly(ethylene glycol) scaffolds’, *Acta Biomater.*, vol. 6, no. 3, pp. 1047–1054, 2010.
- [17] K. W. Binder, A. J. Allen, J. J. Yoo, and A. Atala, ‘Drop-on-demand Inkjet Bioprinting: A Primer’, *Gene Ther. Regul.*, vol. 6, no. 1, pp. 33–49, 2011.
- [18] P. H. Chen, W. C. Chen, P. P. Ding, and S. H. Chang, ‘Droplet formation of a thermal sideshooter inkjet printhead’, *Int. J. Heat Fluid Flow*, vol. 19, no. 4, pp. 382–390, 1998.
- [19] P.-H. Chen, W.-C. Chen, and S.-H. Chang, ‘Bubble growth and ink ejection process of a thermal ink jet printhead’, *Int. J. Mech. Sci.*, vol. 39, no. 6, pp. 683–695, 1997.
- [20] X. Cui, T. Boland, D. D. D'Lima, and M. K. Lotz, ‘Thermal inkjet printing in tissue engineering and regenerative medicine.’, *Recent Pat. Drug Deliv. Formul.*, vol. 6, no. 2, pp. 149–55, 2012.
- [21] C. Henmi *et al.*, ‘Development of an effective three dimensional fabrication technique using inkjet technology for tissue model samples’, pp. 689–692, 2007.

- [22] ‘Organ Printing’. [Online]. Available: https://en.wikipedia.org/wiki/Organ_printing. [Accessed: 28-Oct-2017].
- [23] F. Pati, J. Jang, J. W. Lee, and D. W. Cho, *Extrusion bioprinting*, no. December. 2015.
- [24] I. T. Ozbolat, H. Chen, and Y. Yu, ‘Robotics and Computer-Integrated Manufacturing Development of “ Multi-arm Bioprinter ” for hybrid biofabrication of tissue engineering constructs’, *Robot. Comput. Integrat. Manuf.*, vol. 30, no. 3, pp. 295–304, 2014.
- [25] W. Jia, P. S. Gungor-ozkerim, Y. Shrike, and K. Yue, ‘Biomaterials Direct 3D bioprinting of perfusable vascular constructs using a blend bioink’, *Biomaterials*, vol. 106, pp. 58–68, 2016.
- [26] S. Ji and M. Guvendiren, ‘Recent Advances in Bioink Design for 3D Bioprinting of Tissues and Organs’, *Front. Bioeng. Biotechnol.*, vol. 5, no. April, pp. 1–8, 2017.
- [27] V. Keriquel *et al.*, ‘In situ printing of mesenchymal stromal cells, by laser-assisted bioprinting, for in vivo bone regeneration applications’, *Sci. Rep.*, vol. 7, no. 1, p. 1778, 2017.
- [28] B. Guillotin *et al.*, ‘Biomaterials Laser assisted bioprinting of engineered tissue with high cell density and microscale organization’, *Biomaterials*, vol. 31, no. 28, pp. 7250–7256, 2010.
- [29] S. Michael *et al.*, ‘Tissue Engineered Skin Substitutes Created by Laser-Assisted Bioprinting Form Skin-Like Structures in the Dorsal Skin Fold Chamber in Mice’, *PLoS One*, vol. 8, no. 3, 2013.
- [30] ‘Bioink’. [Online]. Available: <https://en.wikipedia.org/wiki/Bio-ink>. [Accessed: 02-Nov-2017].
- [31] I. T. Ozbolat and I. T. Ozbolat, ‘3 – The Bioink’, in *3D Bioprinting*, 2017, pp. 41–92.
- [32] S. A. Irvine and S. S. Venkatraman, ‘Bioprinting and differentiation of stem cells’, *Molecules*, vol. 21, no. 9, 2016.
- [33] A. Panwar and L. P. Tan, ‘Current status of bioinks for micro-extrusion-based 3D bioprinting’, *Molecules*, vol. 21, no. 6, 2016.
- [34] C. Mandrycky, Z. Wang, K. Kim, and D. Kim, ‘3D Bioprinting for Engineering Complex Tissues’, vol. 34, no. 4, pp. 422–434, 2017.
- [35] J. H. Y. Chung *et al.*, ‘Bio-ink properties and printability for extrusion printing living cells’, *Biomater. Sci.*, vol. 1, no. 7, p. 763, 2013.
- [36] F. Matassi, L. Nistri, D. C. Paez, and M. Innocenti, ‘New biomaterials for bone regeneration’, *Clin. Cases Miner. Bone Metab.*, vol. 8, no. 1, pp. 21–24, 2011.
- [37] A. B. Dababneh and I. T. Ozbolat, ‘Bioprinting Technology : A Current State-of-the-Art Review’, vol. 136, no. December, pp. 1–11, 2014.
- [38] A. L. Rutz, K. E. Hyland, A. E. Jakus, W. R. Burghardt, and R. N. Shah, ‘A Multi-Material Bioink Method for 3D Printing Tunable, Cell-Compatible Hydrogels’, vol. 27, no. 9, pp. 1607–1614, 2015.
- [39] J. Jia *et al.*, ‘Engineering alginate as bioink for bioprinting’, *Acta Biomater.*, vol. 10, no. 10, pp. 4323–4331, 2014.
- [40] S. A. Sell, P. S. Wolfe, K. Garg, J. M. McCool, I. A. Rodriguez, and G. L. Bowlin, ‘The use of natural polymers in tissue engineering: A focus on electrospun extracellular matrix analogues’, *Polymers (Basel).*, vol. 2, no. 4, pp. 522–553, 2010.
- [41] P. A. Janmey, J. P. Winer, and J. W. Weisel, ‘Fibrin gels and their clinical and bioengineering applications’, *J. R. Soc. Interface*, vol. 6, no. 30, pp. 1–10, 2009.
- [42] A. Skardal *et al.*, ‘A hydrogel bioink toolkit for mimicking native tissue biochemical and mechanical properties in bioprinted tissue constructs’, *Acta Biomater.*, vol. 25, pp. 24–34, 2015.
- [43] ‘Matrix Bioinks’. [Online]. Available: <https://www.biobots.io/biowiki/matrix-bioinks/>. [Accessed: 03-Nov-2017].
- [44] U. D. Bret, N. S. Lakshmi, and C. T. Laurencin, ‘Biomedical Applications of Biodegradable Polymers’, *J. Polym. Sci. Part B Polym. Phys.*, vol. 3, no. 49, pp. 832–864, 2011.

FUZZY LOGIC SYSTEM FOR MENSTRUAL CYCLE INTERPRETATION BASED ON BBT DATA

Muhammad Syukri Mohd Yazed^{1,2}, Ariff Farhan Zainodin¹, Farhanahani Mahmud^{1,2}

¹Department of Electronics Engineering, Faculty of Electrical and Electronics Engineering,

²Cardiology and Physiome Analysis Research Laboratory,

Microelectronics and Nanotechnology Shamsuddin Research Centre (MiNT-SRC),

University of Tun Hussein Onn Malaysia (UTHM), 86400 Parit Raja, Batu Pahat, JOHOR.

Abstract: Basal body temperature (BBT) data have been used for so long as a simple method in estimating the day of ovulation occurred and to understand menstrual cycle that is unique for every woman. The BBT is considered to be a reliable ovulatory index, since most women will have increased temperature in the luteal phase of the cycle. However, the problems faced are the studies of validating the efficacy using BBT and lack of research. Therefore, according to these problems, a fuzzy logic system for the predictions of ovulation occurrence, follicular and luteal phase length has been constructed to interpret the BBT data effectively and this system has been implemented on Arduino Mega 2560 microcontroller for portability purpose. As a result, according to six samples of open source BBT data obtained from the Fertility Friend website, the system enables to predict the ovulation occurrence and follicular and luteal phase length with 71.43 % of accuracy.

Keywords: Fuzzy logic, menstrual cycle, basal body temperature.

1. Introduction

Basal body temperature (BBT) has been utilized since thermometers were created to detect the presence of ovulatory cycles. BBT is the lowest body temperature achieve during sleep and usually straight away taken after woke up [1]. Many practitioners have learn on the most proficient method to consolidate BBT in terms of diagnosis and evaluation in the treatment. However, the issues are the absence of research and scientific study approving the viability of using BBT for menstrual cycle.

Menstrual cycle is a series of natural processes that women body goes through. During the period cycle, the hormone levels rise and fall, depending on which stage of the menstrual cycle. These hormones can also affect mood and level of energy. Each woman's cycle has a different number of days due to the lifestyle and environment factors. Normally, the average of menstrual cycle is 28 days long which range from 21 to 35 days in adults and from 21 to 45 days in young teens [2].

This cycle consists of three phases which are follicular phase (FP), ovulation phase (OP), and luteal phase (LP). FP is where the luteinizing hormone (LH) and follicle stimulating hormone (FSH) act on ovaries to stimulate follicle growth. The follicles produce estrogen and progesterone hormone. In this phase, body temperature is at low and steady until at the end of this phase. The estrogen level will rise and reach a point that causes a rapid rise in LH that indicates the follicle is matured and it will release the egg, which is known as the OP. During this phase, the BBT measurement is low and

followed by the rising peak of temperature the day after the ovulation is happen, which is known as biphasic pattern [3]. However, not every women ovulate with increasing of temperature but normally the body temperature will rise after the ovulation happen, which is called a monophasic pattern where the body temperature does not show the rise in body temperature [4]. The maximum period for ovulation phase is only in one day. LP is start when the estrogen level is drastically fall and the egg travels down the Fallopian tube and the process of fertilization or implantation may occur. Here, the temperature is high and steady. This is because progesterone level is high and affected the BBT measurement to be high [2]. However, at the end of the cycle body temperature will drop if there is no pregnancy happen. Monitoring the BBT can identify the change in temperature that occurs before and after ovulation [5].

Previous studies have demonstrated that adjustments in the body temperature reflect the hormonal changes fundamentally in progesterone and estrogen, which could affect the women's health and can make body temperature either increase or decrease. This will reflect the changes in the menstrual cycle, for example the duration of phase and the ovulation process [6]. In order to validate the efficacy of using BBT for menstrual cycle, a system should be developed to interpret the menstrual cycle based on BBT measurement. There are many types of computational intelligent that can do interpretation automatically such as Artificial Neural Networks, Evolutionary Computation, and Fuzzy Logic. In this

research, Fuzzy Logic will be used as a method to develop the menstrual cycle interpretation system.

Fuzzy logic is a logical system, which is an extension of multivalued logic related to the concept of a linguistic variable, canonical form, fuzzy if-then rule, fuzzy quantification, the extension principle, the compositional rule of inference and interpolative reasoning, is not addressed in traditional multivalued logic systems. This is the reason why fuzzy logic has a much wider range of applications than traditional systems. In its wide sense, fuzzy logic is fuzzily synonymous with fuzzy set theory established by Prof. Zadeh in 1965 [7], which is the theory of classes with unsharp boundaries. Fuzzy logic has routinely been shown to outperform classical mathematical and statistical modeling techniques for many applications involving the modeling of real world data. For example, fuzzy logic has found wide acceptance in the field of systems control and medical field.

In the medical area, especially, in oriental medicine, most medical concepts are fuzzy. The imprecise nature of medical concepts and their relationships requires the use of fuzzy logic which can defines inexact medical entities as fuzzy sets and provides a linguistic approach with an excellent approximation to texts. It offer reasoning methods capable of drawing approximate inferences and has been used in medical area to compute and solve complex data or reasons such as medical classification diagnosis, lung cancer, medical image processing and etc. In nearly every one of these applications fuzzy logic in medical system have been shown to outperform the traditional method, yet highly advanced in digital medical reasoning and effectively be a model of a complex real world data that based on a set of historical observations on a time series, serve as the input data to the forecasting method that produces an output of the forecast or future value of the time series of interest. Therefore, in this study, the interpretation system of the BBT data will be developed by using fuzzy logic as data processing to understand the complex data in menstrual cycle towards better healthcare for women.

2. Designing Menstrual Cycle Interpretation System Based on BBT using Fuzzy Logic

The information of menstrual cycle such as day of ovulation (DO), the length of FP and LP are important in the BBT data interpretation [8,9]. Based on the previous research studies [6, 10, 11], they can be obtained using the mathematical formulae as in equation (1) to (3) and the values are summarized according to the type of menstrual cycles as shown in Table 1.

2.1 Menstrual Calculation

This section will explain on how to calculate the DO and the follicular days, FD and the luteal days, LD. The DO is taken from the middle of the last day cycle, LDC of one menstrual cycle as stated in equation (1). As in equation (2), the FD is equal to the DO is minus by one

because the DO occurs in one day only and according to equation (3), the LD is representing by the LDC minus by the DO.

$$DO = \frac{LDC}{2} \quad (1)$$

$$FD = DO - 1 \quad (2)$$

$$LD = LDC - DO \quad (3)$$

DO : Day of ovulation

FD : Follicular days

LD : Luteal days

LDC : Last day cycle

2.2 Menstrual Cycle Table

Table 1 shows the ranges of FD and LD and the range of DO for three types of the woman's menstrual cycle length which are short, medium and long. The range for normal length of FD is between 9 to 11 days, 12 to 15 days and 16 to 21 days for the types of a woman's menstrual cycle in short, medium and long, respectively. Besides, the range for normal length of LD is between 11 to 13 days, 14 to 16 days and 17 to 23 days for the types of a woman's menstrual cycle in short, medium and long, respectively. Therefore, below and above these ranges, the length of FD and LD can be considered as short and long, respectively. Meanwhile, the range of DO is 6 to 14 days, 11 to 18 days and 14 to 24 days for the types of a woman's menstrual cycle in short, medium and long, respectively.

Table 1 The ranges of follicular days, day of ovulation and luteal days based on the type of menstrual cycles.

Type of menstrual cycles	Range of follicular days, FD (days)	Range of day of ovulation, DO (day)	Range of luteal days, LD (days)
SHORT (21 - 25) days	9 - 11	6 - 14	11 - 13
MEDIUM (26 - 32) days	12 - 15	11 - 18	14 - 16
LONG (33 - 45) days	16 - 21	14 - 24	17 - 23

2.3 Fuzzy Logic Development for BBT Data Interpretation

A fuzzy logic development for the BBT data interpretation includes designing block diagrams of the fuzzy logic system using a MATLAB fuzzy logic tool, determining parameter values of membership functions (MFs) and Mamdani rules related to the inputs and outputs and, implementation of the MATLAB fuzzy inference system to the Arduino Mega 2560

microcontroller. Fig. 1 shows the block diagram of the overall fuzzy logic system in this project which consists of three subsystems for the prediction of ovulation day, the FP length and the LP length. There are total of 5 inputs, 3 outputs, 63 MFs of the inputs and outputs and, 53 rules in the fuzzy logic BBT data interpretation system. Starting from the input of BBT data, then it will go through the fuzzy logic in order to be analyzed based on the set of fuzzy rules. Finally, the three fuzzy outputs of the predictions of ovulation, the length of FP and LP will be displayed in the LCD. Here, the MFs of the inputs and outputs are important to determine the rules of for the fuzzy system. Every MF has its own MF parameter value that need to be specified and it was assigned according to the Table 1.

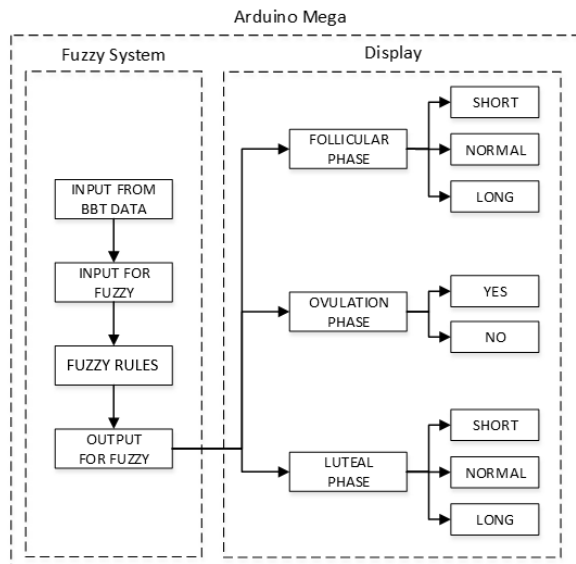


Fig. 1 Block diagram of the fuzzy logic system for BBT data interpretation

Fig. 2 shows the block diagram of the fuzzy ovulation system for the prediction of ovulation starting from three inputs of maximum different temperature between next and previous mean, MaxDiff, menstrual cycle length, MenstrualCL and range of ovulation days, RangeOvulDays, the fuzzy process of ovulation prediction based on 15 Mamdani rules and the output of ovulation prediction, OvuP. There are two MFs in MaxDiff which are less than 0.2 and more than 0.2. MenstrualCL have three MFs which are short, medium, and long. While, RangeOvulDays have six MFs which are less than day 6, day short, day between short and medium, day medium, day long, and more than day 24. Besides, there are two MFs in the output, OvuP which are not ovulate and ovulate.

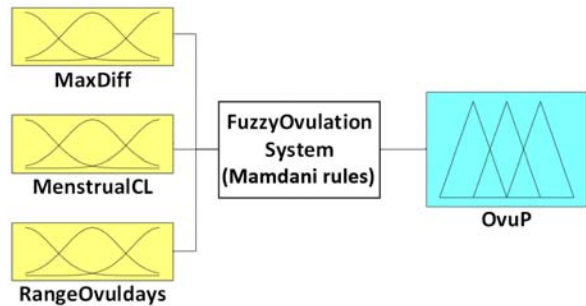


Fig. 2 The fuzzy system for the prediction of ovulation day

Fig. 3 shows the block diagram of the fuzzy system for the prediction of FP length. There are two input blocks; the follicular days, FD and the menstrual cycle length, MenstrualCL and an output of follicular phase length prediction, FPLP. There are 19 MFs in the FD and three MFs in the MenstrualCL which are short, medium, and long. While, for the output FPLP, there are three MFs which are short, normal, and long and the output is obtained based on the 19 Mamdani rules of the fuzzy follicular system with the designated MFs.

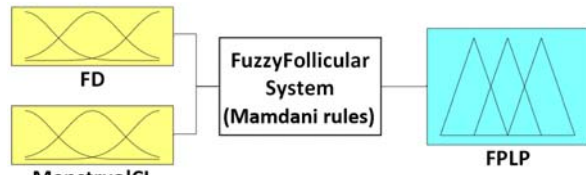


Fig. 3 Fuzzy system for the prediction of FP length

Fig. 4 shows the block diagram of the fuzzy system for the prediction of LP length. There are two input blocks, including the luteal days, LD and the menstrual cycle length, MenstrualCL and an output of luteal phase length prediction, LPLP. There are 19 MFs in the LD and three MFs in the MenstrualCL, which are short, medium, and long. Meanwhile, there are three MF in the output, LPLP which are short, normal, and long. The output is obtained based on the 19 Mamdani rules of the fuzzy luteal system with the designated MFs.

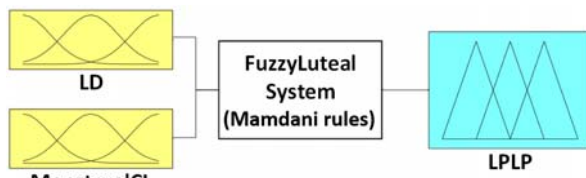


Fig. 4 Fuzzy system for the LP length

3. Results and Discussion

Fig 5 shows the prototype of the fuzzy system for BBT interpretation with a dimension of 15 cm x 6.5 cm x 5.5 cm. Based on seven BBT data (BBT 1 to BBT 7) obtained from Fertility Friend website database, performance of the developed fuzzy system for BBT data interpretation had been evaluated.

Table 2 shows the BBT interpretation results of the DO, the FP length, and LP length prediction from the seven BBT samples tested in the fuzzy system and their actual values obtained from the Fertility Friend website for comparison.

Based on the comparison between the prediction and the actual values, they have shown the same results for the BBT 1 until BBT 5, given that the BBT 1, BBT 2 and BBT 5 have a medium cycle length of 29, 32 and 28 days, respectively. While of, the BBT 3 has 34 days of a long cycle length and the BBT 4 has 22 days (short) of a short cycle length.

Table 2 Confusion matrix for fuzzy ovulation system

Sample of BBT data	Day of Ovulation, DO		Follicular Days, FD		Luteal Day, LD	
	Prediction	Actual	Prediction	Actual	Prediction	Actual
BBT 1	DO = Day-14	DO = Day-14	FD = 13 Days (Normal)	FD = 13 Days (Normal)	LD = 15 Days (Normal)	LD = 15 Days (Normal)
BBT 2	DO = Day-18	DO = Day-18	FD = 17 Days (Long)	FD = 17 Days (Long)	LD = 14 Days (Normal)	LD = 14 Days (Normal)
BBT 3	DO = Day-22	DO = Day-22	FD = 21 Days (Normal)	FD = 21 Days (Normal)	LD = 12 Days (Short)	LD = 12 Days (Short)
BBT 4	DO = Day-8	DO = Day-8	FD = 7 Days (Short)	FD = 7 Days (Short)	LD = 14 Days (Long)	LD = 14 Days (Long)
BBT 5	DO = Day-15	DO = Day-15	FD = 14 Days (Normal)	FD = 14 Days (Normal)	LD = 13 Days (Short)	LD = 13 Days (Short)
BBT 6	DO = NO	DO = Day-13	FD = NO	FD = 12 Days (Normal)	LD = NO	LD = 11 Days (Normal)
BBT 7	DO = Day-18	DO = Day-53	FD = 17 Days (Long)	FD = 52 Days (Long)	LD = 52 Days (Long)	LD = 17 Days (Long)

However, there are differences between the prediction and the actual value for the sample of the BBT 6 and the BBT 7. Here, the BBT 6 has 24 days (short) of a short cycle length and the BBT 7 has 70 days of a long cycle length because of Polycystic Ovary Syndrome, PCOS problem. The interpretation the BBT 6 had shown an inaccurate result of the DO prediction with no ovulation. Thus, the FP and the luteal LP lengths cannot be predicted. While, the actual value of the DO for BBT 6 is at day-13 with the FP and LP lengths are 12 and 11 days. For the results of the BBT 7, the DO occurrence, the FP length and the LP length were incorrectly predicted as day-18, 17 days (long), and 52 (long), respectively. While, the actual value of the DO, the FP length and the LP length are day-53, 52 days (long), and 17 (long), respectively.

The incorrect interpretation of the BBT 6 and the BBT 7 is generally caused from an imperfect designation of the fuzzy rules in tracking the ovulation day since the ovulation occurrence has been predicted as positive only by a single rule which is when a maximum different between two adjacent temperatures is higher than 0.2°C . Based on the BBT 6, the maximum temperature difference is only 0.15°C , thus the ovulation occurrence had been inaccurately predicted as negative. Meanwhile, for the BBT 7, the system had incorrectly predicted the DO earlier at day-18 since the temperature difference with more than 0.2°C is happened two time; at day-18

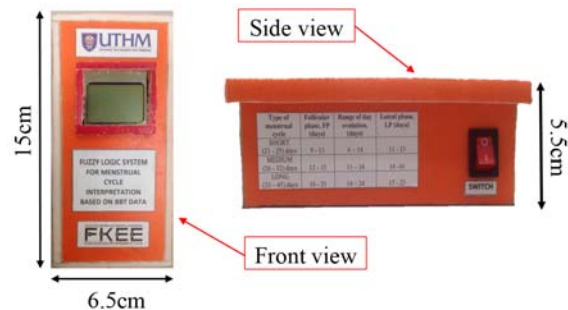


Fig. 5 Dimension of the BBT interpretation prototype

and day-53. Thus, based on only the single rule, the correct ovulation day which is at day-53 was cannot be predicted. Table 3 shows the confusion matrix for an accuracy performance evaluation of the fuzzy ovulation system with the total number of seven tested data, n . The tested data are based on the actual positive BBT 1 to the BBT 7, where the case when the day of the ovulation occurrence was correctly predicted is labeled as positive and vice versa. Here, true positive, TP is determined by the number of accurate predicted positive data and false positive, FP is determined by the number of inaccurate predicted positive data. Meanwhile, true negative, TN is determined by the number of accurate predicted negative data and false negative, FN is determined by the number of the inaccurate predicted negative data [11].

As shown in Table 3, the fuzzy system had successfully predicted five data as TP, while the other two were predicted as FN. Moreover, zero data had been predicted as TN and FP, since there was no actual negative data tested. According to equation (4), the fuzzy system achieved 71.43 % accuracy in predicting the ovulation occurrence with a correct ovulation day.

Table 3 Confusion matrix for fuzzy ovulation system

$n = 7$	Predicted : Positive	Predicted : Negative	
Actual : Positive	TP = 5	FN = 2	7
Actual : Negative	FP = 0	TN = 0	0
	5	2	

$$\text{Accuracy} = \frac{\text{TP} + \text{TN}}{\text{TOTAL}} \times 100\% \quad (4)$$

TP : True positives
 TN : True negatives
 FP : False positives
 FN : False negatives

4. Conclusion

As a conclusion, the development of the fuzzy system for BBT data interpretation had been done towards helping women to interpret their menstrual cycle easily in a portable manner by implementing it on a microcontroller based system using Arduino Mega 2560. The accuracy of the fuzzy system was optimally achieved at 71.43% in interpreting the BBT data for the ovulation day with the FP and LP lengths. Therefore, this system could help women to understand better their menstrual cycles in order to improve and raise awareness on their unique women's health. However, this project needs to be improved in terms of the rules and MF parameter values to increase the system accuracy [12]. Besides, it should be utilized with the internet of things (IoT) and integrated with a temperature measurement system to make better use of this project.

5. Acknowledgement

The authors would like to thank MiNT-SRC, UTHM for providing research facilities especially in Cardiology and Physiome Analysis (CaPA) Research Laboratory in conducting this project work.

References

- [1] J. E. Bauman, "Basal Body Temperature: Unreliable Method of Ovulation Detection,"

- Fertil. Steril.*, vol. 36, no. 6, pp. 729–733, 1981.
 [2] M. D. I. Lawrence M. Nelson, "Menstruation and the Menstrual Cycle," vol. 1, no. 1, p. 6, 2009.
 [3] M. L. Barron, R. Fehring, B. Mary, L. Barron, and R. J. Fehring, "Basal Body Temperature Assessment : Is It Useful to Couples Seeking Pregnancy ?," vol. 30, no. 5, pp. 290–296, 2005.
 [4] O. M. Degree, "Basal Body Temperature (BBT) as an Indicator for Traditional Chinese Medicine (TCM) Diagnosis and Evaluation in W omen 's Reproductive Health," no. April, 2015.
 [5] A. M. Rosliza, and et. al, "Ensuring human rights in the provision of contraceptive information and services - Guidance and recommendations," *2014 IEEE 38th Int. Comput. Softw. Appl. Conf. Work.*, vol. 0, no. 2, SI, pp. 95–101, 2011.
 [6] Y. Liu, E. B. Gold, B. L. Lasley, and W. O. Johnson, "Factors affecting menstrual cycle characteristics," *Am. J. Epidemiol.*, vol. 160, no. 2, pp. 131–140, 2004.
 [7] Lotfi Aliasker Zadeh, "Biological application of the theory of fuzzy sets and sytems," *Process International Symposium Biocybernetics of the Central Nervous System*. Boston, pp. 199–212, 1969.
 [8] Yazed MSM, Mahmud F, and Morsin M, "Fuzzy logic system for bbt based fertility prediction," *J. Fundam. Appl. Sci.*, vol. 9, no. 4S, pp. 475–491, 2017.
 [9] M. Maksimovic, V. Vujovic, B. Perisic, and V. Milosevic, "Developing a fuzzy logic based system for monitoring and early detection of residential fire based on thermistor sensors," *Comput. Sci. Inf. Syst.*, vol. 12, no. 1, pp. 63–89, 2015.
 [10] V. D. L. M. K. Buckingham, C. Farquhar, K. Jam, and M. Metwally, "Luteal phase support for assisted reproduction cycles (Review)," no. 7, 2016.
 [11] L. A. Winters-miner and et. al, "Guidelines to Charting Your Fertility Cycle," *Fertil. Educ. Train.*, vol. 1, no. 1, pp. 1–3, Aug. 2015.
 [12] O. Cordon and F. Herrera, "A proposal for improving the accuracy of linguistic modeling," *IEEE Trans. Fuzzy Syst.*, vol. 8, no. 3, pp. 335–344, 2000.

SHORT REVIEW ON TECHNIQUES AND MATERIALS USED FOR MICROFLUIDIC DEVICE FABRICATION

Sargunan Sundra¹, Chin Phong Soon^{1,*}, Farhanahani Mahmud², Nurfarina Zainal², Kian Sek Tee²

¹Biosensor and Bioengineering Laboratory, MiNT-SRC, Faculty of Electrical and Electronic Engineering, Universiti Tun Hussein Onn Malaysia, 86400 Parit Raja, Batu Pahat, Johor, Malaysia.

²Faculty of Electrical and Electronic Engineering, Universiti Tun Hussein Onn Malaysia, 86400 Parit Raja, Batu Pahat, Johor, Malaysia.

Abstract: Microfabricated devices have revolutionized human ability to control small volumes of fluids and micro-particles contained therein. This has led to countless potential in current technologies that require a fast response, small volume of liquid handling, low costs and automation. Different methods have been implemented to make a microfluidic chip which made up of different materials. Different techniques of microfluidic fabrication evolved over time to make the fabrication process economical, easy and fast. The first part of this short review provides general view regarding the techniques used to fabricate microfluidic devices. The second part introduces polymer materials typically employed for microfluidic development. Besides that, the paper also reviews specifically on usage of poly(dimethylsiloxane) (PDMS) as material used in microfluidic fabrication process. Last part of the paper concluded with advantages of microfluidic application in biological and chemical studies and future direction of microfluidic.

Keywords: Microfluidics, fabrication, material, lab-on-chip, microfluidic techniques, microfluidic materials

1. Introduction

Microfluidics defined as the science and technology of manipulating fluids in microchannels with size of dimensions between approximately 5-500 μm [1]. Microfluidic systems applied to convey volumes of fluid that ranges from microliters to femtoliters in microchannels which are commonly embossed in the surface of polymer and glass. Microfluidics has several characteristics that drastically increase its application in biology, chemistry, engineering and medicine fields. Features such as low consumption of reagents and samples, short reaction and analysis time, economical and reduced dimensions compared to other devices led to endless potential in current analytical technologies [2].

The fabrication of microsystems began in 1968, focusing in semiconductor devices like diodes, transistors, integrated circuits, and complex electronic components which profited communication and information technologies significantly. Silicon was and still a widely used material in semiconductor industries due to its excellent mechanical properties. It is further applied to build up 3D micromechanical systems. Many different fabrication techniques such as deposition, etching, second cast, bonding and mask-less patterning techniques are used to micromachine materials like polymers, silicon, glass and metals. However, photolithography is still the key fabrication process to design microstructures which are transferred by ultraviolet exposure and development. The aim of this short review is to explain the techniques and materials used in the process of fabrication of microfluidic devices.

Besides that, justification for PDMS as chosen material in microfluidic fabrication is also included in this paper.

2. Techniques for Microfluidic Fabrication

Techniques that normally used to develop microfluidic devices namely wet and dry etching, thermoforming, polymer ablation, polymer casting, and soft-lithography. Over period of time, these techniques have been improved in order to make it more economical and less cumbersome. Nonetheless can also produce a customised microfluidic chips in short period of time. However, photolithography is the key process to produce the master mold of a microfluidic device.

2.1 Wet and dry etching

Etching is a process removal of unwanted material by using etchant such as liquid chemicals (wet process) and/or gases (dry process). In wet etching process, the unwanted parts of the materials are removed using selected etchants. The etching area can produce an isotropic pattern. In case of using positive resist, material is etched in all directions except covered masked area and this leads to an extension of the microchannels. The liquid etchants etch the materials at different rates. It is depending on the type and thickness of the material [3]. Meanwhile in dry etching, plasmas or etchant gases were used to remove the unwanted parts of the material leaving behind the microchannels. The ablation reaction can be physical, chemical or hybridization of both. In physical ablation reaction, high kinetic energy is required which is emitted by a beam of ion, electron or photon. There is no

chemical reaction takes place and the particle energy emitted from ions, electron or photon bombard the atoms out from the surface[4]. In chemical dry etching, gas molecules is used to react with the surface and remove the atoms of materials from the surface [5]. Reactive ion etching (RIE) is a combination of both physical and chemical reaction which employ high energy collision from ionization to dissociate the etchant molecules into more reactive species [6].

2.2 Thermoforming

Thermoforming refers to thermoplastic deformation process to form a partially-finished polymer sheets into a 3D shaped [7]. In thermoforming, a material is heated to shape them into the desired form. It is commonly used for many plastic products and aided by injection molding or hot embossing. The injection molding introduces thermoplastics pellet into a heated mold to create a microfluidic chip. This technique allows a high quantity fabrication once the parameters have been optimized. However, the cost of equipment and mold are expensive which make this method not commonly used in the laboratory. Hot embossing is a method that involved pressing of heated silicon or metal towards a thermoplastic sheet such as poly-(methyl methacrylate) (PMMA) and cyclic olefin copolymer (COC) [8, 9].

2.3 Polymer ablation

Polymer ablation is a process where microstructures are formed using direct cutting or patterning processes such as mechanical drilling, sawing, and laser micromachining. Although this technique is able to fabricate microfluidic device in short period of time and able to produce 3D structured microfluidic device (laser micromachining)[10, 11], but the resolution of the micropatterning is limited and it is possible that the shape of the microchannels are distorted due to inhomogenous mechanical ablation of the material which causes defective of the microfluidic device [10, 11].

2.4 Polymer casting

Polymer casting is a different method for fabrication of a microfluidic device. In this method, the main aim is to create a mold and use a polymer to replicate the micropatterns into microchannels. In PDMS microfluidic device, the microchannels mainly fabricated using a simple soft lithography process in which the PDMS reagent is casted on the master mold and followed by bonding process [12, 13]. Casting process is a simple process and the layer is easily released from the master mold and this results in reliable and high yield process. A PDMS casted and cured layer can be directly sealed or adhered to another PDMS or glass substrates by Van der Waals forces [14]. In order to secure high bonding strength, oxygen plasma treatment can be carried out to form an O-Si-O covalent bond at the PDMS-glass interface [15, 16].

2.5 Soft-Lithography

Soft-lithography is a replicating method which used to produce master micromould (mostly made from elastomeric materials) which serve as a pattern transfer agent. These master micromoulds can be made from a variety of materials but SU-8 photoresists are the most common material used. In the photolithography process, the micropatterns are made by curing the masked area while exposing the unmasked area of the photoresist to ultraviolet lights. The etchant removes the UV exposed area of photoresists leaving behind the micropatterns of photoresists. This serve as the micromould for the soft lithography. To fabricate the PDMS micropattern via soft lithography, the siloxane oligomer and the curing agent are mixed thoroughly at ratio 10:1 and degassed in vacuum chamber. Then, the PDMS pre-polymer is poured on the master micromould to replicate the shape of the master template and shape according to the features. Cross-linking of PDMS (polymerisation) can occur at room temperature (25 °C) but also can be fastened by baking it at 70 °C for 60 minutes. Later, the PDMS can be peeled off and bonded to form closed channels [17, 18]. Figure 1 show the comparison of microfluidics fabrication processes between photolithography and soft lithography.

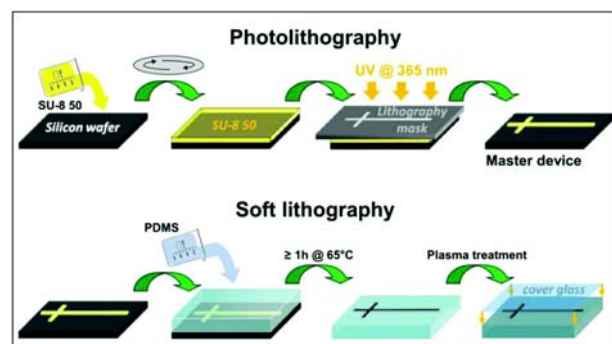


Fig. 1 Photolithography and soft lithography for microfluidics fabrication[19]

3. Polymer for Microfluidics Fabrication

Polymeric materials typically used in microfluidic development can be categorised into two major types namely as polydimethylsiloxane (PDMS) and thermoplastics. PDMS is one of the common materials used in fabricating microfluidics due to its elasticity, gas permeability, and several unique characteristics. PDMS is an elastomer-based material that is able to be deformed by applying force or air pressure. Although both PDMS and thermoplastics have shown high biocompatibility for biomolecules and cells application [20, 21]. Due to the gas permeability and high optical transmissivity, PDMS is the major material choice for cellular application microfluidic device [2, 22, 23]. Thermoplastics are synthetic polymers that show various properties such as mechanical appearance, thermal, solvent resistance and

biocompatibility that enable them to be applied in microfluidic application. Thermoplastics such as poly (methyl methacrylate) (PMMA), polycarbonate (PC), polystyrene (PS), polyvinyl chloride (PVC), polyimide (PI) and family of cyclic olefin polymers have been widely established in microfluidics [24-26]. Thermoplastics are rigid polymer material that have good mechanical strength, low water absorption, and acid/base resistivity. Table 1 shows the physical properties of polymers used in microfluidic fabrication.

Table 1 Summary of physical properties of common polymer used in microfluidic fabrication [27]

Polymer	PDMS	Thermoplastics			
		PC	PMM A	PS	Cyclic olefin
Mechanical	Elastomer	Rigid	Rigid	Rigid	Rigid
Thermal	~80 °C	140~150 °C	100~125 °C	90~100 °C	70~15 5 °C
Solvent resistance	Poor	Good	Good	Poor	Excellent
Acid/Base resistance	Poor	Good	Good	Good	Good
Optical transmissivity (Visible range)	Excellent	Excellent	Excellent	Excellent	Excellent
Biocompatibility	Good	Good	Good	Good	Good

4. Advantage and Disadvantage of PDMS in Microfluidic Fabrication

Most research activities in the field of microfluidic systems employ poly(dimethylsiloxane) (PDMS) which has distinctive characteristics compared to silicon [28]. Presence of siloxane backbone and methyl groups to silicon gives PDMS its unique properties. In chemistry, the empirical formula for PDMS is written as $\text{CH}_3[\text{Si}(\text{CH}_3)_2\text{O}]_n\text{Si}(\text{CH}_3)_3$ and its belong to the silicones group [29]. PDMS is a soft, flexible, chemically stable, non-hydroscopic, electrically insulating, inert, transparent to visible and ultraviolet light, permeable to gases, and moderately permeable to water [27, 30]. Due to its special properties to design microchannels of the microfluidic devices, it is suitable to be used in aqueous systems of biochemical and cells [18, 31]. PDMS has surface that can be easily oxidized to present Si-(OH) groups which characterize the hydrophilic property of PDMS. Thus, this enable the treated PDMS surface to seal with other polymer and glass without using adhesives [32]. The main disadvantages of PDMS for microfluidics fabrication are the absorbance of organic solvents and compounds such as alkyl and aryl amines and the surface properties are difficult to be control [33]. Recent study by

Rolland *et al.* shows that cross-linked perfluoropolyether elastomers (Teflon) have similarities with PDMS in aspect of physical properties but does not absorb organic solvents. However, sealing this polymer with other materials is challenging compared to PDMS sealed by using oxidative route [34]. Besides that, PDMS shrinks about 1.00 % during the curing process and soft texture limits the formation of microstructures in PDMS. A study by Toepke *et al.* has shown another unique characteristic of PDMS made microfluidic which has the ability to absorb drugs, proteins and small hydrophobic molecules [35]. Table 2 summarise the advantages and disadvantages of using PDMS.

Table 2 Advantages and disadvantages of using PDMS in microfluidic fabrication process

Advantages	Soft, flexible, chemically stable, electrically insulating, biocompatible, gaseous permeable, moderately permeable to water.	[27, 28, 30], [18, 31]
Disadvantages	absorbs organic solvents and compounds, shrinks during polymerisation, and ability to absorb drugs, proteins and small hydrophobic molecules.	[33], [34], [35]

5. Microfluidic based Packaging for CMOS – based Lab on Chip

Microfluidic plays a very important role in packaging CMOS – based lab on chip as it enables to deliver cells and fluids in a well-controlled manner between different on chip system. Even though, the flow of fluids and cells above the chip can be either passive or active, passive flow mechanism have been well establish compared to active flow [36, 37]. This is due to sophisticated applications such highly parallel arrays of reactors. Technique of microfluidic packaging such as flip-chip, enable microfluidic packages fabricated from a variety of materials such as silicon, glass, metals, ceramics, hard plastics and elastomers [38]. Integration of photolithography, microfluidic, CMOS and micromachining technology provide the opportunities for application of MEMS in implantable biomedical device. As a study reported in [39], low capacitive pressure sensor based on CMOS was developed with reduced size of the system, low cost and improved performance which is applicable as contact lens integrated with pressure sensor to measure the pressure in the eyes for glaucoma analysis.

6. Conclusion and Future Direction

It is clear that microfluidics has advantages of consuming small volume of fluids and reagents, reduces waste, and requires small number of cells for chemical studies in biological systems. The applications of soft lithography technique enable biologists and biochemists to prototype microfluidic structure rapidly and eliminate most of the difficult steps in fabricating microfluidic systems. Hence, application of microfluidic widens the possibilities of new technology in biological sciences and enhance the performance of bioanalytical process and reduce cost. The future of microfluidic applications provides new opportunities and wide range of interest in research field. Several new approaches in learning such as interfacing microfluidic device with microelectronic devices, enable to run large number of experiments in parallel for biochemical and cell biology, and specific types of biochemical synthesis. Microfluidics has much to offer in chemistry and biological field and able to broaden our understanding of biological interactions and may have applications in other area of science.

Acknowledgements

This study is financially supported by Ministry of Higher Education Malaysia under the contract no UTHM U567.

References

- [1] G. M. Whitesides, "The origins and the future of microfluidics," *Nature*, vol. 442, pp. 368-373, 2006.
- [2] M.-H. Wu, S.-B. Huang, and G.-B. Lee, "Microfluidic cell culture systems for drug research," *Lab on a Chip*, vol. 10, pp. 939-956, 2010.
- [3] A. Grosse, M. Grewe, and H. Fouckhardt, "Deep wet etching of fused silica glass for hollow capillary optical leaky waveguides in microfluidic devices," *Journal of micromechanics and microengineering*, vol. 11, p. 257, 2001.
- [4] E. A. Waddell, "Laser ablation as a fabrication technique for microfluidic devices," *Methods Mol Biol*, vol. 321, pp. 27-38, 2006.
- [5] J. Garra, T. Long, J. Currie, T. Schneider, R. White, and M. Paranjape, "Dry etching of polydimethylsiloxane for microfluidic systems," *Journal of Vacuum Science & Technology A: Vacuum, Surfaces, and Films*, vol. 20, pp. 975-982, 2002.
- [6] J. C. McDonald and G. M. Whitesides, "Poly(dimethylsiloxane) as a material for fabricating microfluidic devices," *Accounts of chemical research*, vol. 35, pp. 491-499, 2002.
- [7] R. Truckenmüller, Z. Rummler, S. Th, and W. K. Schomburg, "Low-cost thermoforming of micro fluidic analysis chips," *Journal of Micromechanics and Microengineering*, vol. 12, p. 375, 2002.
- [8] R. Truckenmüller, S. Giselbrecht, N. Rivron, E. Gottwald, V. Saile, A. van den Berg, *et al.*, "Thermoforming of Film-Based Biomedical Microdevices," *Advanced Materials*, vol. 23, pp. 1311-1329, 2011.
- [9] A. Disch, C. Mueller, and H. Reinecke, "Low Cost Production of Disposable Microfluidics by Blister Packaging Technology," in *2007 29th Annual International Conference of the IEEE Engineering in Medicine and Biology Society*, 2007, pp. 6322-6325.
- [10] E. A. Waddell, "Laser ablation as a fabrication technique for microfluidic devices," *Microfluidic Techniques: Reviews and Protocols*, pp. 27-38, 2006.
- [11] J. Kim and X. Xu, "Excimer laser fabrication of polymer microfluidic devices," *Journal of Laser Applications*, vol. 15, pp. 255-260, 2003.
- [12] Y. Xia, J. A. Rogers, K. E. Paul, and G. M. Whitesides, "Unconventional methods for fabricating and patterning nanostructures," *Chemical reviews*, vol. 99, pp. 1823-1848, 1999.
- [13] M. A. Eddings, M. A. Johnson, and B. K. Gale, "Determining the optimal PDMS-PDMS bonding technique for microfluidic devices," *Journal of Micromechanics and Microengineering*, vol. 18, p. 067001, 2008.
- [14] J. Wang, S. Wang, P. Zhang, and Y. Li, "Easy-disassembly bonding of PDMS used for leak-tight encapsulation of microfluidic devices," in *2017 18th International Conference on Electronic Packaging Technology (ICEPT)*, 2017, pp. 1051-1055.
- [15] Z. Z. Chong, S. B. Tor, N. H. Loh, T. N. Wong, A. M. Gañán-Calvo, S. H. Tan, *et al.*, "Acoustofluidic control of bubble size in microfluidic flow-focusing configuration," *Lab on a Chip*, vol. 15, pp. 996-999, 2015.
- [16] S. H. Tan, N.-T. Nguyen, Y. C. Chua, and T. G. Kang, "Oxygen plasma treatment for reducing hydrophobicity of a sealed polydimethylsiloxane microchannel," *Biomicrofluidics*, vol. 4, p. 032204, 2010.
- [17] J. P. Urbanski, W. Thies, C. Rhodes, S. Amarasinghe, and T. Thorsen, "Digital microfluidics using soft lithography," *Lab on a Chip*, vol. 6, pp. 96-104, 2006.
- [18] G. M. Whitesides, E. Ostuni, S. Takayama, X. Jiang, and D. E. Ingber, "Soft lithography in biology and biochemistry," *Annual review of biomedical engineering*, vol. 3, pp. 335-373, 2001.
- [19] M. Elitas, M. Yuce, and H. Budak, "Microfabricated tools for quantitative plant biology," *Analyst*, vol. 142, pp. 835-848, 2017.

- [20] A. Alrifaiy, O. A. Lindahl, and K. Ramser, "Polymer-based microfluidic devices for pharmacy, biology and tissue engineering," *Polymers*, vol. 4, pp. 1349-1398, 2012.
- [21] P. M. van Midwoud, A. Janse, M. T. Merema, G. M. Groothuis, and E. Verpoorte, "Comparison of biocompatibility and adsorption properties of different plastics for advanced microfluidic cell and tissue culture models," *Analytical chemistry*, vol. 84, pp. 3938-3944, 2012.
- [22] S. K. Sia and G. M. Whitesides, "Microfluidic devices fabricated in poly (dimethylsiloxane) for biological studies," *Electrophoresis*, vol. 24, pp. 3563-3576, 2003.
- [23] M. Mehling and S. Tay, "Microfluidic cell culture," *Current opinion in Biotechnology*, vol. 25, pp. 95-102, 2014.
- [24] K. Liu and Z. H. Fan, "Thermoplastic microfluidic devices and their applications in protein and DNA analysis," *Analyst*, vol. 136, pp. 1288-1297, 2011.
- [25] M. Nevitt, "Selecting and designing with the right thermoplastic polymer for your microfluidic chip: a close look into cyclo-olefin polymer," in *Proc. SPIE*, 2013, p. 86150F.
- [26] A. Bhattacharyya and C. M. Klapperich, "Thermoplastic microfluidic device for on-chip purification of nucleic acids for disposable diagnostics," *Analytical Chemistry*, vol. 78, pp. 788-792, 2006.
- [27] R. O. Rodrigues, R. Lima, H. T. Gomes, and A. M. Silva, "Polymer microfluidic devices: an overview of fabrication methods," *U. Porto Journal of Engineering*, vol. 1, pp. 67-79, 2015.
- [28] A. D. Stroock and G. M. Whitesides, "Components for integrated poly (dimethylsiloxane) microfluidic systems," *Electrophoresis*, vol. 23, pp. 3461-3473, 2002.
- [29] A. Mata, A. J. Fleischman, and S. Roy, "Characterization of polydimethylsiloxane (PDMS) properties for biomedical micro/nanosystems," *Biomed Microdevices*, vol. 7, pp. 281-93, Dec 2005.
- [30] F.-Q. Nie, M. Yamada, J. Kobayashi, M. Yamato, A. Kikuchi, and T. Okano, "On-chip cell migration assay using microfluidic channels," *Biomaterials*, vol. 28, pp. 4017-4022, 2007.
- [31] K. Tsougeni, A. Tserepi, and E. Gogolides, "Photosensitive poly (dimethylsiloxane) materials for microfluidic applications," *Microelectronic engineering*, vol. 84, pp. 1104-1108, 2007.
- [32] N. Lucas, S. Demming, A. Jordan, P. Sichler, and S. Büttgenbach, "An improved method for double-sided moulding of PDMS," *Journal of Micromechanics and Microengineering*, vol. 18, p. 075037, 2008.
- [33] J. N. Lee, C. Park, and G. M. Whitesides, "Solvent compatibility of poly (dimethylsiloxane)-based microfluidic devices," *Analytical chemistry*, vol. 75, pp. 6544-6554, 2003.
- [34] J. P. Rolland, R. M. Van Dam, D. A. Schorzman, S. R. Quake, and J. M. DeSimone, "Solvent-resistant photocurable "liquid teflon" for microfluidic device fabrication," *Journal of the american chemical society*, vol. 126, pp. 2322-2323, 2004.
- [35] M. W. Toepke and D. J. Beebe, "PDMS absorption of small molecules and consequences in microfluidic applications," *Lab Chip*, vol. 6, pp. 1484-6, Dec 2006.
- [36] C. N. Jones, J. Dalli, L. Dimisko, E. Wong, C. N. Serhan, and D. Irimia, "Microfluidic chambers for monitoring leukocyte trafficking and humanized nano-proresolving medicines interactions," *Proceedings of the National Academy of Sciences*, vol. 109, pp. 20560-20565, 2012.
- [37] T. Voitsekivska, E. Suthau, and K.-J. Wolter, "CMOS multiplexer for portable biosensing system with integrated microfluidic interface," in *Electronic Components and Technology Conference (ECTC), 2014 IEEE 64th*, 2014, pp. 173-178.
- [38] J. B. Christen and A. G. Andreou, "Design, fabrication, and testing of a hybrid CMOS/PDMS microsystem for cell culture and incubation," *IEEE Transactions on Biomedical Circuits and Systems*, vol. 1, pp. 3-18, 2007.
- [39] B. yEOP MajLiS, "MEMS very low capacitive pressure sensor based on CMOS process," *Sains Malaysiana*, vol. 40, pp. 259-266, 2011.

EFFECTS OF WITHDRAWAL SPEED ON THE STRUCTURAL AND ELECTRICAL PROPERTIES OF TiO₂ THIN FILMS

Anis Suhaili Bakri¹, Mohd Zainizan Sahdan^{2,*}, Siti Ashraf Abdullah¹, Nur Amaliyana Raship¹, Sawsan Abdullah Abduljabbar¹, Yunus Sari³

¹Faculty of Electrical and Electronic Engineering, Universiti Tun Hussein Onn Malaysia (UTHM), 86400 Parit Raja, Batu Pahat, Johor, Malaysia

²Microelectronic and Nanotechnology-Shamsuddin Research Centre (Mint-SRC), Universiti Tun Hussein Onn Malaysia (UTHM), 86400 Parit Raja, Batu Pahat, Johor, Malaysia

³Preston Shipyard Sdn Bhd Km9, Jalan Ranca Ranca, P.O Box 82164, 87031, Wilayah Persekutuan Labuan

Abstract: Nanocrystalline titanium dioxide (TiO₂) of anatase phase tetragonal lattice structure was successfully prepared on silicon substrate using sol-gel dip coating technique. The effects of withdrawal speed on the crystalline structure, morphology and electrical properties of the TiO₂ thin films were investigated using x-ray diffraction (XRD), atomic force microscope (AFM) and four point probe. It was found that, the withdrawal speed significantly affects the structural, surface morphological and electrical properties of the TiO₂ thin films. XRD analysis confirmed that the films are polycrystalline in nature having anatase tetragonal lattice structure with preferred orientation along (101) plane. The surface roughness (RMS) of the films estimated from AFM measurement increases from 0.371 to 0.739 nm, when withdrawal speed increased from 10 to 200 mm/min, respectively. The resistivity of the films were found to be increases with increasing withdrawal speed.

Keywords: Dip coating, thin films, x-ray diffraction, atomic force microscope, four point probe

1. Introduction

Titanium dioxide also known as titania is an n-type semiconductor with high energy bandgap. Its energy band gap is depends on its crystalline phase [1]. It is widely known that TiO₂ has three different crystalline phase which are brookite, anatase and rutile [2]. Anatase and rutile have tetragonal lattice structure with energy bandgap of 3.30 eV and 3.05 eV, respectively [3]. While brookite has orthorhombic structure and is the least investigated crystalline phase for the TiO₂ films [4]. TiO₂ can be fabricated using several techniques such as sputtering, spin coating, hydrothermal, chemical bath deposition, chemical vapor deposition and more recently it has been fabricated using supersonic plasma jet deposition [5]. Each method produces different nanostructures such as nanotubes, nanorods and nanoflowers. Among these techniques, sol-gel method is one of the versatile methods due to its simplicity, low temperature, ease of composition control and low cost equipment [6]. Moreover, for the TiO₂ films, we can control its crystalline phase using this technique. Due to its attractive features, TiO₂ has been widely investigated for several applications such as dye sensitized solar cells, gas sensor, photocatalytic water purification and hydrogen generation by water splitting [7].

The study of growth mechanism of TiO₂ thin films prepared using sol-gel dip coating is very important to produce good properties of films. In this paper, the influence of the withdrawal speed on the structural,

morphological and electrical properties of the deposited TiO₂ thin films will be discussed in detail.

2. Experimental procedure

In this study, the TiO₂ thin films were deposited on silicon substrates using sol-gel dip coating technique. The experimental details contained four parts.

2.1 Materials and solution preparation

Nanocrystalline TiO₂ thin films were prepared using sol-gel dip coating method on n-type silicon (100) substrate. For the synthesis of the TiO₂ solution, the chemical used were titanium (IV) butoxide, glacial acetic acid, ethanol, triton x-100, and hydrochloric acid as precursor, chelating agent (stabilizer), solvent, surfactant, and catalyst, respectively. Titanium (IV) butoxide (0.34 M) was firstly dissolved in ethanol. After that, the glacial acetic acid and the diluted hydrochloric acid with molar ratio to deionized water (1:1) were added into the solution and then 1 drop of triton x-100 was added into the solution. The TiO₂ solutions were stirred at 40 °C for 10 minutes and continuously stirrer for the next 2 hours at room temperature to yield a clear and homogenous solution, which served as the coating solution.

2.2 Substrate preparation

Before performing the dip coating technique, silicon substrates were ultrasonically cleaned in acetone and ethanol for 10 minutes, both. To remove the native oxide on the surface of the silicon substrate, it was then dipped for a short time (~ 1 minutes) in a diluted hydrofluoric acid (HF) and thoroughly rinsed with deionized water. The change of wetting characteristics of the initially hydrophilic to hydrophobic surface, can visually indicate when the surface is clean from oxide. This is because the characteristic of oxide is hydrophilic whereas pure silicon is hydrophobic. Finally, they were purged with nitrogen (N_2) gas to dry. The N_2 gas was used to dry the silicon substrate instead by allowing the water to evaporate itself due to the evaporation of the water may leave the residues on the substrate.

2.3 Deposition of nanocrystalline TiO_2 thin film

The silicon substrate was immediately used after it was cleaned to avoid the re-growth of the native oxide. The TiO_2 films were deposited using dip coater machine (PTL-MM01-Desktop dip coater) (Fig. 1) with different withdrawal speed of 10, 100, and 200 mm/min. After single deposition layer, all films were preheated at 100 °C for 5 minutes on a hot plate to completely evaporate the solvent and organic residuals. The resulting thin films were then annealed at 400 °C for 1 hour in an electrical furnace.

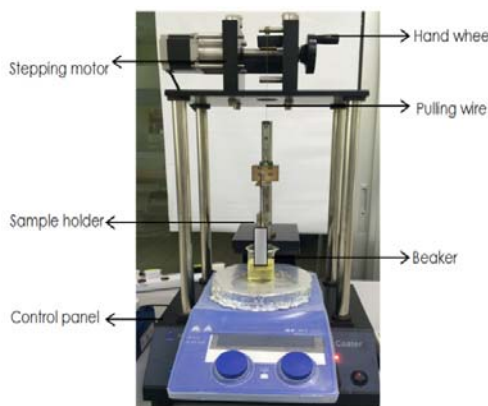


Fig. 1 Deposition of TiO_2 thin film using dip coating

2.4 Characterization of nanocrystalline TiO_2 thin films

The crystal phase of the prepared thin films were determined using the X-ray diffraction (XRD, Panalytical X'Pert³ powder) utilizing $CuK\alpha$ radiation source ($\lambda=0.15406$ nm) at a setting operated of 40 mA and 40 kV. The step size of 2θ degree angle was 0.03 and the scan step time was 0.5 s at a divergent slit of 1/2°. The surface morphologies of the thin films were studied using atomic force microscope (AFM, Park System XE-100) and measurement were taken in non-contact mode with the scan size of the films taken in 1 μm x 1 μm. The

average grain size and the root mean square (RMS,Rq) roughness values were obtained using XEI image processing software. The thickness of the deposited films were determined using a surface profiler (Alpha step IQ) with scan length 5000 μm and scan speed of 50 μm. the electrical properties of the films were studied using four point probe measurement (Lucas Signatone : Pro 4 G-100 integrated with Keithley 2400 series source meter).

3. Results and Discussion

The film thickness of the TiO_2 thin films can be controlled using the withdrawal speed of dip coating. The relation between the film thickness and the withdrawal speed is shown in Fig. 2. From the experiment, it is found that the thickness of the TiO_2 thin films is directly proportional to the withdrawal speed of dip coating. This result agree well with Landau-Levich equation [8], and is given by,

$$h = 0.94 \frac{(\eta \cdot v)^{2/3}}{\gamma^{1/6} (\rho \cdot g)^{1/2}} \quad (1)$$

where h represents film thickness, η is the withdrawal speed of dip coating, v is solution viscosity, γ is solution vapor surface tension, ρ is solution density and g is gravitational acceleration. Higher withdrawal speed will cause higher evaporation rate and acceleration of the gelation process. The coating thickness increases as the withdrawal speed increased due to increase in upward viscous drag on the liquid by the moving silicon substrate [9]. Furthermore, more coating solution is pulled up on the substrate surface because there is no time for the solution to flow down back to the beaker.

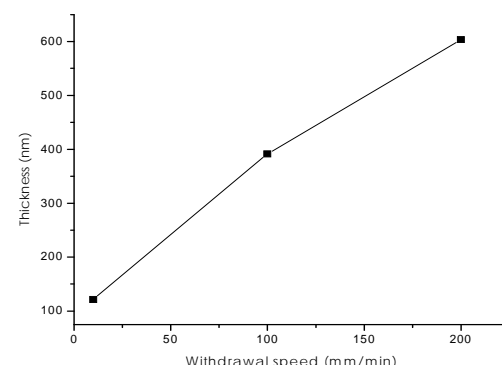


Fig. 2 Variation of thickness at various withdrawal speed

Fig. 3 shows the diffraction patterns of the dip coated TiO_2 films fabricated at different withdrawal speed ranging from 10-200 mm/min. The XRD patterns were observed at 2θ degree angle from 20° to 65°. From the XRD measurement, it is clearly observed that all films exhibit TiO_2 anatase peak with tetragonal lattice structure. The highest peaks was observed at 25° which reflects to (101) plane. Therefore, the TiO_2 thin films was (101) plane preferential growth. There are another six planes

observed at 2θ of 37.8, 48.0, 54.0, 55.2 and 62.7 corresponding to the crystal planes of (004), (200), (105), (211) and (204), respectively. All peaks present match well with Bragg reflection of the standard anatase nanocrystalline structure inorganic crystal structure database (ICSD) file no. 98-015-4604 with approximately correct integrated intensity proportions. The peak present at 52.4° belongs to silicon substrate with ICSD file no 98-004-1991.

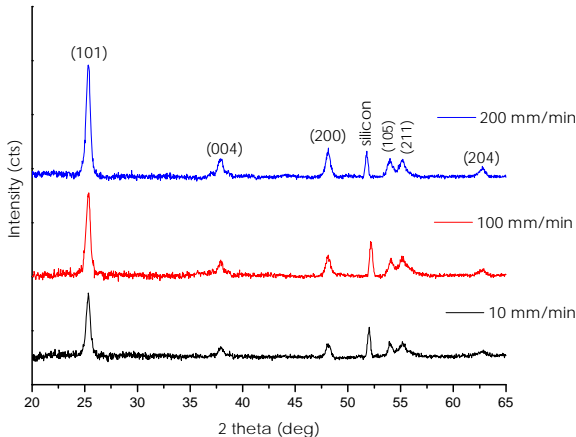


Fig. 3 XRD patterns of TiO₂ thin films with different withdrawal speed.

As the withdrawal speed of dip coating increased, the intensity also increases. The increasing in the intensity of the XRD peak is reported due to increasing in film thickness [10]. This result agrees well with the thickness measurement as shown in Fig. 1. From the XRD patterns presented in Fig. 2, the (101) peaks show the highest intensity. Therefore, the crystallite size was calculated on the (101) plane as shown in Table 1. Scherrer's equation is used to estimated the crystallite size from full width at half maximum (FWHM) of the XRD peak, and is given by,

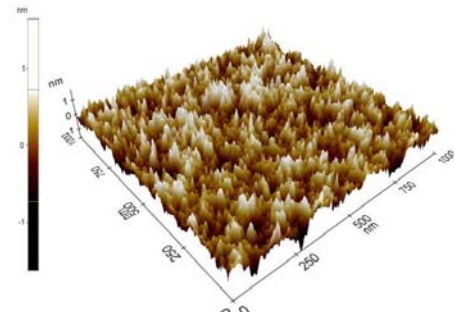
$$D = \frac{K\lambda}{\beta \cos \theta}$$

where D represents the crystallite size, K is a dimensionless number known as scherrer constant (0.9), λ is the wavelength of the incident x-ray beam, θ is the bragg angle and β is the FWHM of the XRD peak in radian. When withdrawal speed increased, the crystallite size of TiO₂ increases from 22 to 39 nm.

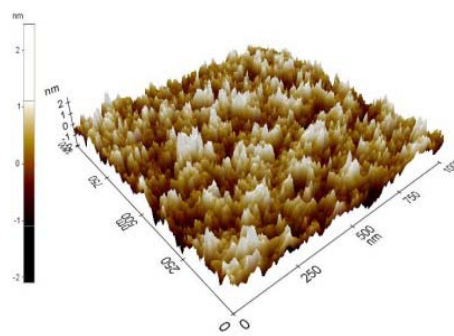
Table 1 The crystallite size of the (101) peak of the TiO₂ thin films with different withdrawal speed.

Withdrawal speed (mm/min)	Intensity (cts)	FWHM (deg)	Crystallite size (nm)
*10	1148.7	0.3542	22.99
100	1439.8	0.2657	30.65

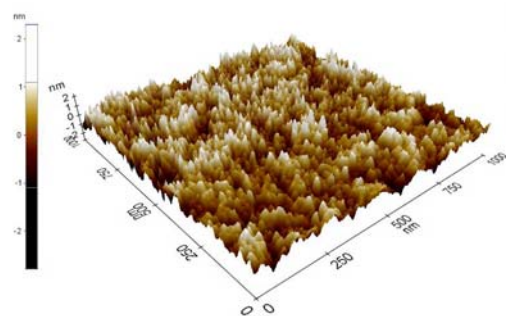
*200	2022.0	0.2066	39.42
*The minimum and maximum speed for this dip coater machine			



(a)



(b)



(c)

Fig. 4 AFM images of TiO₂ thin films with different withdrawal speed (a) 10 (b) 100 (c) 200 mm/min

The AFM images of the TiO₂ thin films fabricated at different withdrawal speeds are presented in Fig. 4. AFM images show homogenous film with different heights for each films. Table 2 presents the grain size and root mean square roughness of the TiO₂ thin films obtained from the AFM measurement. With the increasing of withdrawal speed, the average grain size and the root mean square (RMS) roughness of the TiO₂ thin films increases as shown in Table 2. The grain size increases from 33 to 61 nm while the RMS values of the films were about 0.371, 0.563 and 0.739 nm for withdrawal speeds of 10, 100 and 200 mm/min, respectively. The average grain size and

surface roughness of the films are strongly depending on the withdrawal speed.

Table 2 The AFM data of the TiO₂ thin films with different withdrawal speed.

Withdrawal speed (mm/min)	Average grain size (nm)	Root mean square roughness, (nm)
10	33	0.371
100	42	0.563
200	61	0.739

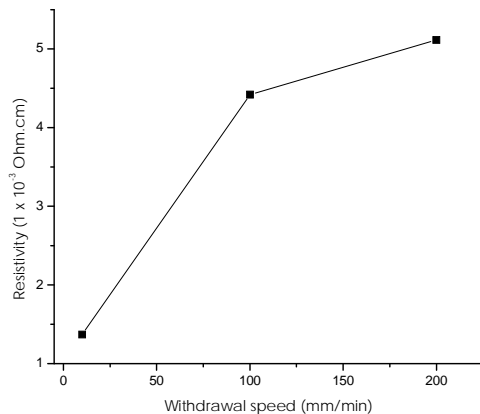


Fig. 5 AFM images of TiO₂ thin films with different withdrawal speed (a) 10 (b) 100 (c) 200 mm/min

Fig. 5 indicates the resistivity of the TiO₂ thin film at various withdrawal speed. It is clearly observed that the resistivity of the film is directly proportional to the withdrawal speed. The increases in the resistivity of the films may be due to the increase of the surface roughness. Rough surface of the films are expected to cause the diffusive of electrons [11].

4. Conclusion

TiO₂ thin films were successfully fabricated using a sol-gel dip coating technique. All films were characterized using XRD, AFM and four-point probe. In the end of this study, we found that when the withdrawal speed increased, the films thickness increases. The film roughness, grain size and resistivity were also increases. It might be strong correlation between film roughness, grain size and resistivity when withdrawal speed increased. Therefore, these findings can be applied for several applications such as solar cells and gas sensor devices where the grain size, roughness and resistivity of the TiO₂ film is critically measure to produce a good performance of device.

Acknowledgment

The facilities used in this study were supported by MiNT-SRC, Universiti Tun Hussein Onn Malaysia (UTHM).

The authors would like to thank Mrs. Faezahana for her technical assistance. This study is financially supported by Ministry of Higher Education Malaysia under MyBrain 15 scholarship and Preston Shipyard under contract grant no. vot A124.

References

- [1] S. Valencia, J. M. Marin, and G. Restrepo, Study of the Bandgap of Synthesized Titanium Dioxide Nanoparticules Using the Sol-Gel Method and a Hydrothermal Treatment, *Open Mater. Sci. J.* Volume 4, (2011), pp. 9–14.
- [2] R. Castelino and N. G. Pramod, Selective CO sensing using nanostructured TiO₂ gas sensors : A review, *Int. J. Smart Sens. Intell. Syst.* Volume 9, (2011), pp. 2237–2256.
- [3] M. M. Byranvand, A N. Kharat, L. Fatholahi, and Z. M. Beiranvand, A Review on Synthesis of Nano-TiO₂ via Different Methods, *J. Nanostructures.* Volume 3, (2013), pp. 1–9.
- [4] A. Di Paola, M. Bellardita, and L. Palmisano, Brookite, the Least Known TiO₂ Photocatalyst, *Catalyst.* Volume 3, (2013), pp. 36–73.
- [5] E. C. Dell'Orto, S. Caldirola, A. Sassella, V. Morandi, and C. Riccardi, Growth and properties of nanostructured titanium dioxide deposited by supersonic plasma jet deposition, *Appl. Surf. Sci.* Volume 425, (2017), pp. 407–415.
- [6] A.-L. Anderson and R. Binions, The Effect of Tween® Surfactants in Sol-Gel Processing for the Production of TiO₂ Thin Films, *Coatings.* Volume 4, (2014), pp. 796–809.
- [7] W. Maziarz, A. Kusior, and A. Trenczek-Zajac, Nanostructured TiO₂ based gas sensors with enhanced sensitivity to reducing gases, *Beilstein J. Nanotechnol.* Volume 7, (2016), pp. 1718–1726.
- [8] D. C. L. Vasconcelos, E. H. M. Nunes, A. C. S. Sabioni, P. M. P. Vasconcelos, and W. L. Vasconcelos, Optical characterization of 316L stainless steel coated with sol-gel titania, *J. Non. Cryst. Solids.* Volume 358, (2012), pp. 3042–3047.
- [9] S. Aydemir, Effects of withdrawal speed on the microstructural and optical properties of sol-gel grown ZnO:Al thin films, *Vacuum.* Volume 120,(2015), pp. 51–58.
- [10] L. Lopez, W. A. Daoud, D. Dutta, B. C. Panther, and T. W. Turney, Effect of substrate on surface morphology and photocatalysis of large-scale TiO₂ films, *Appl. Surf. Sci.* Volume 265, (2013), pp. 162–168.
- [11] V. Timoshhevskii, Y. Ke, H. Guo, and D. Gall, The influence of surface roughness on electrical conductance of thin Cu films: An ab initio study, *J. Appl. Phys.* Volume 103, (2008), pp. 9–12.

A REVIEW ON SEMICONDUCTOR MATERIALS FOR PHOTOCHEMICAL WATER SPLITTING: RECENT ADVANCES AND FUTURE CHALLENGES

Sawsan Abdullah Abduljabbar Anaam^{1,2}, Hashim Saim¹, Mohd Zainizan Sahdan¹, Anis Suhaili Bakri¹, Siti Ashraf Abdullah¹

¹ Microelectronics & Nanotechnology-Shamsuddin Research Centre (MiNT-SRC), Universiti Tun Hussein Onn Malaysia (UTHM), 86400 Batu Pahat, Johor

² National Atomic Energy Commission (NATEC), Sana'a, Yemen

Abstract: Photoelectrochemical (PEC) water splitting is the promising method for hydrogen generation under sunlight irradiation. The chemical reaction occurs on the semiconductor anode and cathode which releases oxygen and hydrogen. The challenge using this method is to produce efficient and stable semiconductor films for the anode and cathode. In this paper, recent developments on the semiconductor used for PEC were reviewed. The advantages and drawbacks of photoanode and photocathode were discussed. In this finding, no semiconductor material meets all requirements for high solar-to- hydrogen efficiency. The low efficiency of semiconductors because of its photocorrosion, wide band gap or its recombination of photogenerated carriers.

Keywords: photoelectrochemical water splitting; hydrogen production; photocurrent; semiconductor; photocathode; photanode; solar-to-hydrogen efficiency

1. Introduction

Energy is essential for continual consumption of the world population and maintaining lifestyle standards. It is needed for transportation, industrial sectors and development of technologies. Currently, fossil fuel is the most energy used for human civilization. However, fossil fuel which includes coal, crude oil, and natural gas is non-renewable energy source. Furthermore, the combustion of fossil fuel leads to emission of greenhouse gases such as carbon dioxide (CO_2). Moreover, rapid growth of urbanization and industrialization results in the consumption of fossil fuel which will be depleted in the future [1-4]. Developing clean and renewable energy is important to avoid the problems caused by fossil fuel.

Solar energy is considered as renewable energy. However, the main drawback of solar energy is its intermittency. The electricity is unavailable at night, in cloudy days, or winter season; as a result, electricity from photovoltaic devices is not available every time and not enough for human needs [5]. Converting sunlight to chemical fuel is the best method to obtain sufficient solar energy. Hydrogen can play a significant role for energy supply of a sustainable economy and zero air pollution [6]. Hydrogen can be produced from solar energy by using three methods; thermochemical water splitting, water electrolysis and photoelectrochemical water splitting. Although, water electrolysis and thermochemical water splitting is a suitable method for renewable hydrogen production, the greatest challenge of using these technologies is reducing hydrogen generation

cost [7]. Due to the limitation of using water electrolysis and thermochemical water splitting for hydrogen production, scientists tried to find another method which

is simple, cheap, and sufficient for hydrogen production using solar energy. Photoelectrochemical (PEC) water splitting is the most promising method for hydrogen generation. Solar water splitting only needs photons from sunlight and material to absorb the sunlight and react with water to generate hydrogen and oxygen [8].

The initial attempt for hydrogen production using sunlight via photoelectrochemical water splitting was reported by Fujishima and Honda. Titanium dioxide (TiO_2) was used as the photoanode and platinum as the cathode. When TiO_2 electrode was exposed to sunlight, oxygen will be generated on the photoanode and hydrogen will be generated of the cathode [9]. After Fujishima and Honda work, scientists use various semiconductor materials for solar hydrogen production through photoelectrochemical (PEC) water splitting.

In this review, we briefly present the principle of photoelectrochemical water splitting and the requirement of semiconductor materials for efficient materials in PEC water splitting. Furthermore, we study the recent research area that has used semiconductors as photoanode and photocathode. The paper focused on the advantages and drawbacks of the most common materials used as electrodes for PEC water splitting.

2. Principle of photoelectrochemical water splitting

When a semiconductor is exposed to photons from sunlight where their energies exceed the semiconductor band gap, photons will excite electrons in the valence band (VB) to the conduction band (CB) leaving holes behind. According to equation (1), the holes, in the valence band which are supplied by anode, oxidize the water to produce oxygen. Electrons move to cathode to produce hydrogen as is shown in equation (2). The overall and basic principle of water reduction and water oxidation reaction is shown in equation (3) and figure 1 respectively.

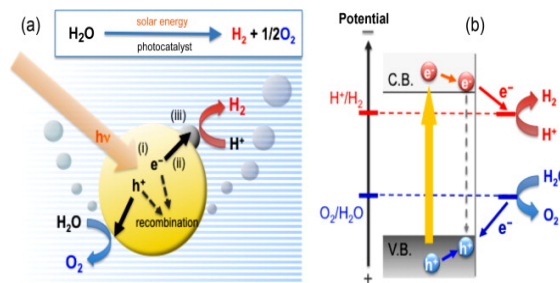
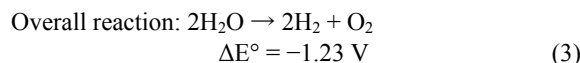
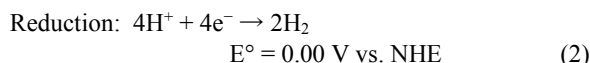
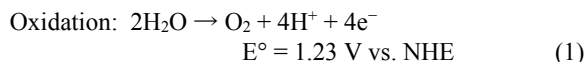


Figure 1 Schematic illustration of photoelectrochemical water splitting principle, (a) holes and electrons of semiconductor are excited by sunlight, (b) water splitting on semiconductor surface [10].

3. Requirement for efficient PEC water splitting

Up to date, researchers have been synthesized various semiconductor materials for hydrogen production by solar water splitting. For economic and practical using of semiconductors for hydrogen production, the solar-to-hydrogen (STH) efficiency must be greater than 15% and current densities should be between 10 - 15 mA.cm⁻² [11, 12].

The main barrier of using semiconductor materials for PEC water splitting is the absorption of visible spectrum of sun and the band edge position for water splitting. Although most studies focused on narrowing band gap for visible light absorption, few studies were paid attention on the band edge position to drive the water oxidation and reduction reaction. The band edge position should be taken into consider because the PEC water spitting occurs in aqueous environment. In other words, for ideal PEC water splitting reaction, the semiconductor should have bandgap large enough (>1.23 eV at standard conditions) for efficient water splitting reaction. Furthermore, the band gap of semiconductor should be

small enough to include most of the visible spectrum [13]. The band structure of some semiconductors with respect to water redox potential is shown in figure 2. Moreover, to obtain high solar-to-hydrogen (STH) efficiency other requirements should be considered. Among these requirements are economically viable, abundant, and stable in aqueous solution, and non-toxic [14].

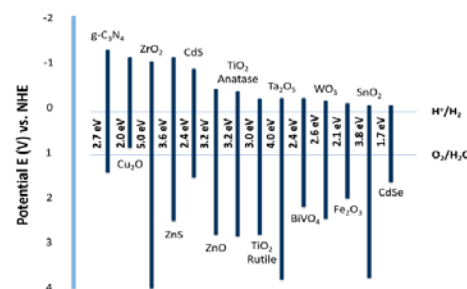


Figure 2 band structures of semiconductors with respect to water redox potentials [15].

4. Semiconductor materials for PEC water splitting

There are various types of semiconductor materials can be used for PEC water splitting. They can be used either as photoanode or photocathode.

4.1 Semiconductor materials as photoanode

Many semiconductors can be utilized as photoanode for direct solar water splitting. The anodic electrode for water oxidation is n-type semiconductor. The photoexcited holes on the surface of semiconductors participate in water oxidation reaction. The electrons move to counter electrode via external circuit and participate in water reduction reaction as is shown in figure 3 [16]. To harvest broad visible sunlight, semiconductor should have narrow band gap. Besides, the valence band edge position of semiconductor should be more positive than water oxidation potential in order to drive the water oxidation reaction [17]. In photoanodic electrode the holes is responsible for oxidation reaction to produce oxygen.

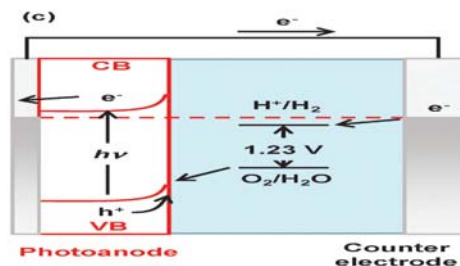


Figure 3 Energy diagrams of PEC water splitting based on photoanode [16].

Among these semiconductors which have been used as photoanodes, Bismuth vanadate (BiVO₄) can be used

as a photoanode for water oxidation. It has a suitable band gap (2.4 eV) to absorb visible sunlight and it is chemically stable in water under sunlight irradiation [18]. However, the main drawbacks of BiVO₄ are its recombination of photogenerated carriers and slow charge transfer between BiVO₄ and electrolyte which obtains low efficiency. Many studies have been carried out to improve the performance of BiVO₄. One of these studies is fabrication of core-shell WO₃ nanorods /BiVO₄ as photoanode. This heterojunction of WO₃ and BiVO₄ was used to reduce the recombination of photogenerated carrier. The measured photocurrent was 6.72 mA cm⁻² under the standard AM1.5G illumination at 1.23 V_{RHE} [19]. Another study was achieved to improve the charge separation of BiV₄. They deposited nanoporous Mo-doped BiVO₄ (Mo:BiVO₄) on cone-shaped nanostructure, nanocone/Mo:BiVO₄/Fe(Ni)OOH photoanode which obtained 5.82 mA cm⁻² under the standard AM1.5G illumination at 1.23 V vs RHE with solar-to-hydrogen conversion efficiency of up to 6.2%[20].

Besides BiVO₄, hematite (α -Fe₂O₃) also has desirable features to be used a photoanode for PEC water splitting. It absorbs visible light because its band gap is 2.1 eV. Moreover, α -Fe₂O₃ is stable in aqueous solution, abundant and cheap [21]. However, the using of α -Fe₂O₃ for PEC water splitting is limited due to the high electron–hole pair recombination rate. A method to prevent the charge recombination and increase the charge transfer of α -Fe₂O₃ is fabrication of a Fe₂O₃/graphene composite. The photocurrent obtained was 1.63 mA cm⁻² at 1.8 V vs reversible hydrogen electrode (RHE) [22].

Zinc oxide (ZnO) is an attractive metal oxide semiconductor for PEC water splitting because of its stability, low cost, high electron mobility and nontoxicity [23]. Although ZnO meets the most desirable requirement for PEC water splitting, its main disadvantages are the photocorrosion in aqueous solution and its large band gap 3.26 eV [24]. Vuong et al. fabricated hydrogenated ZnO (H:ZnO) to improve the performance of ZnO for PEC water splitting, they observed that H:ZnO nanorods enhanced the photocurrent in comparison with ZnO nanrods [25].

4.2 Semiconductor materials as photocathode

Photocathode semiconductors also have been used to improve the PEC water splitting. The photocathode is used for water reduction and should be a p-type semiconductor which acts as a photocathode for water reduction to produce hydrogen. The conduction band edge position should be more negative than water reduction potential as shown in figure 4 [16]. The band gap of semiconductor should be narrow enough to absorb a large portion of visible sunlight to drive the water reduction reaction to produce hydrogen. In photocathodic electrode, electrons participate in proton reduction to generate hydrogen.

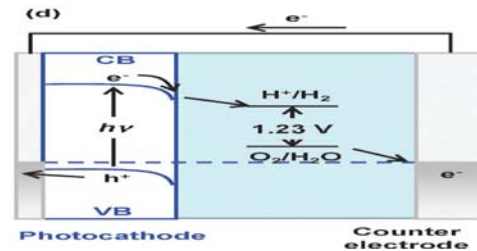


Figure 4 Energy diagrams of PEC water splitting based on photocathode, ref [16].

In comparison with photoanode semiconductors, there are few research papers studying semiconductors as photocathode for PEC water splitting. Cuprous oxide (Cu₂O) has extensive attention towards PEC water splitting because of its absorption in visible region which is related to its suitable band gap (2.0 eV). Furthermore, band edge position is more negative than water reduction potential and used as photocathode [26]. Despite the suitable features of Cu₂O for PEC water splitting, it suffers from photocorrosion in aqueous solution. Qi et al. used modified Cu₂O/NiFe- Layered Double Hydroxide (LDH) electrode for water reduction. The photocurrent increased due to using NiFe-LDH which improved the electrons transfer and enhanced the stability of Cu₂O. The photocurrent was increased from 1.27 mA cm⁻² to 2.42 mA cm⁻² by using NiFe-LDH [27].

Besides Cu₂O semiconductors, cadmium Sulfide (CdS) can be used as photocathode. CdS has band gap 2.4 eV. Moreover, CdS has suitable valence and conduction band edge position for oxidation and reduction of water respectively. However, using CdS as photoanodes suffer from photocorrosion because it is oxidized by photogenerated holes. Although CdS can't be used as photoanode, it can be used as photocathode. Huang et al. doped copper on CdS to fabricate CdS:Cu photocathode. The photocurrent and stability was enhanced by modifying CdS: Cu surface with Pt nanoparticles [28].

5. Summary and future perspective

In this paper, we have reviewed the recent advance of using semiconductors materials for PEC water splitting. Although various studies has been done to fabricate efficient materials for PEC water splitting, there are various challenges should be addressed. For example, some of semiconductors suffer from instability and photocorrosion in aqueous solution such as Cu₂O and ZnO. Others have high electron–hole pair recombination rate like α -Fe₂O₃. Some of them do not absorb visible light; hence, they do not harvest the great spectrum of sun. For future work, to improve the performance of semiconductor for PEC water splitting to produce hydrogen, it still needs to overcome the barriers of which obtained low solar-to-hydrogen efficiency. Although most of studies have been focused on doping and using single photoelectrode to improve the efficiency for PEC water splitting, the photocurrent and efficiency are still very low. It is needed to focus on intrinsic defects in

semiconductors to prevent electron-hole pair recombination which occurs by using external defect. Moreover, we should expend research on fabrication one device which should have two photoelectrodes (photoanode/photocathode) in order to harvest more sunlight for water splitting reaction. Besides the intrinsic defect and photoanode/photocathode method, the p-n homojunction method should be considered to prevent the recombination photo-induced charge carriers.

Acknowledgment

The authors are grateful to the Universiti Tun Hussein Onn Malaysia with Grant contract VOT A124.

References

- [1] Peharz, G., Dimroth, F., and Wittstadt, U. Solar hydrogen production by water splitting with a conversion efficiency of 18%. *International Journal of Hydrogen Energy*, volume 32, (2007), pp. 3248–3252.
- [2] Liao, C.H., Huang, C.W., and Wu, J.C.S. Hydrogen Production from Semiconductor-based Photocatalysis via Water Splitting. *Catalysts*, Volume 2, (2012), pp. 490–516.
- [3] Kochuveedu, S.T. (2016) Photocatalytic and Photoelectrochemical Water Splitting on TiO₂ via Photosensitization. *Journal of Nanomaterials*, Volume 2016, (2016), pp. 1–12.
- [4] Guan, W.F.S., (2007) Hydrogen evolution from water splitting on nanocomposite photocatalysts. *Science and Technology of Advanced Materials*, volume 8, pp. 76–81.
- [5] Sharma, A. A comprehensive study of solar power in India and World. *Renewable and Sustainable Energy Reviews*, volume 15, (2001), pp. 1767–1776.
- [6] Mao, S. M., Shen, S. H., and Guo, L.J. (2012). Nanomaterials for renewable hydrogen production, storage and utilization. *Materials International*, 22(6): 522–534.
- [7] Landman, A., Dotan, H., Shter, G.E., Wullenkord, M., Houaijia, A., Maljusch, A., Grader, G.S., and Rothschild, A. Photoelectrochemical water splitting in separate oxygen and hydrogen cells. *Nature Materials*, volume 16, (2017), pp. 646–651.
- [8] Miller, E.L. Photoelectrochemical water splitting. *Energy Environ. Sci.*, volume 8, (2015), pp. 2809–2810.
- [9] Fujishima A., and Honda K. Electrochemical photolysis of water at a semiconductor electrode. (1972). *Nature*, Volume 238, (1972), pp. 37–38.
- [10] Abe, R. Recent progress on photocatalytic and photoelectrochemical water splitting under visible light irradiation. *Journal of Photochemistry and Photobiology C: Photochemistry Reviews*, volume 11, (2010), pp. 179–209.
- [11] May, M.M., Lewerenz, H.J., Lackner, D., Dimroth, F., and Hannappel, T. Efficient direct solar-to-hydrogen conversion by in situ interface transformation of a tandem structure. *Nat Commun* 6, (2015).
- [12] Juodkazyt, J., Seniutinas, G., Sebeka, B., Savickaja, I., Malinauskas, T., Badokas, K., Juodkazis, K., and Juodkazis,S. Solar water splitting: Efficiency discussion, *International Journal of Hydrogen Energy*, volume 41(2016), pp.1-8.
- [13] Zhou, C., O'Brien, J.E., Rajan, G., Marsillac, S., and Xiaoyu Zhang, X.Y. Water Splitting Using High Temperature Solid Oxide Photoelectrochemical Cell and Visible Sunlight: Searching for the Appropriate Semiconductor Materials, *Journal of The Electrochemical Society*, Volume 164, (2017), pp. H497-H502.
- [14] Momeni, M.M., & Nazari, Z. Fabrication of new photoanodes for solar-water-splitting photoelectrochemical cells: synergistic effect between platinum and nanocomposite photocatalysts. *Journal of Materials Research Innovations*, volume 20, (2016), pp.51-57.
- [15] Jafari, T., Moharreri,E., Amin, A.S., Miao, R., Song, W.Q., and Suib, S.L. Photocatalytic Water Splitting—The Untamed Dream: A Review of Recent Advances. *Molecules*, volume 21, (2016), pp. 1–29.
- [16] Hisatomi, T., Kubota, J., and Domen, K. Recent advances in semiconductors for photocatalytic and photoelectrochemical water splitting. *Chem. Soc. Rev.*, 2014, volume 43, (2014), pp. 7520–7535
- [17] Chen, S.Y., and Wang, L.W. Thermodynamic Oxidation and Reduction Potentials of Photocatalytic Semiconductors in Aqueous Solution. *Chem. Mater.*, volume 24, 2012 pp. 3659–3666.
- [18] Joa, W.J., Kang, H.J., Kong, K.J., Lee, Y.S., Parkb, H., Lee, Y., Buonassisi, T., Gleason, K.K., & Lee, J.S. Phase transition-induced band edge engineering of BiVO₄ to split pure water under visible light, *Proc Natl Acad Sci U S A*. volume 112, (2015), pp.13774–13778.
- [19] Pihosh,Y., Turkevych, I., Mawatari, K., Uemura, J., Kazoe, Y., Kosar, S., Makita, K., Sugaya, T., Tosa, M., Kondo, M., and Kitamori,T. Photocatalytic generation of hydrogen by core-shell WO₃/BiVO₄ nanorods with ultimate water splitting efficiency. *Scientific Reports* 5, Article number: 11141, (2015), pp. 1–10.
- [20] Qiu, Y.C., Liu, W., Chen, W., Chen, W., Zhou, G.M., Hsu, P., Zhang, R.F., Liang, Z., Fan, S.S. Zhang, Y.G., and Cui, Y. Efficient solar-driven water splitting by nanocone BiVO₄-perovskite tandem cells. *Science Advances*, volume 2, (2016), pp. 1–8.
- [21] Kenneth J. McDonald, K.J., & Choi, K.S. Synthesis and Photoelectrochemical Properties of Fe₂O₃/ZnFe₂O₄ Composite Photoanodes for Use in Solar Water Oxidation, *Chem. Mater.*, Volume 23, (2011), pp. 4863–4869.
- [22] Liu,S.X., Zheng , L.X., Yu, P.P , Han, S.C . , and Fang, X.S. Novel Composites of α -Fe₂O₃

- Tetrakaidecahedron and Graphene Oxide as an Effective Photoelectrode with Enhanced Photocurrent Performances. *Adv. Funct. Mater.*, Volume 26, (2016), pp. 3331–3339.
- [23] Shen, S.H., Chen, J.N., Ren, L.C.F., Liejin Guo. Strategy of engineering impurity distribution in metal oxide nanostructures for photoelectrochemical water splitting. *Journal of Materomics*, Volume 1, (2015), pp. 134-145.
- [24] Simelys Hernandez, S., Hidalgo, D., Sacco, A., Chiodoni, A., Lamberti, A., Cauda, V., Tressoab, E., & Saracob, G. Comparison of photocatalytic and transport properties of TiO₂ and ZnO nanostructures for solar-driven water splitting. *Phys Chem Chem Phys.*, Volume 17, (2015) pp.7775-7786.
- [25] Vuong, N.M., Reynolds, J.L., Conte, E., & Lee, Y. H:ZnO Nanorod-Based Photoanode Sensitized by CdS and Carbon Quantum Dots for photoelectrochemical Water Splitting. *J. Phys. Chem. C*, Volume 119, (2015), pp. 24323–24331.
- [26] Luo, J., Steier,L., Son, M., Schreier,M., Mayer, M.T. Grätzel,M. Cu₂O Nanowire Photocathodes for Efficient and Durable Solar Water Splitting. *Nano Lett.*, Volume 16,(2016), pp. 1848–1857.
- [27] Qi1, H., Wolfe,J., Fichou,D., and Zhong Chen, Z. Cu₂O Photocathode for Low Bias Photoelectrochemical Water Splitting Enabled by NiFe-Layered Double Hydroxide Co-Catalyst. *Nano Lett.*, Volume1, (2016) pp. 1848–1857.
- [28] Huang, Q., Li, Q. and Xiao, X. Hydrogen Evolution from Pt Nanoparticles Covered p-Type CdS:Cu Photocathode in Scavenger-Free Electrolyte. *J. Phys. Chem. C.*, Volume118, (2014).pp. 2306–2311.